Fast Prediction of Radio Channel Large-Scale Parameters Considering Environmental Factors

Lingyou Zhou

School of Electrical and Electronic Engineering

The University of Sheffield

Supervisors: Prof Jie Zhang & Prof Timothy O'Farrell

This thesis is submitted for the degree of

Doctor of Philosophy

April 2026

This thesis is dedicated to my beloved parents and family. It is their deepest love and greatest support that have led me here and where I am going.

Acknowledgements

First and foremost, I would like to express my sincere appreciation to my supervisor, Prof Jie Zhang, for giving me the opportunity to pursue a PhD and for his guidance and support throughout my research. At the beginning of my PhD in early 2022, he shared with me five key qualities of being a good person and a good researcher: integrity, tenacity, critical thinking, passion, and curiosity. These values have guided me throughout my entire PhD journey. Their presence was essential in helping me navigate the many difficult times—especially in 2023 and early 2024—and I am truly grateful for these "shore beacons" that kept me grounded. He also shared with me what it takes to become a good researcher: having a broad perspective and a solid understanding of the wider field, becoming a specialist in my own research area, and developing strong skills in mathematics, coding, and academic writing. Although I am still far from reaching these goals, I believe that with consistent effort each day, I can gradually move closer to them.

Meanwhile, I wish to acknowledge my deep gratitude to Prof Jiliang Zhang (Northeastern University, China) for his hands-on guidance at the beginning of my PhD study, which helped me learn how to conduct research step by step. The research outcomes I have achieved are deeply rooted in the guidance and inspiration he provided at the start of my research journey. His noble character and rigorous academic attitude continue to serve as a role model for me. Further, I would like to convey my profound appreciation to Prof Timothy O'Farrell and Dr Tiantai Deng for their kind support during my thesis writing-up period. Following that, I would also like to thank the examiners of my PhD viva, Prof Xiaoli Chu and Prof Ian Wassell (University of Cambridge), for their time and their valuable feedback, which has been very helpful in improving my thesis.

Besides, I would like to thank Dr Haonan Hu, Dr Sai Xu, Dr Zitian Zhang, Dr Zeyang Li, Dr Yan Jiang, and Ms Keira Sweet for their help and advice during my PhD study. During my time at Ranplan Wireless, I would like to thank Dr Jiming Chen for his guidance on the engineering work and Dr Kan Lin for his help. I am also grateful to Prof Bowei Yang (Zhejiang University, China) for his kind help during my visit to Zhejiang University in 2023, Prof Di Yuan (Uppsala University, Sweden) for his kind help during my secondment to Uppsala University in 2024 and 2025, and to the anonymous reviewers of my paper published in IEEE AWPL in 2024 for their valuable comments.

Beyond research, I would like to thank Mr Hang Yuan for his advice and care in 2023 and for his guidance during my undergraduate study, as well as Ms Yangfan Zhang for her advice and teaching during my undergraduate study. I am also thankful to Mr Gang Yu, Mr Qiquan Wang, and Mr Mingwu Xue for their care in 2023.

Last but not least, I would like to thank my parents, Xi Wan and Hong Zhou, and my family, Wanlan Zhou, Qinglin Wan, Yi Wan, and Jian Wan, for their constant support and encouragement over the years.

大学之道，在明明德，在亲民，在止于至善。知止而后有定，定而后能静，静而后能安，安而后能虑，虑而后能得。物有本末，事有终始。知所先后，则近道矣。

古之欲明明德于天下者，先治其国。欲治其国者，先齐其家。欲齐其家者，先修其身。欲修其身者，先正其心。欲正其心者，先诚其意。欲诚其意者，先致其知。致知在格物。

——《礼记·大学》

Abstract

Radio channel modelling is a crucial technique for the development of sixth generation (6G) and beyond 6G (B6G) networks. With the increase in environmental complexity and technical diversity, channel modelling techniques are eventually required to cover environmental information as a digital twin channel (DTC) for complete simulation information, acceptable prediction accuracy, and low modelling complexity. However, current mainstream channel models, the geometry-based stochastic channel models (GSCMs), are rooted in statistical distributions without physical surrounding information, and so they cannot be further evolved into an alternative option for future channel models.

Under these circumstances, in this thesis, we propose a potential method for enhancing current GSCMs with environmental considerations for the future development of channel modelling. We develop the adaptive multiple path loss exponent (AMPLE) framework and its large-scale parameter (LSP) extension (AMPLE-LSP), incorporating environmental information directly into statistical modelling. This framework bridges the gap between deterministic ray-based models and conventional statistical models, achieving significantly improved prediction accuracy while preserving LSP simulation efficiency. Extensively validated via measurements and ray-based simulations, these models consistently outperform widely used models such as those defined by the Third Generation Partnership Project (3GPP) and the Fifth Generation Channel Model Special Interest Group (5GCMSIG), at a comparable computational cost. These results provide a practical and scalable solution for realistic vehicular and wireless network studies, opening a new direction for future GSCMs.

List of Publications

[1] **L. Zhou**, X. Dong, K. Qiu, G. Yu, J. Zhang, and J. Zhang, "Ray-based characterization of the AMPLE model from 0.85 to 5 GHz," *IEEE Trans. Antennas Propag.*, vol. 73, no. 10, pp. 8174-8188, Oct. 2025.

[2] **L. Zhou**, J. Zhang, J. Zhang, K. Lin, W. Qi, and J. Chen, "A site-specific channel large-scale parameter model with ray-based validation," *IEEE Trans. Veh. Technol.*, early access, doi: 10.1109/TVT.2025.3640770.

[3] **L. Zhou**, J. Zhang, J. Zhang, O. Cetinkaya, and S. A. Jubb, "AMPLE: An adaptive multiple path loss exponent radio propagation model considering environmental factors," *IEEE Trans. Veh. Technol.*, vol. 74, no. 2, pp. 3395-3400, Feb. 2025.

[4] **L. Zhou**, J. Zhang, J. Zhang, and K. Qiu, "An environment-adaptive radio propagation path loss model with ray-based validation," *IEEE Antennas Wireless Propag. Lett.*, vol. 23, no. 10, pp. 3217-3221, Oct. 2024.

[5] X. Dong, C. Chen, G. Yu, **L. Zhou**, C. Yuan, and J. Zhang, "Deep learning-based channel estimation for stacked intelligent metasurface-enhanced multi-user communications," *IEEE Trans. Veh. Technol.*, early access, doi: 10.1109/TVT.2026.3653980.

[6] G. Yu, **L. Zhou**, J. Zhang, and J. Zhang, "A ray-launching algorithm for polarized wireless channel prediction," in *Proc. 2023 IEEE Globecom Workshops (GC Wkshps)*, 2023, pp. 1928-1933.

[7] L. Xiao, J. Liu, **L. Zhou**, Q. Hu, Z. Hua, R. Zhang, W. Gu, and J. Zhang, "Characterization of the AMPLE channel model for IEEE 802.11ah-Based IoT," in *Proc. 2025 IEEE 25th Int. Conf. Commun. Technol. (ICCT)*, 2025, pp. 139-143.

[8] G. Yu, Y. Zhang, X. Dong, W. Xi, **L. Zhou**, Y. Zheng, J. Zhang, and J. Zhang, "Eliminating the bit error floor of polarization modulation by using wireless friendly building materials," major revision, under review in *IEEE Trans. Commun*.

Table of contents

List of figures

List of tables

Abbreviations

2D Two-Dimensional

3D Three-Dimensional

3GPP Third Generation Partnership Project

4G Fourth Generation

5G Fifth Generation

5GCMSIG Fifth Generation Channel Model Special Interest Group

5GNR Fifth Generation New Radio

6G Sixth Generation

ABG Alpha-Beta-Gamma Model

AHRE Average Total Hit Ratio Error

AI Artificial Intelligence

AIC Akaike Information Criterion

AMPLE Adaptive Multiple Path Loss Exponent Radio Propagation Model

AMPLE-LSP AMPLE Model for Large-Scale Parameter

AOA Azimuth Angle of Arrival

AS Angular Spread

ASA Azimuth Angular Spread of Arrival

AT&T American Telephone and Telegraph Company

B6G Beyond Sixth Generation

CDF Cumulative Distribution Function

CEPT European Conference of Postal and Telecommunications Administrations

CI Close-In

CIF Close-In Model With A Frequency-Weighted Path Loss Exponent

CIR Channel Impulse Response

COST European Cooperation in Science and Technology

CPU Central Processing Unit

DS Delay Spread

DTC Digital Twin Channel

D2D Device-To-Device

ECC Electronic Communication Committee

FDTD Finite-Difference Time-Domain

FEM Finite Element Method

FIT Finite Integration Technique

GBSM Geometry-Based Stochastic Model

GIS Geographic Information System

GPS Global Positionging System

GSCM Geometry-Based Stochastic Channel Model

GTD Geometrical Theory of Diffraction

IEEE Institute of Electrical and Electronics Engineers

IMT-2020 International Mobile Telecommunications-2020

InH Indoor Hotspot

InF Indoor Factory

ITU-R International Telecommunication Union-Radiocommunication Sector

LoRaWAN Long Range Wide Area Network

LOS Line-Of-Sight

LS Least Squares

LSP Large-Scale Parameter

LSPE Large-Scale Parameter Exponent

MAE Mean Absolute Error

METIS Mobile and Wireless Communications Enablers for Twenty-twenty (2020) Information Society

MIMO Multiple Input Multiple Output

MiWEBA Millimetre-Wave Evolution for Backhaul and Access

ML Maximum Likelihood

mmMAGIC Millimetre-Wave Based Mobile Radio Access Network for Fifth Generation Integrated Communications

MoM Method of Moments

NLOS Non-Line-Of-Sight

NYUSIM New York University Channel Model Simulator

PDF Probability Density Function

PLE Path Loss Exponent

PMDE Prediction-Measurement Distribution Error

Q-D Quasi-Deterministic

QuaDRiGa Quasi Deterministic Radio Channel Generator

RAM Random-Access Memory

RGB Red, Green, and Blue

RIS Reconfigurable Intelligent Surface

RMS Root Mean Square

RMSE Root Mean Square Error

RMa Rural Macrocell

RSSI Received Signal Strength Indicator

Rx Receiver

SBR Shooting and Bouncing Rray

SCM Spatial Channel Model

SUI Stanford University Interim Model

SSP Small-Scale Parameter

THR Total Hit Rate

TIA Telecommunications Industry Association

T-R Transmitter-Receiver

TSP Time-Spatial Propagation

Tx Transmitter

UE User Equipment

UMa Urban Macrocell

UMi Urban Microcell

UTD Uniform Theory of Diffraction

V2V Vehicle-To-Vehicle

V2X Vehicle-To-Everything

VR Visibility Region

WiFEEB Wireless Friendly and Energy Efficient Buildings

WINNER Wireless World Initiative New Radio

XML Extensible Markup Language

ZOA Zenith Angle of Arrival

ZOD Zenith Angle of Departure

ZSA Zenith Angular Spread of Arrival

ZSD Zenith Angular Spread of Departure

Chapter 1

Introduction

1.1 Background and Motivation

Channel modelling in the 6G and B6G systems must address significantly more complex propagation scenarios across a wider range of frequencies [1–3]. As a key component of the modelling process, the prediction of LSPs–including path loss, shadow fading, the Ricean K-factor, root mean square (RMS) delay spread (DS), and angular spread (AS)–plays a crucial role in the statistical channel models. These parameters characterise various aspects of the wireless channel, such as channel gain, temporal dispersion, and spatial information, under diverse propagation scenarios. Moreover, in statistical channel models, LSPs serve as essential constraints in the overall channel modelling process, influencing the prediction of small-scale parameters (SSPs) and the construction of the channel matrix [4–14]. In other words, to further enhance the statistical channel models based on current efforts, neglecting LSPs and focusing solely on refining the characterisation of SSPs yields limited improvement and requires considerable effort [15–20].

For the characterisation of LSPs and wireless channels, one of the key modelling approaches is the deterministic channel model. These models are either based on the full-wave solutions, such as the finite-difference time domain (FDTD) [21–23], the finite element method (FEM) [24, 25], the method of moments (MOM) [26, 27], and the finite integration technique (FIT) [28]; or the ray-based methods, such as the ray-tracing and ray-launching

methods [29–31]. Since full-wave solutions are significantly more complex and are primarily used for modelling electromagnetic problems [32–35], deterministic models for LSP prediction typically refer to ray-based models. Based on ray-optics [29–31], these ray-based models predict LSPs by incorporating detailed environmental information and simulating the full propagation process. By applying Maxwell's equations with appropriate boundary conditions [36], they simulate the entire propagation channel, with LSPs obtained as part of the modelling outcome. Further, channel models like the Institute of Electrical and Electronics Engineers (IEEE) 802.11ay channel model [37, 38] and the Millimetre-Wave Evolution for Backhaul and Access (MiWEBA) channel model [39] combine ray-based approach with statistical parameters to predict LSPs and channels. However, to maintain high accuracy, deterministic models require complete environmental information and involve large computational complexity. In more complex environments envisioned for 6G and B6G systems [1–3], ray-based models require more detailed and precise environment information, and the intricate nature of such environments also results in higher computational costs, making it challenging to deploy such models in practical scenarios [40].

In contrast, for simplicity, LSPs can also be modelled under specific propagation scenarios using measurements, and then regressed simply into statistical LSP models based on log-distance. These models cover parameters such as path loss [41, 42], the Ricean K-factor [43, 44], DS [45] and AS [46]. Despite its simplicity, this model type lacks generality and cannot be applied across diverse scenarios and frequency bands, let alone to the more complex and various environments in 6G & B6G. To generally model LSPs under different scenarios with low computational complexity, GSCMs predict LSPs through statistics and distributions. These GSCMs include the Wireless World Initiative New Radio Phase II (WINNER II) channel model [4], the 3GPP channel model [5, 6], the Quasi Deterministic Radio Channel Generator (QuaDRiGa) [7, 8], the 5GCMSIG channel model [9], the Millimetre-Wave Based Mobile Radio Access Network for Fifth Generation Integrated Communications (mmMAGIC) channel model [10], the Mobile and Wireless Communications Enablers for Twenty-twenty (2020) Information Society (METIS) channel model [11], the International Mobile Telecommunications-2020 (IMT-2020) channel model [12], the European Coop-

eration in Science and Technology (COST) 2100 channel model [13], and the New York University Channel Model Simulator (NYUSIM) [14]. For path loss, those models include the alpha-beta-gamma (ABG) model, the close-in (CI) free space reference distance model, and the CI model with a frequency-dependent path loss exponent (PLE) (CIF) [9, 47]. For other LSPs (Ricean K-factor, DS, and AS), based on measurements and reliable ray tracing simulations under different propagation scenarios, these LSPs are characterised via normal distribution in decibels, with different means and standard deviations. However, these LSP prediction methods are limited to scenarios with simple environments. Without redesigning the model structures, these models are limited by their lack of environmental considerations, which gradually leads to large prediction errors as environmental complexity increases.

1.2 Contribution

This thesis proposes a new method for empirically predicting path loss and other channel LSPs while considering environmental factors. Specifically, the aims of this research include: 1) developing a framework for empirical path loss modelling considering environmental factors; 2) refining the proposed path loss model for general and practical usage; and 3) expanding the proposed path loss model to other LSPs to achieve unified LSP prediction with a single consistent formulation. In this section, we first present the contribution of each chapter, followed by an outline of the publications derived from the research.

1.2.1 Contribution of the Thesis

In this section, we give a quick view of the contribution within this thesis. Detailed presentations can be found in the corresponding chapters. Overall, the main contribution of this thesis is summarised as follows:

Chapter 3

- We propose AMPLE–a novel multiple PLE radio propagation model that can adapt to different environmental factors. To the best of our knowledge, this is the first time

that a practical multi-slope model precisely maps PLEs and region types. Besides, this model can be integrated into map systems by creating a new path loss attribute for digital maps.

- We validate the AMPLE model from both measurements and ray-based simulations. Then, we give the process of extracting the AMPLE model based on the datasets we collect. We also compare the AMPLE model with the current path loss models in the 3GPP channel model and the 5GCMSIG channel model.

Chapter 4

- Based on our previous works in Chapter 3 [15–17], we enhance the AMPLE model by introducing an additional frequency coefficient to support path loss prediction across different carrier frequencies.

- We use Ranplan Professional, a measurement-validated ray-based simulator, to simulate and collect path loss data for the fifth generation new radio (5GNR) 0.85 GHz, 2.1 GHz, and 5 GHz under the urban macrocell (UMa) and urban microcell (UMi) scenarios. Four cities are selected as propagation environments to set up the simulations, and the basic information including environments and propagation is based on the definitions of the typical UMa and UMi scenarios [5, 9, 47].

- We conduct a simple validation for the ray-based simulations, specifically under the field of path loss model characterisation. That is, we extract the CI model parameters from the simulations including UMa line-of-sight (LOS), UMa non-line-of-sight (NLOS), and UMi NLOS environments. Then, we compare the simulation-based parameters with those extracted from measurements reported by the research group of Theodore S. Rappaport in [47]. The comparison results show close alignment between the simulation-based and measurement-based CI model parameters.

- We characterise and validate the AMPLE model using Ranplan simulation data across the 0.85–5 GHz range for the UMa LOS, UMa NLOS, UMi LOS, and UMi NLOS

environments. The whole characterisation and validation process is given, which can be considered as the standard characterisation process of the AMPLE model for future research.

- We compare the AMPLE model with the current path loss models in the 3GPP channel model [5] and the 5GCMSIG channel model [9] under the UMa/UMi scenarios with LOS/NLOS environments. Beyond general metrics such as the root mean square error (RMSE) and the mean absolute error (MAE), we propose the prediction-measurement distribution error (PMDE) to show overall alignment between predictions and measurements, and the mean simulation time per point to show model complexity. The overall results show that the AMPLE model outperforms the current empirical models by considering environments while maintaining similar model complexity.

- Based on the results of the AMPLE model in this chapter, we found that the map-based path loss and radio channel models should also account for scenario types (i.e., by modelling under scenario types such as UMa, UMi, and rural macrocell (RMa), rather than treating them identically). This conclusion is expected to significantly influence the future development of both map-based and artificial intelligence (AI)-based models.

Chapter 5

- We review the theoretical basis of the proposed model for different LSPs, that is, the distance-based log-normal modelling methods especially for the Ricean K-factor, DS, and AS [43–46]. To the best of our knowledge, although these methods were introduced in previous studies, they remain largely unfamiliar to researchers in this field. Even without the work of this chapter, the distance-based LSP model structure can be considered a future direction for current GSCMs.

- An LSP prediction framework considering environmental factors is proposed based on the AMPLE radio propagation model that we proposed in the previous works [15–18], and is referred to as the AMPLE-LSP model [19]. This model prototype provides a potential path for the future development of GSCMs in radio communications.

- We use Ranplan Professional [108], a commercial ray-tracing simulator, to generate channel multipath simulations in both outdoor UMa and indoor hotspot (InH) scenarios and validate the proposed AMPLE-LSP model.

- We comprehensively compare the proposed AMPLE-LSP model with the current 3GPP and 5GCMSIG models in both outdoor and indoor scenarios. The results show that the AMPLE-LSP model outperforms these two models while maintaining similar model complexity.

1.2.2 Papers Included in the Thesis

- **Paper I: AMPLE: An Adaptive Multiple Path Loss Exponent Radio Propagation Model Considering Environmental Factors.** Lingyou Zhou, Jie Zhang, Jiliang Zhang, Oktay Cetinkaya, and Stephen A. Jubb. This paper has been published in *IEEE Transcations on Vehicular Technology*, Volume: 74, Issue: 2, Pages: 3395-3400, February 2025.

- **Paper II: An Environment-Adaptive Radio Propagation Path Loss Model With Ray-Based Validation.** Lingyou Zhou, Jie Zhang, Jiliang Zhang, and Kehai Qiu. This paper has been published in *IEEE Antennas and Wireless Propagation Letters*, Volume: 23, Issue: 10, Pages: 3217-3221, October 2024.

- **Paper III: Ray-Based Characterization of the AMPLE Model From 0.85 to 5 GHz.** Lingyou Zhou, Xin Dong, Kehai Qiu, Gang Yu, Jie Zhang, and Jiliang Zhang. This paper has been published in *IEEE Transactions on Antennas and Propagation*, Volume: 73, Issue: 10, Pages: 8174-8188, October 2025.

- **Paper IV: A Site-Specific Channel Large-Scale Parameter Model with Ray-Based Validation.** Lingyou Zhou, Jie Zhang, Jiliang Zhang, Kan Lin, Weijie Qi, and Jiming Chen. This paper has been published in *IEEE Transcations on Vehicular Technology* with early access, December 2025, DOI: 10.1109/TVT.2025.3640770.

It should be noted that, Chapter 3 contains the works of **Paper I** and **Paper II**, of which we combine two papers together with revisions, Chapter 4 contains the revised work of **Paper III**, and Chapter 5 contains the revised work of **Paper IV**.

1.3 Organisation

The remainder of this thesis is organised as follows. Chapter 2 provides a brief review of existing channel modelling approaches, including deterministic and stochastic models, followed by an overview of LSP modelling based on statistical methods. Chapter 3 introduces the proposed AMPLE radio propagation model considering environmental factors, along with the model validations by both measurements and ray-based simulations. Chapter 4 further enhances the AMPLE model with a frequency coefficient to handle the path loss predictions under multiple carrier frequencies, along with the ray-based model characterisation from 0.85 to 5 GHz in the UMa and UMi scenarios. Chapter 5 expands the modelling to other LSPs and present the AMPLE-LSP model with ray-based validations, of which the AMPLE-LSP model covers LSPs including path loss, the Ricean K-factor, DS, and AS. Finally, Chapter 6 draws the conclusion and presents future work of the research.

Chapter 2

Literature Review

In this chapter, we first briefly review the current channel models for radio communications, including deterministic channel models such as ray-based models [29, 30, 48] and full wave solutions [34], and the statistical channel models based on probabilities and distributions [3, 10, 49, 50]. Then, since the main focus of this thesis is on LSPs within the statistical channel models, we also introduce the current methods on modelling path loss [41, 47, 51], and other LSPs including the Ricean K-factor, DS, and AS [10, 43–46].

2.1 Deterministic Channel Models

In this section, we review the deterministic channel models based on electromagnetic theory and Maxwell's equations [36]. The current deterministic models can be classified as the ray-based models (in Section 2.1.1) and the full wave solutions (in Section 2.1.2).

2.1.1 Ray-Based Methods

To accelerate the modelling speed, ray-based models are proposed which simplify the electromagnetic waves to rays [29]. Within the ray-based models, the complete information of propagation environment is required to build up the modelling process. A typical process of ray-based models, in essence, involves asymptotically tracing the propagation of rays from the source to the field point. During propagation, rays may interact with surrounding

environments, leading to different types of rays that are classified according to various electromagnetic mechanisms and modelled using distinct methods. The modelling of the complete multipath propagation via rays aims to generate the channel impulse response (CIR) and channel matrix, in order to capture key channel characteristics, including channel gain, temporal, and spatial information [48].

Since the main topic of this thesis is not about ray-based models, we here only cover the basic information, including types of rays and basic ray-tracing algorithms. Detailed introduction and review of ray-based methods can be found in [29], [30], and [48].

Types of Rays

The basic ray types within a ray-based model can be classified as direct rays, transmitted rays, reflected rays, diffracted rays, and scattered rays [29, 30]. These ray types are related to the real propagation mechanisms of LOS propagation, transmission, reflection, diffraction, and scattering, respectively [29].

Direct rays. The direct rays are those that have direct propagation from the transmitter (Tx) to the receiver (Rx) without obstructions [29, 30]. These rays are modelled and calculated using the Friis equation [52].

Transmitted and reflected rays. The transmitted (reflected) rays are defined as rays encounter one or multiple transmission(s) (reflection(s)) at interfaces between different mediums before reaching the field point [29, 30]. The propagation direction is calculated based on the Snell's Law [36], and the magnitude of the transmitted (reflected) field is calculated by Fresnel equation for different polarisations [53].

Diffracted rays. Diffracted rays are typically caused by diffraction from mountain peaks and ridges, or generally from the "knife-like" edges of objects [54–56]. Instead of the direct, transmitted, and reflected rays, the diffracted rays are more complicated, since one incident ray can spawn many diffracted rays under the diffraction [29]. Initially the diffraction is modelled by geometrical theory of diffraction (GTD) [57], and currently most ray-based methods use uniform theory of diffraction (UTD) to model the diffraction during the propagation [58–62].

Scattering. The scattered rays are caused by rough surfaces of objects that the rays impinge on, resulting in the reflected energy being diffused in all directions [41]. Scattering may arise from various objects, including trees [63–66], building facades [67–70], lampposts [71, 72], and vehicles [71–73].

Basic Ray Tracing Algorithms

We here review the basic algorithms for ray tracing methods, including the Fermat's principle of least time [74], the image method [29], and the shooting and bouncing ray (SBR) method [29, 75]. Detailed explanation can be found in [29].

Fermat's principle of least time. This algorithm is one of the fundamental components of ray-based models, defining the path of a ray travelling from the source to the field point [74]. It states that a ray will follow the propagation path that takes the least time to travel from one point to another [29]. This principle forms the theoretical basis for deriving the laws of transmission, reflection, and diffraction.

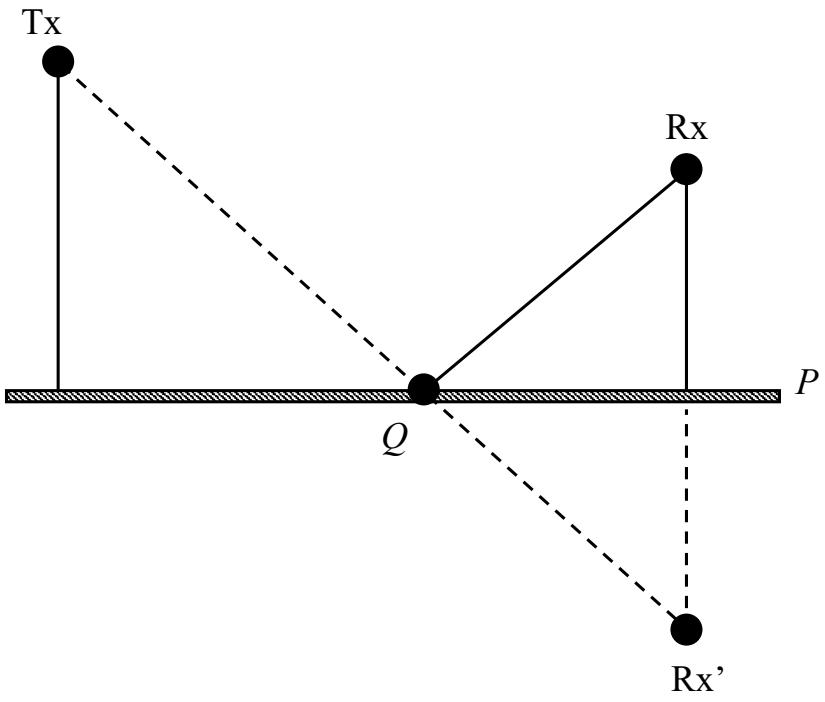

Fig. 2.1 Example of the image method [29]. Rx' is the image of Rx with respect to the reflection surface *P*.

Image method. To determine the exact path for reflected rays, the image method is proposed [29, 30]. An example of the image method is shown in Fig 2.1 [29]. After the locations of Tx and Rx are given, we can: First, define the image of Rx, Rx', with respect of the planar reflection surface P; second, connect Tx and Rx' and find the intersect point Q on the surface P; and finally, define the route of reflection as Tx-Q-Rx.

Shooting and bouncing ray (SBR) method. The SBR method was initially proposed to compute the radar cross section of cavities [29, 75]. The key idea of the SBR method is to trace the rays launched from the Tx and determine whether they reach the Rx. The typical steps of the SBR method includes ray launching, ray tracing, and ray reception [29]. Briefly, ray launching from an isotropic source requires a uniform distribution of launching method, where each emitted ray carries approximately equal power [76]. The ray tracing step involves the aforementioned ray types, which are generated within the propagation environment. In the ray reception step, the algorithm determines whether a ray covers the field point, thereby confirming its arrival.

2.1.2 Full Wave Solutions

Another class of deterministic models is the full wave solutions. These methods involve more detailed simulations of channels based on Maxwell's equations and are significantly more computationally intensive than ray-based methods. Typical full wave solutions include the FDTD [21–23], the FEM [24, 25], the MoM [26, 27], and the FIT [28]. Due to their extremely high computational complexity, these methods have used far less frequently than ray-based models. For wireless channel modelling, these methods are only used for simple indoor scenarios [77]. Instead, they are widely used for modelling antenna patterns [32], electromagnetic body effects [33], electromagnetic object structures [34], and electromagnetic scattering problems [35], which fall outside the scope of this thesis.

2.2 Stochastic Channel Models

In this section, we review another type of channel modelling method, which is based on statistics and named as stochastic channel model. The current stochastic channel models can be classified as measurement/simulation-based stochastic channel models (in Section 2.2.1), and theory-based stochastic channel models (in Section 2.2.2).

2.2.1 Geometry-Based Stochastic Channel Models

For the mainstream stochastic models, GSCMs are developed based on measurements and/or simulations, using statistical distributions across different scenario types. Here, we briefly review the most popular GSCM channel models, including the WINNER II channel model [4], the 3GPP channel model [5], the QuaDRiGa channel model [7, 8], the 5GCMSIG channel model [9], the mmMAGIC channel model [10], the METIS channel model [11], the IMT-2020 channel model [12], the COST 2100 channel model [13], the MiWEBA channel model [39], and the NYUSIM [14]. A family history of the GSCMs are shown in Fig. 2.2 [10].

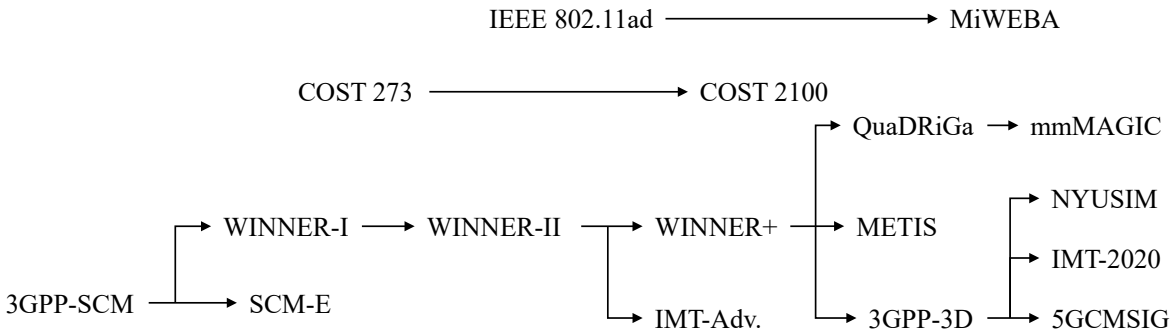

Fig. 2.2 Family history of the current GSCMs [10].

WINNER II channel model. Based on the initial 3GPP spatial channel model (3GPP-SCM) [6] and WINNER I [78] channel models, the WINNER II channel model [4] was proposed and considered the foundation of current stochastic channel models. It defines a standard process for constructing a two-dimensional (2D) GSCM, including environment and propagation setup, measurement-based LSP generations, cluster-based SSP generations, and the construction of CIRs and channel matrices [4]. The overall channel parameters

are calculated based on different distributions, which are observed from measurements. For different scenarios, the same modelling approach is used, but with scenario-specific parameters. These parameters are summarised in tables and organised according to the scenario types covered by the model [4].

3GPP channel model. The 3GPP channel model reported in TR 38.901 [5] extends the WINNER II model [4] to a three-dimensional (3D) version, supporting a wide frequency range (from 0.5-100 GHz) and a large bandwidth (up to 10% of carrier frequency) [3]. For the 3D channel model, the 3GPP channel model establishes the generation of zenith angular spread of arrival (ZSA) and zenith angular spread of departure (ZSD) during the LSP generation step, and subsequently generates zenith angle of arrival (ZOA) and zenith angle of departure (ZOD) during the cluster-based SSP generation. Beyond that, it defines the standard scenario types–UMa, UMi, RMa, and InH–each with LOS and NLOS environments. The corresponding parameters for these scenario types are based on, or closely aligned with, those used in the WINNER II channel model [5, 10].

QuaDRiGa channel model. The QuaDRiGa model, an open-source 3GPP-3D-like channel model, was developed by the Fraunhofer Heinrich Hertz Institute [7, 8]. It further enhances spatial consistency for moving user equipments (UEs) in massive multiple input multiple output (MIMO) and multi-cell transmissions by introducing 2D LSP correlation maps and supporting time evolution [79] via mechanisms such as UE trajectories, segmentation and transitions [4], and channel drifting [80].

5GCMSIG channel model. The 5GCMSIG model further extends the 3GPP-3D channel model using extensive measurements and ray-tracing simulations for frequencies from 6 to 100 GHz [3, 9, 10]. Its channel modelling strategy is closely aligned with those of the WINNER II [4], 3GPP-3D [5], and mmMAGIC [10] channel models. Moreover, for LSP generations, it offers multiple path loss models including the CI, CIF, and ABG models, along with additional measurement-and/or-simulation-based values of LSPs (i.e., the Ricean K-factor, DS, and AS) under different scenario types. Besides, it extends the standard scenarios defined by the 3GPP-3D channel model [5], such as UMi street canyon, InH shopping mall, and stadium [3, 9].

mmMAGIC channel model. Taking the QuaDRiGa channel model [7, 8] as a basis, the mmMAGIC channel model [10] is another extension of the 3GPP-3D channel model [5]. The mmMAGIC project added more measurement campaigns, including 6, 10, 14, 28, 41, 60, 82, and 100 GHz, to further support the mmMAGIC channel model that is built upon the QuaDRiGa channel model structure [10]. It also supports mmWave channel modelling via new modelling approaches, including frequency-dependent LSPs, more realistic cluster-based SSP generations, and so on [3, 10].

METIS channel model. The METIS model includes a stochastic channel model based on the 3GPP-3D model, a map-based channel model constructed using ray-tracing simulations with simplified propagation environments, and a hybrid model that combines both approaches [11]. For the stochastic channel model, the METIS framework supports frequency ranges up to 70 GHz and is capable of modelling device-to-device (D2D)/vehicle-to-vehicle (V2V) scenarios with time evolution [3, 11].

IMT-2020 channel model. The IMT-2020 channel model [12] is another extension of the 3GPP-3D channel model, featuring a wide frequency range of up to 100 GHz, large bandwidth, spatial consistency, blockage modelling, and so on [3]. It also proposes two extension modules as alternatives for generating channel parameters: the time-spatial propagation (TSP) model for frequency below 6 GHz, and the map-based hybrid model for frequency above 6 GHz [3, 11, 12].

COST 2100 channel model. Stemming from the COST 273 model [81], the COST 2100 channel model [13] runs in parallel to the framework of the 3GPP-3D channel models. It introduces the concept of visibility regions (VRs), which impact the activation and deactivation of clusters along the trajectory of a moving UE and their contributions to the overall channel simulations [3], to model radio channels under different scenarios. Compared to the 3GPP-like channel models, the concept of clusters is more detailed in the COST 2100 channel model [3, 13].

MiWEBA channel model. Unlike the fully stochastic modelling approach used in the 3GPP-3D channel model [5], the MiWEBA channel model characterises channels via the quasi-deterministic (Q-D) method [37–39]. It models the channel multipath components as

D-rays and R-rays [3], using different modelling approaches for each. D-rays, which account for the major portion of the received power (e.g., dominant components such as the LOS path and single- or double-bounce reflections), are modelled deterministically using ray-based methods and environmental information. R-rays, representing weaker components (e.g., NLOS paths and signals transmitted/reflected/diffracted/scattered from multiple obstacles), are modelled using random clusters characterised by statistical parameters, which are similar to the stochastic modelling approaches [3, 10].

NYUSIM. NYUSIM is developed by the group of Prof Theodore S. Rappaport in New York University, USA [14]. It was created based on the measurements from 28 GHz to 140 GHz to cover channel modelling at mmWave and sub-THz. The NYUSIM supports channel modelling with a frequency range of 0.5-150 GHz for all 3GPP-listed scenarios, such as UMa, UMi, RMa, InH and indoor factory (InF) scenarios. Also, compared to the 3GPP channel model, the NYUSIM provides a more comprehensive and accurate realization of the radio channel [14].

2.2.2 Theory-Based Stochastic Channel Models

Instead of relying on measurement-based parameters [4–13], another type of stochastic channel model uses mathematical equations to theoretically model the CIRs [30, 49, 50, 82]. It should be noted that some works refer to them as geometry-based stochastic models (GBSMs) [30, 49, 50], while others conflate the concept of GBSMs with GSCMs [3, 82]. At the current stage, we prefer to classify them into two sub-types of stochastic channel models: GSCMs that stem from measurements and/or simulations (reviewed in Section 2.2.1), and GBSMs that are based on theoretical reasoning and hypotheses [49]. The GBSMs can be further classified into regular-shaped GBSMs [83, 84], and irregular-shaped GBSMs [85, 86].

2.3 Modelling of Radio Channel Large-Scale Parameters Based on Statistics

Since the main topic of this thesis is on statistical channel LSP models, in this section, we review the statistical path loss models (i.e., empirical path loss models) [51], and other LSP models including the Ricean K-factor, DS, and AS [10].

2.3.1 Modelling of Path Loss

For fast path loss predictions in the stochastic channel models, empirical path loss models are raised based on observations and measurements, of which typical empirical models use one formula to characterise certain types of propagation scenarios. Even though the accuracy is sacrificed, these models have been widely used in both research and industrial communities owing to their minimum complexity. Here, we briefly review the most popular path loss models for practical use. In the early stage of empirical path loss modelling, common models include the log-distance path loss model [40, 41], the Okumura-Hata model family [41, 87–93], and the Erceg-Greenstein empirical model family [42, 94, 95]. While currently, models that are widely used in stochastic channel modelling include the CI, CIF, and ABG models [5, 9, 47, 96].

Early Stage of Empirical Path Loss Modelling

Log-distance path loss model. The log-distance path loss model is based on the definitions and properties of path loss, that is, a function of the transmitter-receiver (T-R) separation distance with log-normal distribution [40, 41]. This model simply characterises path loss using measurement-based parameters in decibels, including an intercept at the CI reference distance, a PLE of log-distance for a certain type of area, and a shadow fading term (i.e., a zero-mean normally distributed random variable having a dB scale). Note that the shadow fading term describes the random shadowing effects caused by propagation environments, leading to variations in path loss across links with identical T-R separation distances [41].

Okumura-Hata model. Initially, the Okumura-Hata model was one of the most widely used empirical models for signal strength prediction [41, 87, 88]. It predicts the path loss at urban area and is valid from 150 MHz to 1500 MHz. The Tx antenna height ranges from 30 m to 200 m, and the Rx antenna height ranges from 1 m to 10 m. This model characterises the path loss by a standard formula along with supplied correction equations for application to other environment types (e.g., suburban area). Building upon the Okumura-Hata model, several extensions and corrections have been proposed [51], including the COST-231 model [89], the Hata-Davidson model [90], the ECC-33 model [91], and the rural Hata model [92, 93]. The COST-231 model [41, 89], established by the European COST, extends the Okumura-Hata model with a larger frequency coverage of up to 2 GHz; the Hata-Davidson model [90], proposed by the Telecommunications Industry Association (TIA), introduces corrections to the Okumura-Hata model, especially for high Tx antenna heights up to 2.5 km and long-distance links of up to 300 km [51]; the ECC-33 model [91], developed by Electronic Communication Committee (ECC)-European Conference of Postal and Telecommunications Administrations (CEPT), extends the frequency coverage up to 3.5 GHz; and the rural Hata model [92, 93], defined in the International Telecommunication Union-Radiocommunication Sector (ITU-R) 529 [93], corrects the Okumura-Hata model to address path loss overestimations in rural environments.

Erceg-Greenstein empirical model. The Erceg-Greenstein empirical model was presented by the American Telephone and Telegraph Company (AT&T) Wireless and V. Erceg *et al*. [42]. It specifically characterise the suburban areas at 1.9 GHz using T-R distance and base antenna heights. Further, it defines three different terrain categories within the suburban scenario, which are: Category A that is hilly terrain with moderate-to-heavy tree densities, which results in maximum path loss; Category B that is either flat terrain with moderate-to-heavey tree densities or hilly terrain with light tree densities, which results in median path loss; and Category C that is flat terrain with light tree densities, which results in minimum path loss [42]. Following the strategies of terrain categories defined in the Erceg-Greenstein empirical model, the Stanford University interim model (SUI) [94, 95] is

then developed by both the IEEE 802.16 group and Stanford University, which covers carrier frequencies from 2.5 GHz to 2.7 GHz.

In summary, the aforementioned models are among the earliest empirical path loss models with practical applications. Other early path loss models such as the flat-edge model [97] and the partition model [98, 99] are not included in this subsection, since they are designed for more specific scenarios compared to the three discussed above. More information on early-stage path loss modelling can be found in [51]. Among these earliest empirical path loss models, their limited datasets and specific model structures restrict the broader integration into full channel models, confining their use primarily to path loss prediction.

Current Empirical Path Loss Models

Even though the early path loss models established a basic vision of path loss modelling, they are either limited in frequencies or tailored to specified scenarios, making them unsuitable for integration into stochastic channel models. Over the past two decades, the CI, CIF, and ABG models have been proposed to support path loss predictions within stochastic channel models [4–13]. Basically, following the radiation-like log-distance model structure, these three models characterise path loss using an additional frequency-dependent coefficient (for large frequency coverage) and apply to different scenario types (for wide and general deployment). These models cover frequencies from 0.5 GHz to 100 GHz, and the commonly used scenario types include UMa, UMi, RMa, and InH [5, 6, 9]. Also, a composite sensitivity and accuracy analysis of these three models has been investigated by the research group led by Prof Theodore S. Rappaport in [47].

2.3.2 Modelling of Other Large-Scale Parameters

Beyond path loss, stochastic channel models also cover other LSPs in order to construct the final channel matrix, including the Ricean K-factor, DS, and AS [4–13]. Within stochastic channel models, these LSPs are modelled similarly to path loss, but in a more approximate manner. These LSPs follow log-normal distributions and are modelled using measurement-based random variables, with linearly regressed means and standard deviations defined

for different scenario types. In other words, instead of a radiation-based structure varying with log-distance, the entire scenario of interest is described using mean LSP values with associated variations.

Besides, some researchers have proposed and validated log-distance model for these LSPs (i.e., the Ricean K-factor [43, 44], DS [45], and AS[46]). However, these studies are not widely known within the current research community, and their usage remains limited, having not yet been integrated into mainstream stochastic channel models.

Chapter 3

AMPLE: An Adaptive Multiple Path Loss Exponent Radio Propagation Model Considering Environmental Factors

3.1 Introduction

[1][2][3]Over the past decade, research on statistical models has primarily focused on the practical applications of the CI, CIF, and ABG models, with various works including more deployment scenarios, sensitivity analysis, and so on. Still, the limitation of these models, as we discussed in Chapter 1, have constrained further development in this field. Against this background, the AMPLE model is designed to enhance prediction accuracy under the structure of statistical models while maintaining low complexity. In other words, within the statistical model framework, we aim to strike a balance between providing practical model usages with a minimum of computational complexity and including as much detail as possible [42].

[1]The content of this chapter is based on the revised versions of our two publications [16, 17].

[2]© 2025 IEEE. Reprinted, with permission, from **L. Zhou**, J. Zhang, J. Zhang, O. Cetinkaya, and S. A. Jubb, "AMPLE: An adaptive multiple path loss exponent radio propagation model considering environmental factors," *IEEE Trans. Veh. Technol.*, vol. 74, no. 2, pp. 3395-3400, Feb. 2025.

[3]© 2024 IEEE. Reprinted, with permission, from **L. Zhou**, J. Zhang, J. Zhang, and K. Qiu, "An environment-adaptive radio propagation path loss model with ray-based validation," *IEEE Antennas Wireless Propag. Lett.*, vol. 23, no. 10, pp. 3217-3221, Oct. 2024.

In this chapter, we present the AMPLE model, which is a fast radio propagation model considering environmental factors [15–17]. The environment data is first extracted by classifying raster maps into multiple region types, and each region type is labelled with a PLE that can be further determined via measurement and/or simulation. For path loss, a straight line between the Tx and Rx is generated, which records all the intersected regions and the weighted region path loss. The total path loss is computed in decibels by accumulating the weighted path loss of all the intersected regions within the straight line. We also validate the AMPLE model via both measurements and ray-based simulations, and we compare the AMPLE model with the 3GPP path loss model [5] and the ABG model in the 5GCMSIG channel model [9]. The results show that the AMPLE model outperforms these models while having similar model complexity. To the best of our knowledge, this is the first time that the PLEs precisely correspond to different region types in a practical multi-slope model. The current AMPLE model is a prototype which only considers path loss prediction and static environment. Also, this simple-but-accurate model can be integrated into map systems by creating a new path loss attribute for digital maps.

The rest of this chapter is organised as follows. In Section 3.2, we introduce the AMPLE model with details. Section 3.3 provides the validation process of the AMPLE model based on measurements that are collected in Sheffield and Barnsley, both are considered as UMa scenarios. Section 3.4 presents another validation process via ray-based simulations using a measurement-validated commercial ray-tracing simulator. Section 3.5 gives a discussion about the AMPLE model. Finally, Section 3.6 summarises this chapter.

3.2 The AMPLE Model

In this section, we present the construction details of the AMPLE model. A typical modelling process is shown in Fig. 3.1, including measurement and/or simulation, environment recognition, straight line model construction, and characterisation and prediction.

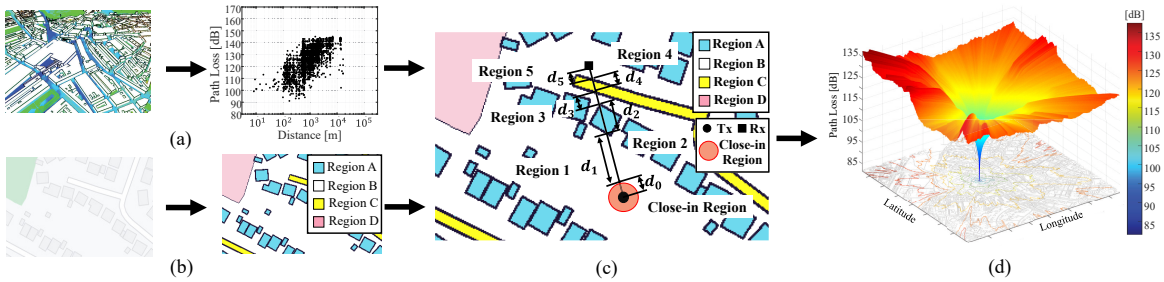

Fig. 3.1 Example of the AMPLE model construction process [16]. (a) Simulation/measurement collection and analysis. (b) Environment collection and classification. (c) Straight line construction. (d) Parameter extraction and path loss prediction.

3.2.1 Preliminary Information

To construct the AMPLE model, both path loss and scenario information are necessary during the model construction stage [16]. For path loss data, similar to other empirical path loss models [5, 6, 9, 47], preliminary path loss data under the desired scenario are collected from ray-based simulations and/or measurements, as illustrated in Fig. 3.1(a). After that, to combine the environmental information and construct a site-specific model, the map information of the scenario is another preliminary model characterisation condition. As shown in Fig. 3.1(b), the AMPLE model utilises the 2D region map to cover environmental information, of which it classifies the whole map into different region types. By using manual classification, map classification based on image processing, or AI-based classification methods, the maps collected from satellite systems, digital map systems, and geographic information systems (GISs) can be therefore transformed.

To combine path loss and map information, each type of region is assigned with a PLE, and a straight line between each T-R link is generated. The straight line records the intersected region PLE as well as the corresponding region length, which can be expressed as [16, 17]

$$\mathbf{S}_z = \begin{bmatrix} n_0 & n_1 & n_2 & n_3 & \cdots & n_{R_z} \\ d_0 & d_1 & d_2 & d_3 & \cdots & d_{R_z} \end{bmatrix}, \tag{3.1}$$

where $\mathbf{S}_z$ is the line matrix of the zth T-R link, n_{R_z} is the PLE of the R_zth region, and d_{R_z} is the corresponding region length. Based on common practice [41, 42], we define regions within

d_0 as the CI region, where d_0 is the CI distance [16, 17]. That is to say, regions within the CI distance are not counted (i.e., $n_0 = 0$). An example of the straight line and the CI region is given in Fig. 3.1(c). Note that the straight line is irrelevant to the LOS path, since the LOS case may not exist for all the links, and it is just a method to construct the AMPLE model.

3.2.2 The AMPLE Model

Based on the straight line matrix $\mathbf{S}_z$ in (3.1), the decibel characterisation of the AMPLE model for the zth T-R pair can be expressed as

$$\mathrm{PL}_z\,[\mathrm{dB}] = A + \sum_{r=1}^{R_z} 10 n_r \log_{10}\left(\frac{\sum_{k=0}^{r} d_k}{\sum_{k=0}^{r-1} d_k}\right) + \Psi_\sigma, \tag{3.2}$$

where A, R_z, n_r, d_k, and Ψ_σ are characterised as follows.

- ***Intercept*** (A): Within the straight line, A is the decibel path loss of the CI region.
- ***Intersected Regions*** (R_z & n_r): R_z regions in total are intersected within the zth T-R straight line, and n_r is the rth region PLE. Note that for different T-R pairs, R_z may be different as well.
- ***Weighted Path Loss*** (d_k): The weighted path loss of the rth region is computed by the subtraction between the end point path loss of rth and $r-1$th region, respectively [15–17]. Note that d_k is the kth region length.
- ***Shadowing*** (Ψ_σ): Ψ_σ is a normally distributed shadowing term with $N[0, \sigma^2]$ under dB scale.

By combining terms with the same PLE, (3.2) can be simplified as region-type-based, which can be expressed as

$$\mathrm{PL}_z\,[\mathrm{dB}] = A + \sum_{m=1}^{M} D_m n_m + \Psi_\sigma, \tag{3.3}$$

where M is the number of region types within the environment (e.g., $M = 4$ in Fig. 3.1(c)), n_m is the mth region type PLE, and D_m is the corresponding coefficient extracted by combining

like terms of n_m. Also, as the model in dB scale contains a shadowing term with normal distribution $N[0,\sigma^2]$, which means, the total path loss in this case is normally distributed with $N[\mu(A,n_m),\sigma^2]$, where [101]

$$\mu(A,n_m) = A + \sum_{m=1}^{M} D_m n_m. \tag{3.4}$$

Combining (3.2)-(3.4) with measured and/or simulated data, the parameters that construct the model can be extracted using various algorithms. Finally, in Fig. 3.1(d), the path loss prediction can be made based on the extracted model parameters.

3.2.3 Relationship with the Log-Distance Model

From the above description, the AMPLE model is applicable to different scenarios according to different map-measurement/simulation sets. Thus, the quantity M may increase for complex scenario (e.g., multiple region types) and decrease for simple scenario (e.g., a single region type). Specially, for a scenario with a single region type (i.e., $M = 1$), (3.2) will be simplified to the log-distance model in decibels, which is [42]

$$\mathrm{PL}_z\,[\mathrm{dB}] = A + 10n\log_{10}(d/d_0) + \Psi_\sigma \qquad d \geq d_0, \tag{3.5}$$

with

$$\mu(d) = A + 10n\log_{10}(d/d_0), \tag{3.6}$$

where A is the intercept that represents the path loss at CI distance d_0, n is the PLE, and (3.6) is the distance-dependent mean of normal distribution $N[\mu(d),\sigma^2]$ in dB scale.

3.3 Measurement Validation

In this section, we provide a validation process of the AMPLE model in two UMa areas with measurements. We first present the data collection method within the measurement areas. Then, we describe the mapping between the region map and the data coordinates. In addition,

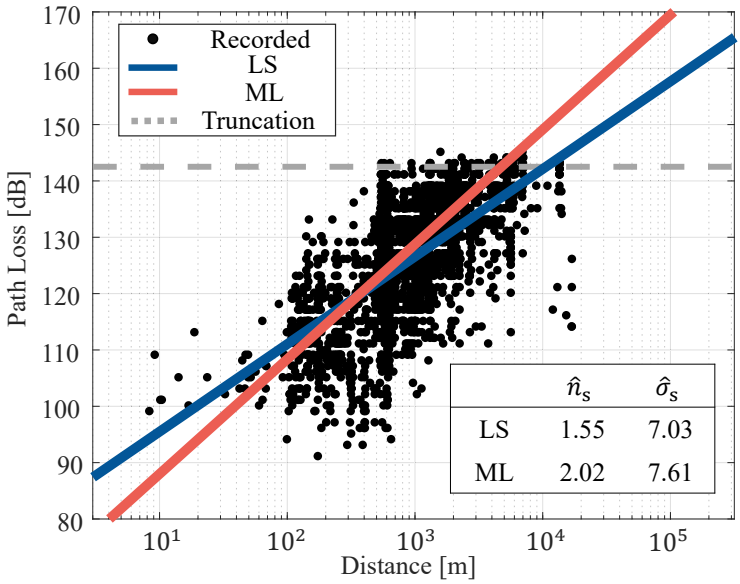

Fig. 3.2 Scatter plot of the measurement in Sheffield, and the estimation results of LS and ML with truncated normal distribution.

the extraction of model parameters based on the truncated data is given. Following that, the AMPLE model is characterised and compared with the 3GPP-UMa model [5, Table 7.4.1-1] and the ABG-UMa model [9, Table 6], and the comparison results and analysis are given.

3.3.1 Measurement Collection

For the measurement data, we consider two scenarios for parameter extraction and model validation, where they have the same propagation conditions. For parameter extraction, the measured data are collected in Sheffield, UK, which is considered a suburban area with hilly terrain, dense buildings, and moderate-to-heavy tree density [42]. We focus on a gateway of Long Range Wide Area Network (LoRaWAN) [102] that accommodates a LORIX One with a 4.15 dBi omnidirectional antenna. It is located on the Hicks Building (53.381029, -1.4864733) of the University of Sheffield, which has a height of 30 m. For the mobile antenna, Sheffield is mapped through "drive test" experiments, which are performed with an autonomous mobile network scanner and field test device (having an antenna gain of 2 dBi), installed on an electric vehicle (an average height of 1.2 m). The received signal strength indicator (RSSI) are periodically recorded, together with the global positioning system (GPS) coordinates. More details of the measurement collection are described in [103]. Overall, the

measurement data collected in Sheffield comprises 4,615 data points transmitted at around 868 MHz, with a transmitted power of 20 dBm. These data are taken at T-R separation distances ranging from several metres to 10 km. Since the antenna gains are included in RSSI [102], the path loss is calculated by subtracting the antenna gains of 6.15 dBi (4.15 dBi for Tx and 2 dBi for Rx) to exclude antenna effects.

Fig. 3.2 shows the scatter plot of 4,615 measured path loss in metres. The gray dashed line shows the truncation of measured data, while two straight lines represent two extraction fit methods based on the log-distance model. Since the Rx has a sensitivity limit, path loss data beyond 142 dB is missing, leading to a bias in the estimated PLE and standard deviation of the shadowing. This is evident in the blue line representing least squares (LS) fit in Fig. 3.2, resulting in $\hat{n_{\mathrm{s}}} = 1.55$ and $\hat{\sigma}_{\mathrm{s}} = 7.03$. To mitigate this, a maximum likelihood (ML) fit with a truncated normal distribution is employed [101, 104]. Based on equations (3.5) and (3.6), the probability density function (PDF) of zth measured path loss is given by [101, 104]

$$P(l_z;\mu(d),\sigma) = \begin{cases} \frac{1}{\sqrt{2\pi}\sigma} \frac{\exp\left(-\frac{(l_z-\mu(d))^2}{2\sigma^2}\right)}{\Phi\left(\frac{L-\mu(d)}{\sigma}\right)} & l_z < L, \\ 0 & \text{else}, \end{cases} \tag{3.7}$$

where L is the right truncated value as 140 dB, and Φ is the cumulative distribution function (CDF) of the standard normal distribution. By using (3.7) to extract the PLE and the standard deviation in the log-distance model, it yields more accurate results: $\hat{n_{\mathrm{s}}} = 2.02$ and $\hat{\sigma}_{\mathrm{s}} = 7.61$, as indicated by the red line in Fig. 3.2.

Meanwhile, for model validation, another set of measurement data is collected in Barnsley, UK, which is considered a similar scenario to Sheffield (i.e., a suburban area). The propagation conditions in Barnsley are also identical to those in Sheffield, including the transmission network, antenna type, collection method, and so on. The gateway in Barnsley is located on the roof of the Barnsley Digital Media Centre (53.5551977, -1.4789376), which has a height of 25 m. The measured path loss data in Barnsley consists of 631 data points, which also suffers truncation during data collection due to device sensitivity, and so that, the same truncation process is applied in this case. Similar to the measurements in Sheffield, as shown in Fig. 3.3, the initial truncated PLE and standard deviation based on LS are $\hat{n_{\mathrm{b}}} = 1.51$

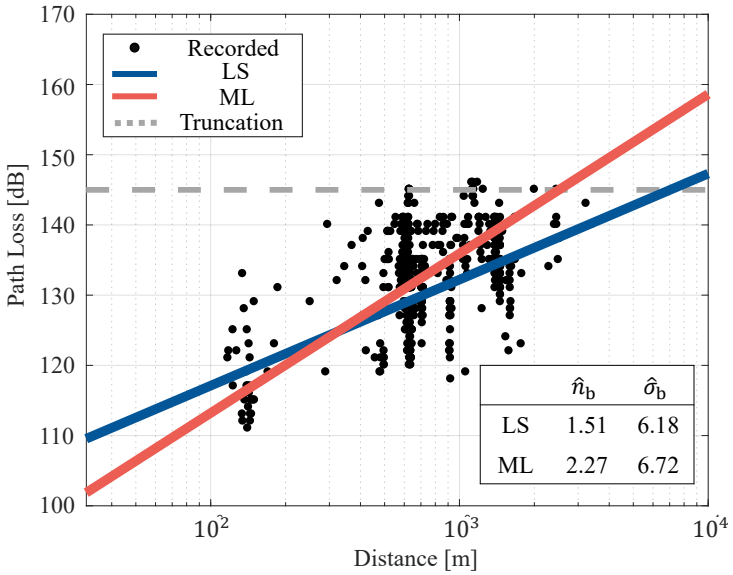

Fig. 3.3 Scatter plot of the measurement in Barnsley, and the estimation results of LS and ML with truncated normal distribution.

and $\hat{\sigma}_b = 6.18$, respectively. After applying the truncation process (i.e., ML estimation with a truncated normal distribution [101, 104]), the PLE and standard deviation are $\hat{n}_b = 2.27$ and $\hat{\sigma}_b = 6.72$, respectively.

3.3.2 Region Classification and Coordinate Mapping

To extract the information of the environment, we collect raster maps of two scenarios from Google Maps, both with a map scale of 50 m and covering an area of approximately 2.25 km^2 (has a side of 2,115 pixels). It should be noted that under the map constraints, 3,128 out of 4,615 measured path loss points are included in Sheffield, and 456 out of 631 measured path loss points are included in Barnsley. For region classification, as shown in Fig. 3.4, we apply k-means clustering to identify regions with the same RGB values, and we combine the regions within the same type manually. While some errors occur during the clustering process, the overall classification results remain acceptable. Finally, the environmental obstacles in the two scenarios are classified into the following region types: *Building*, *OpenSpace*, *Lane*, *WoodedArea* and *Lake*. Taking Sheffield as an example, the original raster map and the classified region map are shown in Fig. 3.5.

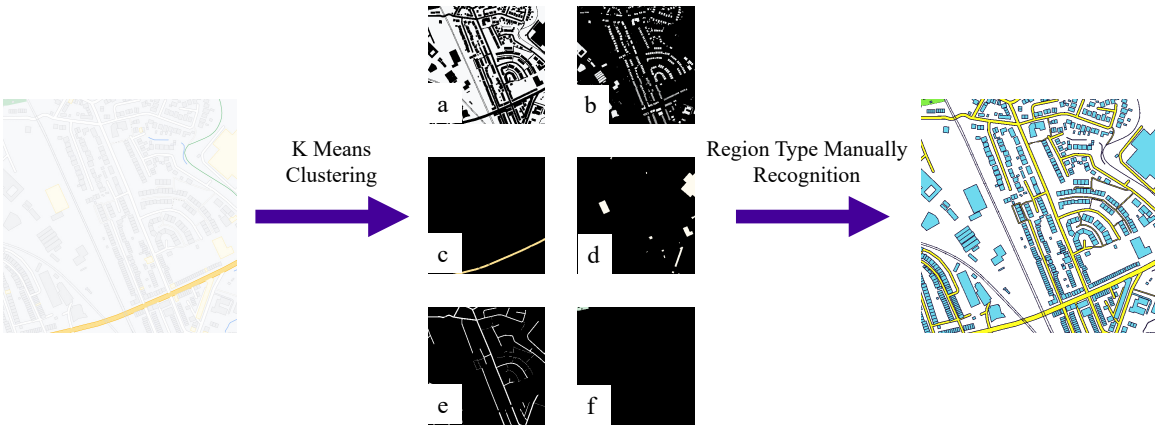

Fig. 3.4 Example of region map classification from 2D raster map, based on k-means clustering and manual recognition.

Since the coordinates of Rx are recorded during experiments, the mapping between region map and measurement is to link the coordinates with the region map. Based on the coordinates of map edges, the coordinate system is established and illustrated in Fig. 3.5, where each pixel can be constrained by its corner coordinates. For each T-R pair, the linear function of coordinates is generated to further record the intersected pixels. With exclusive-or algorithm, the intersected pixels can be finally constructed into the intersected regions.

3.3.3 Parameter Extraction with Truncated Data

By setting region type M as five, we first calculate the PDF of (3.3) to process the truncation by ML with truncated normal distribution, which can be expressed as

$$P(l_z;\mu(A,n_m),\sigma)=\begin{cases}\frac{1}{\sqrt{2\pi}\sigma}\frac{\exp\left(-\frac{(l_z-\mu(A,n_m))^2}{2\sigma^2}\right)}{\Phi\left(\frac{L-\mu(A,n_m)}{\sigma}\right)} & l_z<L,\\ 0 & \text{else},\end{cases} \tag{3.8}$$

where $\mu(A,n_m)$ is expressed in (3.4), and other values in (3.8) are mentioned before. Based on (3.8), the likelihood function can be written as

$$F(\mu(A,n_m),\sigma)=\prod_{z=1}^{Z}\frac{1}{\sqrt{2\pi}\sigma}\frac{\exp\left(-\frac{(l_z-\mu(A,n_m))^2}{2\sigma^2}\right)}{\Phi\left(\frac{L-\mu(A,n_m)}{\sigma}\right)}. \tag{3.9}$$

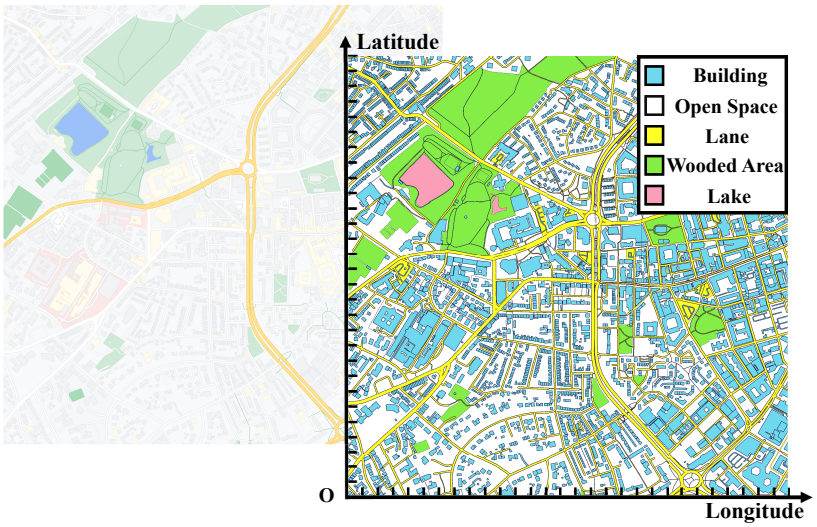

Fig. 3.5 Map classification in Sheffield, from the original raster map to the region map, along with the pixel coordinate system.

To extract the model parameters by ML, the partial derivatives under natural logarithm of (3.9) for all the values are required, including intercept A, PLEs n_m, and the standard deviation σ, which are

$$-\frac{\partial \ln F(n_m,A,\sigma)}{\partial A}=\sum_{z=1}^{Z}\left[\frac{\mu(A,n_m)-l_z}{\sigma^2}-\frac{\exp\left(-\left(\frac{L-\mu(A,n_m)}{\sqrt{2}\sigma}\right)^2\right)}{\sigma\int_{-\infty}^{\frac{L-\mu(A,n_m)}{\sigma}}\exp(-\frac{t^2}{2})dt}\right], \tag{3.10}$$

$$-\frac{\partial \ln F(n_m,A,\sigma)}{\partial n_m}=\sum_{z=1}^{Z}D_m\left[\frac{\mu(A,n_m)-l_z}{\sigma^2}-\frac{\exp\left(-\left(\frac{L-\mu(A,n_m)}{\sqrt{2}\sigma}\right)^2\right)}{\sigma\int_{-\infty}^{\frac{L-\mu(A,n_m)}{\sigma}}\exp(-\frac{t^2}{2})dt}\right], \tag{3.11}$$

and

$$\begin{aligned}-\frac{\partial \ln F(n_m,A,\sigma)}{\partial \sigma}=\sum_{z=1}^{Z}\Bigg[&\frac{1}{\sigma}-\frac{(\mu(A,n_m)-l_z)^2}{\sigma^3}\\&-\frac{(L-\mu(A,n_m))\exp\left(-\left(\frac{L-\mu(A,n_m)}{\sqrt{2}\sigma}\right)^2\right)}{\sigma^2\int_{-\infty}^{\frac{L-\mu(A,n_m)}{\sigma}}\exp(-\frac{t^2}{2})dt}\Bigg],\end{aligned} \tag{3.12}$$

where Z is the total data points (i.e., $Z=3{,}128$). Based on (3.10)-(3.12), the above parameters are combinatorially optimised by gradient descent with suitable step size.

3.3.4 Results and Analysis

Table 3.1 Model Parameters in the Measurement Area

Environmental Factors	**Variables**	**Values [dB]**
Intercept	A	81.54
In-Building	n_1	1.07
Open Space	n_2	1.71
Lane	n_3	2.45
Wooded Area	n_4	4.79
Lake	n_5	1.08
Standard Deviation	σ	6.97

By setting d_0 to 1 m in (3.1) and applied the AMPLE model in Sheffield, the numerical values of PLEs are estimated combinatorically based on (3.8)-(3.12), and shown in Table 3.1. Also, the physical analysis of these numerical values are given as follows.

- ***In-Building***: The predominance of teaching buildings and student accommodations in the measurement area, characterised by features like long corridors, induces an in-building waveguide effect. These factors contribute to significantly lower in-building PLE compared to a measured case that is 1.57 [105].

- ***Open Space***: For the measured base station, it is located at the top of Hicks Building, which is situated at the hillside. Combined with the waveguide effect caused by other buildings, n_2 is lower than 2.

- ***Lane***: For constantly moving vehicles (e.g., cars, buses and trams) on lanes that cause reflection, diffraction and scattering during the measurement [41], the value of n_3 is larger than 2.

- ***Wooded Area***: The intensive scattering caused by trees leads to severe loss, so the value of n_4 goes beyond 4.

- ***Lake***: When propagating over lakes at 868 MHz, the Sommerfeld-Zenneck surface waves are generated which is 10-20 dB stronger than space waves [106], [107]. That

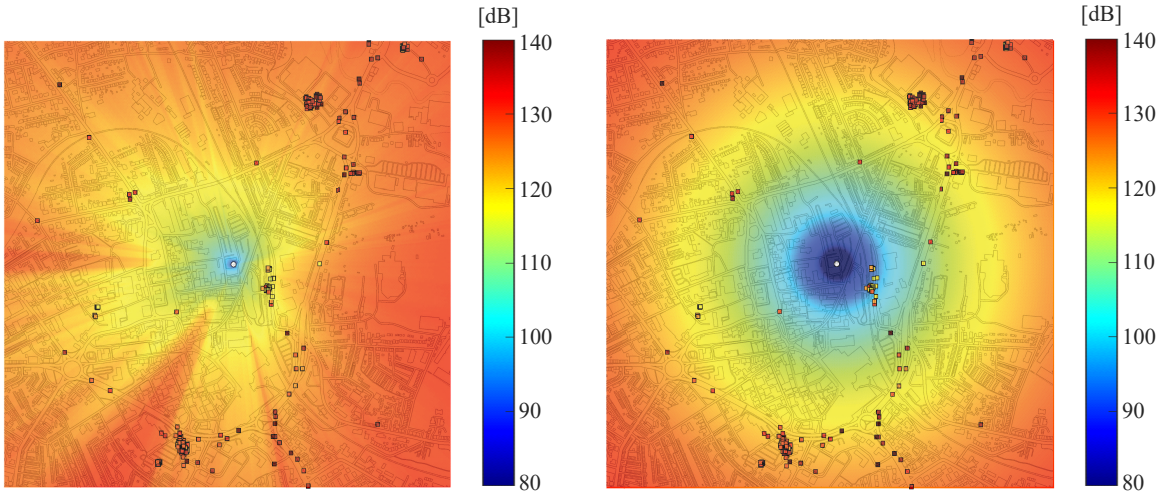

(a) (b)

Fig. 3.6 Heat maps of the path loss prediction results predicted by (a) the AMPLE model and (b) the 3GPP-UMa model, in comparison with the measurements (shown as squares in the heat maps) in Barnsley.

is, the signal decays as the quantity of n_5 because it propagates over the lake surface as a circle instead of radiating through the air as a sphere.

Based on PLEs in Table 3.1 which are extracted from measurements in Sheffield, we use the AMPLE model to predict the path loss of Barnsley and compare it to the 3GPP-UMa path loss model [5, Table 7.4.1-1]. Note that the base station and user terminal antenna heights are set as 25 m and 1.5 m in 3GPP-UMa [5], respectively. In Fig. 3.6, we draw heatmaps of the two models and compare them with the measurement points in Barnsley, represented by squares with different colours indicating the level of path loss. Generally, by considering the environmental factors within the propagation scenario, the predictions of the AMPLE model are closer to the measurements, in comparison with the 3GPP-UMa model.

To provide a more intuitive comparison, we further deploy the ABG-UMa path loss model [9, Table 6] for the measurement area, and we draw the CDFs to visualise the absolute error between these predictions and the measurements, as shown in Fig. 3.7. Besides, we compute the MAE and the RMSE of those models in decibels (as shown in the bottom right corner of Fig. 3.7). Overall, the prediction of the AMPLE model outperforms the other

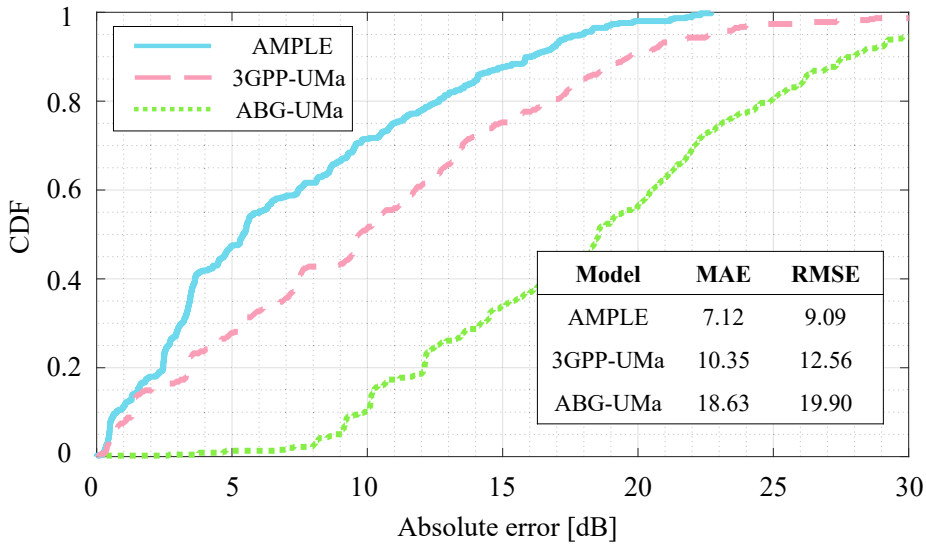

Fig. 3.7 CDF of absolute error between predictions (i.e., AMPLE, 3GPP-UMa, and ABG-UMa) and measurements in Barnsley.

models. The poor performances of both the 3GPP and ABG models may be caused by the measurements we collected [103] and the lack of considering environments.

3.4 Ray-Based Validation

In this section, we apply the AMPLE model to two simulated outdoor scenarios: Scenario A for parameter extraction and Scenario B for model validation. We first introduce the two scenarios simulated by Ranplan Professional, along with basic information of radio propagation. Then, we describe the method for extracting the parameters of the AMPLE model under the simulation of Scenario A. The comparison results are made in Scenario B, along with explanation and analysis.

3.4.1 Outdoor Simulation and Environment Recognition

To validate the AMPLE model, we employ Ranplan Professional to simulate radio propagation in two outdoor scenarios for parameter extraction and model validation. For Ranplan Professional [30, 108–111], it is developed by Ranplan Wireless as a commercial ray tracing simulator, which supports propagation simulations for both the indoor and outdoor envi-

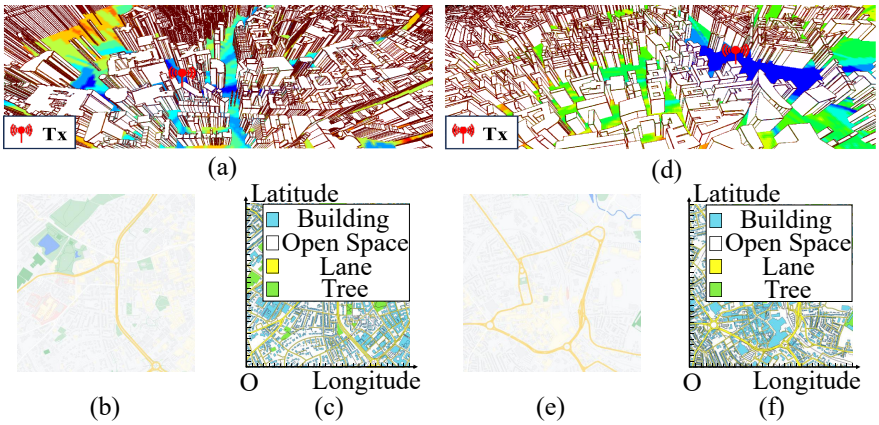

Fig. 3.8 Two simulations with the same propagation conditions, along with environment recognition. (a) Scenario A for parameter extraction. (b) Original map A. (c) Region map A. (d) Scenario B for model validation. (e) Original map B. (f) Region map B.

ronment, and has been used as validations for model characterisations in several works [112–114].

The simulated outdoor scenarios involve two suburban cities in the UK: Sheffield (Scenario A) for parameter extraction and Barnsley (Scenario B) for model validation. Detailed environment features (e.g., buildings, trees, etc.) are imported from EDINA's Digimap Ordnance Survey [115, 116] to reveal the real outdoor information in two cities, as illustrated in Fig. 3.8(a) and Fig. 3.8(d), respectively. Both simulation resolutions are set to 5 m, and the regions of the same type (e.g., buildings) are assumed to have consistent material properties. For the scenario of parameter extraction (i.e., Scenario A), it is bounded by latitudes and longitudes ranging from 53.373579 to 53.387172, and -1.49688 to -1.47412, respectively. The Tx, positioned at a height of 80 m above ground, is located beyond the rooftop of a building at coordinates (53.381029, -1.4864733). Also, the Tx is equipped with an omnidirectional antenna transmitting at LoRaWAN 868 MHz [102], and the Tx power is 20 dBm, along with 0 dBi antenna gains for both Tx and Rx. For the scenario of model validation (i.e., Scenario B), it is bounded by latitudes and longitudes ranging from 53.548515 to 53.561859, and -1.490611 to -1.467880, respectively. Similar propagation conditions are present in Scenario B. Once all the propagation parameters are configured, the path loss across two simulated areas is calculated at 5-m intervals, with an Rx height of 1 m. A total of 91,596 data points for Scenario A and 89,441 data points for Scenario B are respectively collected via simulations,

which are nearly 30-fold than the measurement we previously made in Section 3.3, and without path loss truncation caused by device sensitivity.

For environment recognition, the square maps of Scenarios A and B are collected from Google Maps with a 50-m map scale, and the area of each scenario is about 2.25 km^2, as shown in Fig. 3.8(b) and Fig. 3.8(e), respectively. The map is then classified as *Building, Open Space, Lane*, and *Tree* using k-means clustering with manual region type combinations, and each region type is assigned with a PLE. By using the latitude and longitude boundaries, simulation results can be mapped onto the region map based on the corresponding coordinates (as shown in Fig 3.8(c) and Fig. 3.8(f), respectively), allowing for the generation of straight line matrix $\mathbf{S}_z$ in (3.1) for each T-R link.

3.4.2 Parameter Extraction

Different from the truncated ML due to data truncation (i.e., (3.8)-(3.12)), we consider pure ML to extract the parameters contained in (3.3), and the PDF of the zth link without truncation is written as

$$P(l_z;\mu(A,n_m),\sigma)=\frac{1}{\sqrt{2\pi}\sigma}\exp\bigg(-\frac{(l_z-\mu(A,n_m))^2}{2\sigma^2}\bigg), \tag{3.13}$$

where l_z is the zth T-R link path loss for Z samples (i.e., $Z=91{,}596$ in Scenario A) in total, and $\mu(A,n_m)$ is the mean path loss value, which is expressed in (3.4). The likelihood function can be computed as

$$F(\mu(A,n_m),\sigma)=\prod_{z=1}^{Z}\frac{1}{\sqrt{2\pi}\sigma}\exp\bigg(-\frac{(l_z-\mu(A,n_m))^2}{2\sigma^2}\bigg). \tag{3.14}$$

Then, the partial derivatives under natural logarithm of (3.14) are computed for all parameters in (3.3), including intercept A, PLEs n_m, and standard deviation σ, which can be expressed

as

$$-\frac{\partial \ln F(\mu(A,n_m),\sigma)}{\partial A} = \sum_{z=1}^{Z}\left(\frac{\mu(A,n_m)-l_z}{\sigma^2}\right), \tag{3.15}$$

$$-\frac{\partial \ln F(\mu(A,n_m),\sigma)}{\partial n_m} = \sum_{z=1}^{Z}\left(\frac{(\mu(A,n_m)-l_z)D_m}{\sigma^2}\right), \tag{3.16}$$

$$-\frac{\partial \ln F(\mu(A,n_m),\sigma)}{\partial \sigma} = \sum_{z=1}^{Z}\left(\frac{1}{\sigma}-\frac{(l_z-\mu(A,n_m))^2}{\sigma^3}\right). \tag{3.17}$$

Following (3.15)-(3.17), those parameters can be extracted together by gradient descent, which is omitted here.

3.4.3 Results and Analysis

Based on the ray-tracing simulation of Ranplan Professional in Scenario A, we extract the AMPLE model following (3.15)-(3.17), and apply it to the simulation results of Scenario B for fair validation. We then compare its performance with the ABG model in the 5GCMSIG channel model under the UMa scenario case [9, Table 6], and the 3GPP model for the UMa scenario as well [5, Table 7.4.1-1].

For the prediction results, the heat maps of three models in comparison with the simulation in Scenario B are shown in Fig. 3.9. Note that the error maps in Fig. 3.9(e), Fig. 3.9(f), and Fig. 3.9(g) represent the absolute error between the model prediction results and simulation in Scenario B, which is computed as $|l_o(x,y)-\hat{l_o}(x,y)|$, where $l_o(x,y)$ and $\hat{l_o}(x,y)$ denote the simulation in Scenario B and the model prediction at the spatial point (x,y), respectively. Throughout the three error maps, the AMPLE model demonstrates better prediction performance, especially compared to the 3GPP-UMa model. The three models show similar predictions when the Rxs are close to the Tx. However, as the T-R separation distances increase, the impact of environmental complexities significantly interferes with the predictions of path loss models that do not account for these factors. These interferences are evident in both the ABG-UMa and 3GPP-UMa models but are effectively mitigated by the AMPLE model.

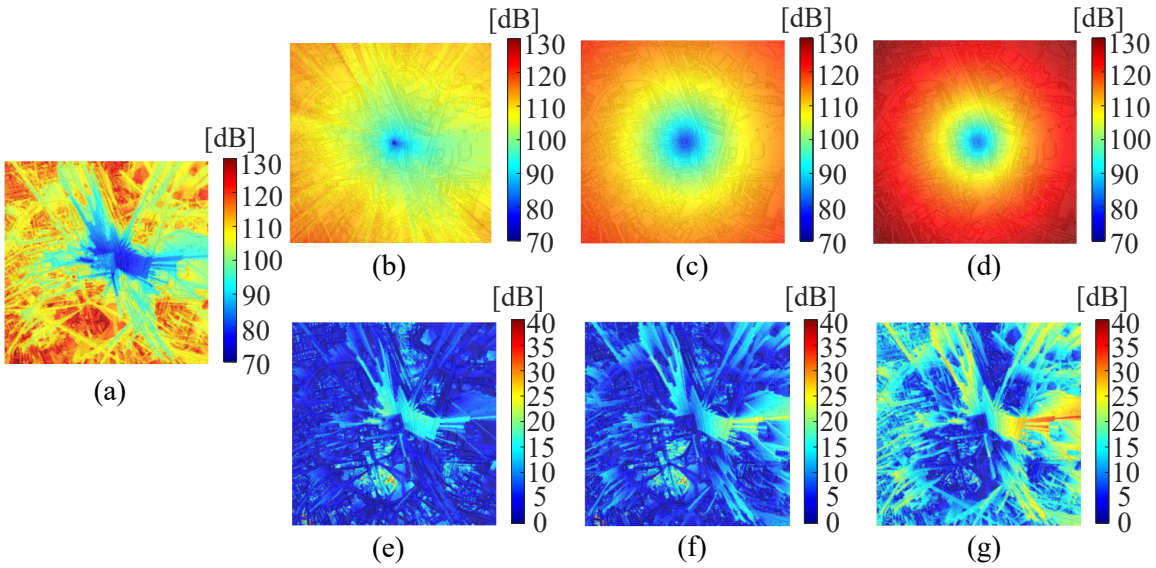

Fig. 3.9 Comparison of path loss heat maps under the simulated area, with the error maps depicting the absolute errors between the three models and Ranplan Professional simulation. (a) Simulation of Scenario B. (b) AMPLE. (c) ABG-UMa. (d) 3GPP-UMa. (e) AMPLE error map. (f) ABG-UMa error map. (g) 3GPP-UMa error map.

Table 3.2 Performance of Models

Model	MAE [dB]	RMSE [dB]	Mean Simulation Time [s]
AMPLE	5.75	7.43	0.136
ABG-UMa	7.20	8.80	0.138
3GPP-UMa	12.84	14.51	0.228

To provide a more intuitive comparison along with the model complexity, we compute the MAE and the RMSE of the three models in decibels with respect to 89,441 simulation data points using the same computer, as shown in Table 3.2. All three models are run 10 times to compute the mean simulation time on a typical office computer (central processing unit (CPU): Intel (R) Core (TM) i5-10505 3.20 GHz; random-access memory (RAM): 16.0 GB 2133 MHz) with MATLAB-R2022a programming environment. Moreover, we draw the CDFs to visualise the absolute error between the path loss models and simulation results, which are shown in Fig. 3.10. Overall, the path loss prediction of the AMPLE model outperforms the ABG-UMa and 3GPP-UMa path loss models.

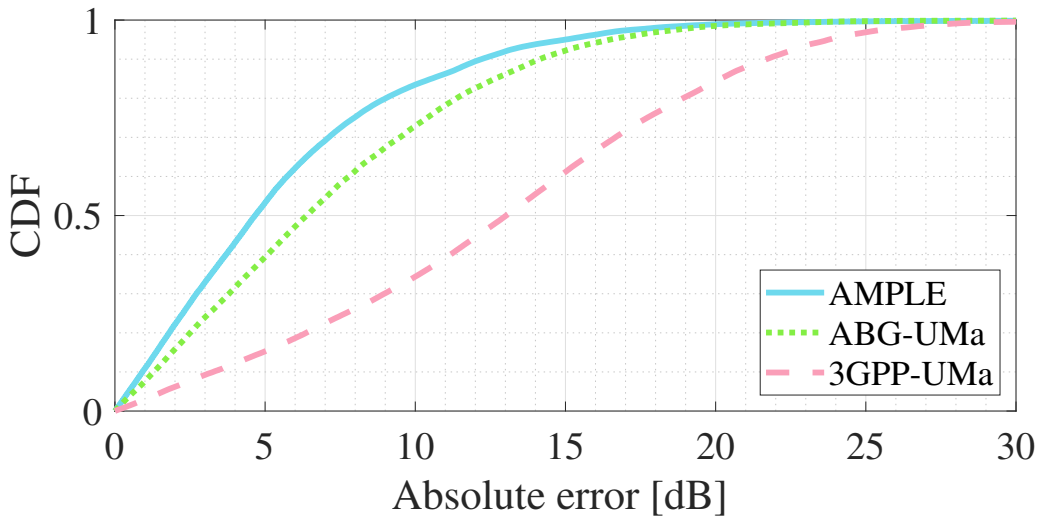

Fig. 3.10 CDF of absolute error between three predictions (i.e., the AMPLE, ABG-UMa and 3GPP-UMa models) and Ranplan Professional simulation.

3.5 Discussion of Similar Model Design

3.5.1 Multi-Slope Models: Distance or Weighted Distance?

For traditional multi-slope models with multiple region types, path loss is computed directly based on distance, with additional losses added at break points between slopes to maintain model continuity [117–120]. However, for practical applications, especially in scenarios involving multiple region types, each transition between region types requires a distinct loss assignment (e.g., transitions between region types A, B, C, and D require six separate and unique losses). That is, as the complexity of environment increases, the number of losses for transitioning between region types grows, in addition to the PLEs for each region type. As a result, for such model type, the most commonly used model in practice is the dual-slope model only, which consists of a single break point dividing the model into two parts that roughly correspond to LOS and NLOS scenarios.

Instead, by directly addressing the impact of region types to path loss (i.e., weighted path loss for intersected regions, calculated by weighted distance), there is no need to consider the discontinuity since the path loss is calculated by weight. So that, the model is largely simplified and can be deployed in multiple region types practically, along with the direct and

precise relationship of "path loss–PLEs", instead of the indirect and rough "distance–PLEs" relations.

Also, from the weighted distance in the parenthesis of (3.2), the 2D distance can be potentially replaced by 3D distance (i.e., consider antenna height), as a simple ratio relation between hypotenuse and adjacent and the cancellation within that parenthesis based on trigonometric functions.

3.5.2 Partition-Based Path Loss Model Versus the AMPLE Model

Considering the similar model construction of the partition-based path loss model [98, 99], we hereby classify the differences between these two models. For partition-based path loss model [98, 99], it counts the real penetration losses within one link based on measurements (as described in the Abstract of [99]), which is the root of the idea. The model characterisation is expressed as [99, Eq. (5)]

$$PL = 20\log_{10}(d) + a \times X_a + b \times X_b \cdots, \tag{3.18}$$

where a, b, etc., are the numbers of each penetration type between Tx and Rx, and X_a, X_b, etc., are their respective penetration losses in decibels [98, 99]. In (3.18), it contains one PLE (with a general case of 2) with multiple penetrations of objects lying between one link. That is, the key design of this model is the accumulation of multiple penetrations based on log-normal distribution. However, one PLE with multiple penetrations of obstacles are hard to deploy for various scenarios, especially for long-distance transmission with complex environments, since those penetrations need to be measured one by one. That is why the partition-based model is for in-home and residential areas.

For the AMPLE model, (3.2) and (3.3) contain multiple PLEs for the corresponding region types. That is to say, we define the mapping relationship between the number of region types within the propagation environment and the number of PLEs, where no penetrations are considered within (3.2) and (3.3).

3.6 Summary

In this chapter, we have presented the AMPLE path loss model with multiple PLEs considering environmental factors. We then separately used both measurements and ray-based simulations to validate the AMPLE model. Following that, we compared the AMPLE model with the 3GPP model and the ABG model for path loss predictions. The results showed that the AMPLE model outperforms these models. The AMPLE model can not only be used to obtain fast and accurate path loss predictions, but can also be integrated into map systems by creating a new path loss attribute for digital maps. Therefore, the AMPLE model has the potential for wide applications and will have a significant impact in wireless communications.

Chapter 4

Ray-Based Characterisation of the AMPLE Model From 0.85 to 5 GHz

4.1 Introduction

[1][2]To cover propagation environment with low computational complexity, in Chapter 3 we proposed the AMPLE model and validated using both measurements [16] and ray-based simulations [17]. In this chapter, we enhance the AMPLE model with frequency considerations to improve its practical usages in path loss predictions under different carrier frequencies. It is accomplished by adding a frequency coefficient into the current model, so that the impact of frequencies on path loss predictions arises. Following that, we characterise the AMPLE model from 0.85 to 5 GHz under the UMa and UMi scenarios using ray-based simulations. For the simulation datasets, we imply a simple measurement validation by extracting the CI model parameter from simulations and compare the values that are extracted from measurements reported in [47]. For model construction, we give a standard process to construct the AMPLE model, which can be considered the basis of future AMPLE model generations. Also, we present a comprehensive validation for the AMPLE model. For the

[1]The content of this chapter is based on the revised version of our publication [18].

[2]© 2025 IEEE. Reprinted, with permission, from **L. Zhou**, X. Dong, K. Qiu, G. Yu, J. Zhang, and J. Zhang, "Ray-based characterization of the AMPLE model from 0.85 to 5 GHz," *IEEE Trans. Antennas Propag.*, vol. 73, no. 10, pp. 8174-8188, Oct. 2025.

compared models, we consider the 3GPP path loss model [5], the ABG and CI models from 5GCMSIG [9], and those with simulation calibrations. For performance evaluations, we use the RMSE and the MAE for point-wise evaluations, and the average total hit ratio error (AHRE) for quality evaluations. Beyond that, we propose two new metrics, that are, the PMDE for overall distributional alignment and the mean simulation time per point per round t_p for model complexity. The results show that the AMPLE model outperforms the current empirical path loss models in the GSCMs.

The remainder of this chapter is organised as follows. Section 4.2 introduces the enhanced AMPLE model considering propagation carrier frequencies. Section 4.3 presents the ray-tracing simulations conducted using the measurement-validated Ranplan Professional. In Section 4.4, the characterisation process of the AMPLE model from 0.85-5 GHz is given, along with a performance comparison against other models. Finally, Section 4.5 summarises this chapter.

4.2 The AMPLE Model with Frequency Consideration

Based on the description in Section 3.2, by further considering the propagation carrier frequency as a factor, the decibel path loss of the zth T-R link can be expressed as [15–17]

$$\mathrm{PL}_z\,[\mathrm{dB}] = A + \sum_{r=1}^{R_z} 10 n_r \log_{10}\left(\frac{\sum_{k=0}^{r} d_k}{\sum_{k=0}^{r-1} d_k}\right) + 10\gamma \log_{10}(f_z) + \Psi_\sigma, \tag{4.1}$$

where A, R_z, n_r, d_k, and Ψ_σ are explained in Section 3.2.2, and γ and f_z are characterised as follows.

- ***Frequency*** (γ & f_z): Based on the typical path loss characterisation methods [5, 6, 9, 47], we add a coefficient γ to indicate the dependence of path loss on frequency [47], where f_z denotes the carrier frequency of the zth link in GHz.

By combining terms with the same PLE, (4.1) can be simplified as region-type-based, which can be expressed as

$$\mathrm{PL}_z\,[\mathrm{dB}] = A + \sum_{m=1}^{M} D_m n_m + 10\gamma \log_{10}(f_z) + \Psi_\sigma, \tag{4.2}$$

where M is the number of region types within the environment (e.g., $M = 4$ in Fig. 3.1(c)), n_m is the mth region type PLE, and D_m is the corresponding coefficient extracted by combining terms of n_m.

4.3 Ranplan Professional Ray-Tracing Simulations

In this section, we first introduce the current usage of ray-based simulations and the measurement-validated Ranplan Professional simulator. We then provide the details of simulations for the UMa and UMi scenarios using Ranplan Professional. Following that, we give a simple validation of the collected dataset by extracting model parameters, such as PLE, and comparing them to those obtained from measurements in [47].

4.3.1 Ranplan Professional Ray-Tracing Simulator

With the development of ray-tracing technology, powerful ray-tracing simulators are used for hardware testbed evaluations [121–123], essential 5G technology validations [124], channel model characterisations [125], and so on. These simulators have also been regarded as an alternative data collection method to hardware measurements, due to their ability to generate larger volumes of data while maintaining minor discrepancy from hardware measurement, and are commonly referred to as "ray-tracing measurements" [126]. In other words, for characterisation of channel models, the database can be collected not only from hardware measurements, but also the ray-tracing simulations generated through reliable simulators. In this chapter, we use Ranplan Professional [108], a powerful commercial ray-tracing simulator, to characterise and validate the AMPLE model from 0.85 to 5 GHz. Validated by hardware

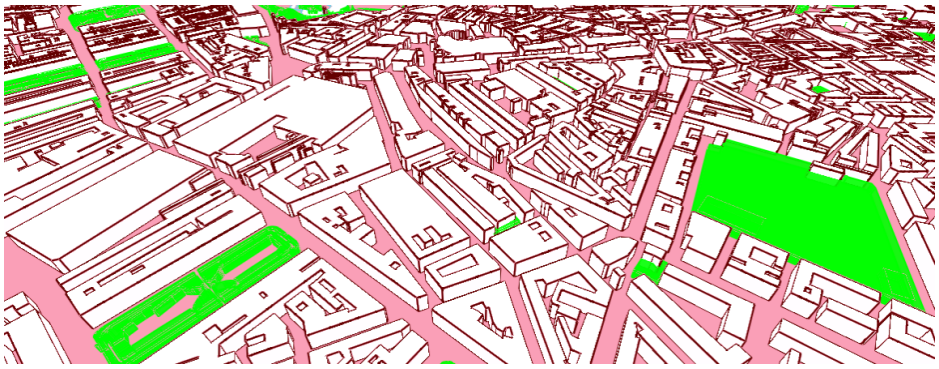

Fig. 4.1 Example of the Ranplan Professional outdoor simulation in London, where pink is open space, white is building, green is foliage, and blue is body of water.

measurements [110, 111], Ranplan Professional has been used to characterise propagation models [17, 112] and support other research in wireless communications [113, 114, 127, 128].

For the model characterisation and validation, we focus on the UMa and UMi for the outdoor scenario types. We consider the 5GNR system frequency bands at 0.85 GHz (5GNR band n5 with 10-MHz bandwidth), 2.1 GHz (5GNR band n1 with 10-MHz bandwidth), and 5 GHz (5GNR band n46 with 10-MHz bandwidth) across both scenario types, and we set up the simulation resolutions as 5 m. An example of the outdoor environment simulation is given in Fig. 4.1, and the detailed propagation information for each scenario simulation is given as follows.

4.3.2 UMa Simulations in Sheffield and Barnsley

For the UMa scenarios, we consider two outdoor simulations that are Sheffield and Barnsley in the UK. Both Sheffield and Barnsley are the typical European style cities that have medium population and building densities. We first import the city layout from EDINA's Digimap Ordnance Survey [116], and we focus on the key environment regions that are general in real-world outdoor scenarios while have a significant impact on radio propagation. Those environment regions include *buildings*, *open space*, *foliage*, and *bodies of water* (lake, river, etc.). The electromagnetic properties of materials used in the simulations, including material type, transmission loss, reflection loss, and diffraction loss, are listed in Table 4.1. The properties of concrete are derived from measurements conducted by Ranplan Wireless as

part of the European project "Wireless Friendly and Energy Efficient Buildings (WiFEEB)" [129], and the properties of bodies of water and foliage are informed by [130, 131]. For the simplification of simulations, we here does not consider adding details into the outdoor scenario, such as road signs and other obstacles that are different in various places and are negligible in comparison to those key regions we covered [16]. Within the simulations, the regions of the same type (e.g., buildings) are assumed to have consistent material properties and heights. Following that, we set foliage with a height of 10 m, and the buildings are made of heavy concrete with a height of 20 m, which is close to the average height in the typical UMa scenarios [5, 47]. For the scenario in Sheffield, it is bounded by latitudes and longitudes ranging from 53.36590854 to 53.39712604, and -1.5114482 to -1.46115222, respectively. In the meantime, the scenario in Barnsley is bounded by latitudes and longitudes ranging from 53.54123619 to 53.56927884, and -1.50333959 to -1.4537181, respectively.

Beyond that, the Txs in both scenarios are equipped with omnidirectional antennas transmitting at 5GNR frequencies of 0.85 GHz, 2.1 GHz, and 5 GHz as previously mentioned, with heights of 30 m [47]. For the exact positions, the Tx in Sheffield is positioned on the rooftop of a building at (53.381029, -1.4864733), and the Tx in Barnsley is positioned on the rooftop of a building at (53.5551977, -1.4789376). Along with that, the Rx is positioned at a height of 1.5 m with a 5-m resolution across the whole outdoor scenarios. The Tx power is

Table 4.1 Electromagnetic Properties of Materials Used in Ranplan Professional, Including Losses [dB] of Transmission, Reflection, and Diffraction [129–131]

Electromagnetic Property	**Frequency**	**Building**	**Body of Water**	**Foliage**
		Concrete	Water	Tree
Transmission	0.85 GHz	10.11 dB	16.16 dB	0.10 dB/m
	2.10 GHz	20.25 dB	25.92 dB	0.30 dB/m
	5.00 GHz	44.35 dB	49.09 dB	0.60 dB/m
Reflection	0.85-5.00 GHz	6.00 dB	1.95 dB	10.20 dB
Diffraction	0.85 GHz	10.26 dB	6.00 dB	-
	2.10 GHz	18.37 dB	14.00 dB	-
	5.00 GHz	38.00 dB	33.00 dB	-

set as 26 dBm, and both Tx and Rx are with 0-dBi antenna gains and with 0-dB cable losses. Based on the environments we set up, we collect a maximum of 823,923 raw data points from Sheffield and 682,803 raw data points from Barnsley across three carrier frequencies.

4.3.3 UMi Simulations in London and Manchester

For UMi scenarios, we simulate London and Manchester in the UK, which are two typical European style UMi cities. We focus on the centre of two cities (i.e., London Soho and the centre of Manchester), that are with high building densities and street canyons. The construction process explained in the UMa scenarios (i.e., Section 4.3.2) is used to set up the environments in two UMi cities (e.g., city layout and environment regions), except that the average building height is set to 10 m [5, 47]. The scenario in London is bounded by latitudes and longitudes ranging from 51.48038 to 51.51303 and -0.16366 to -0.11336, respectively. Also, for scenario in Manchester, it is bounded by latitudes and longitudes ranging from 53.47072 to 53.4978 and -2.27098 to -2.21759, respectively.

For propagation information, the Txs in the UMi scenarios have heights of 15 m (i.e., on the rooftop of a building), with the Tx in London positioned at (51.49474159, -0.14394048), and the Tx in Manchester positioned at (53.48710645, -2.24311856). Other propagation details, such as frequencies, Rx height, Tx power, and so on, are similar to those in the UMa scenarios. Due to the constraints of the UMi scenario, the overall signal coverage is significantly smaller than that of the full simulated environment in both cases. Finally, we collect 482,403 raw data points from London and 482,403 raw data points from Manchester across three carrier frequencies.

4.3.4 Validation Based on the CI Model PLE Extraction

For path loss model characterisation, a reliable dataset can produce similar model parameters (e.g., model PLE) compared to those obtained from measurements under similar propagation conditions recognised by engineers and researchers [5, 9, 47]. Under this way, to validate the simulation results for two scenario types, we compare the CI model parameters extracted

from Ranplan Professional and measurements reported by the research group of Theodore S. Rappaport in [47] (UMa scenario in Aalborg, Denmark, and UMi scenario in New Jersey, USA). In other words, after filtering the simulation data points, we first extract the CI model parameters by the same closed-form solutions as shown in [47, Appendix Eq. (30) & (31)], and we compared the CI values that are extracted by measurements in [47, Table I]. The detailed process is given as follows. Note that for the CI model, it can be expressed as [47]

$$\mathrm{PL}_z^{\mathrm{CI}}(f_z, d_z)\,[\mathrm{dB}] = A(f_z, d_0)\,[\mathrm{dB}] + 10n\log_{10}(\frac{d_z}{d_0}) + \Psi_\sigma^{\mathrm{CI}}, \qquad d_z \geq d_0, \tag{4.3}$$

with

$$A(f_z, d_0)\,[\mathrm{dB}] = 20\log_{10}\left(\frac{4\pi f_z d_0 \times 10^9}{c}\right), \tag{4.4}$$

where $A(f_z, d_0)$ is the free-space path loss in decibels with distance d_0 at carrier frequency f_z in GHz, n is the CI model PLE, and $\Psi_\sigma^{\mathrm{CI}}$ is the shadowing term with $N[0, \sigma^2]$ under dB scale.

To compare with the measurements around 2 GHz in [47], we combine all data points for each scenario type, filter the interference points (e.g., data points beyond a path loss value, such as 150 dB; data points beyond a T-R distance, such as 1.5 km for the UMa scenario, etc.) and extract the path loss data at 5GNR 2.1 GHz. After that, we classify the data points into LOS and NLOS sets based on map information, which is similar to the classification method in [47]. By using closed-form solutions for CI PLE n and standard deviation σ

Table 4.2 Parameters of the CI Path Loss Model Extracted From Ranplan Professional Simulations and Measurements in [47, Table I]. # of Points Refers to the Number of Data Points After Distance Binning and Path Loss Thresholding

Scenario	**Env.**	**Freq. [GHz]**	**Model**	$\boldsymbol{d_0}$ **[m]**	**Data Source**	**# of Points**	**PLE**	$\boldsymbol{\sigma}$ **[dB]**
UMa	LOS	5GNR 2.1	CI	1	Ranplan	12,283	2.26	5.06
		2.0			T. S. Rappaport [47, Table I]	253	2.00	1.70
	NLOS	5GNR 2.1	CI	1	Ranplan	211,996	2.92	10.08
		2.0			T. S. Rappaport [47, Table I]	583	2.80	3.50
UMi	NLOS	5GNR 2.1	CI	1	Ranplan	27,619	2.62	10.31
		2.9			T. S. Rappaport [47, Table I]	18	2.90	2.90

[47, Appendix Eq. (30) & (31)], we extract those values under the UMa LOS, NLOS, and the UMi NLOS, and compared with those extracted from measurements in [47], which are shown in Table 4.2.

Throughout Table 4.2, the CI PLE n extracted from Ranplan Professional is close to those in [47], with a maximum difference below 0.3, whereas the differences of standard deviation σ are large. The reasons of such differences including n and σ can be probably explained as:

- **Number of data points**: As shown in Table 4.2, the number of data points exhibits significant discrepancies between Ranplan Professional simulations and measurements in [47], with a maximum difference exceeding 1,500 fold. A larger number of data points is more likely to result in a higher variance in distribution, leading to an increased σ. Despite this, the PLE values of the two remain close, indicating a high similarity in the path loss trend between simulations and measurements.

- **Frequency**: Differences between propagation carrier frequencies have a non-negligible impact on path loss, which further influences the model values. For example, as shown in the UMi NLOS case, the frequency difference (i.e., a 0.8-GHz difference) is one of the factors contributing to the PLE variation between simulation and measurement.

- **Environment**: Even within the same scenario type, environmental differences may lead to minor variations of model values between different datasets.

Overall, the simulation datasets of Ranplan Professional show high similarity for the CI model PLEs in comparison to those in [47, Table I], and in this chapter, we use these datasets to characterise the AMPLE model.

4.4 Characterisation of the AMPLE Model and Performance Results

In this section, we introduce the process of characterising the AMPLE model based on Ranplan simulations which are presented in Section 4.3. Following that, we briefly introduce

the compared models and the considered performance metrics including the two metrics we defined. Finally, we analyse the results and give the characterisation parameters of the AMPLE model under the UMa and UMi scenarios from 0.85 to 5 GHz.

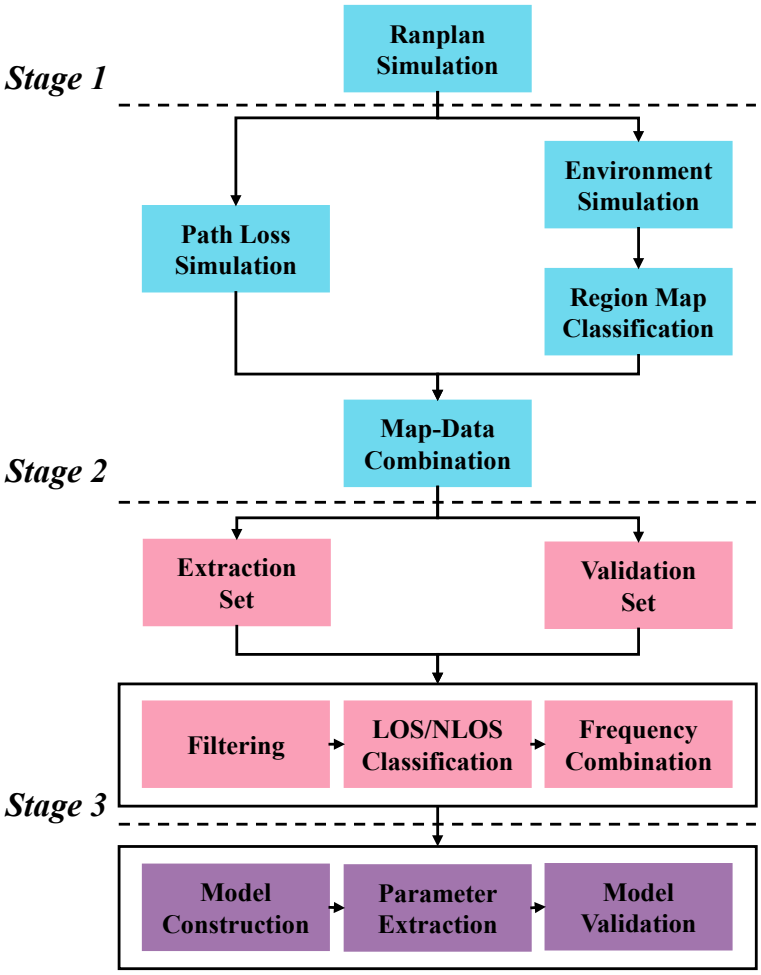

Fig. 4.2 Flowchart of characterisation process based on Ranplan Professional simulations, similar process could be considered for other types of datasets.

4.4.1 Characterisation Process of the AMPLE Model

As shown in Fig. 4.2, the characterisation process of the AMPLE model based on Ranplan Professional can be split into three stages, that is, region classification and map-data combination, simulation data processing, and model constructions.

Stage 1: Region Classification and Map-Data Combination.

Initially, Ranplan Professional contains both environment simulation and the corresponding path loss simulations. Following the environment types we set up as described in Section 4.3.2, we first extract the region maps of those scenarios from Ranplan Professional. By extracting Ranplan Professional simulations as extensible markup language (XML) files, we collect the 2D region maps of four simulated cities, which cover region types including *buildings*, *open space*, *foliage*, and *bodies of water*. To map the path loss data with the generated region maps, we consider the geographical coordinates of the simulated scenarios. That is, by adding latitude/longitude to region maps, each path loss data can be therefore mapped into the region map. The region maps of four scenarios with coordinates are shown in Fig. 4.3.

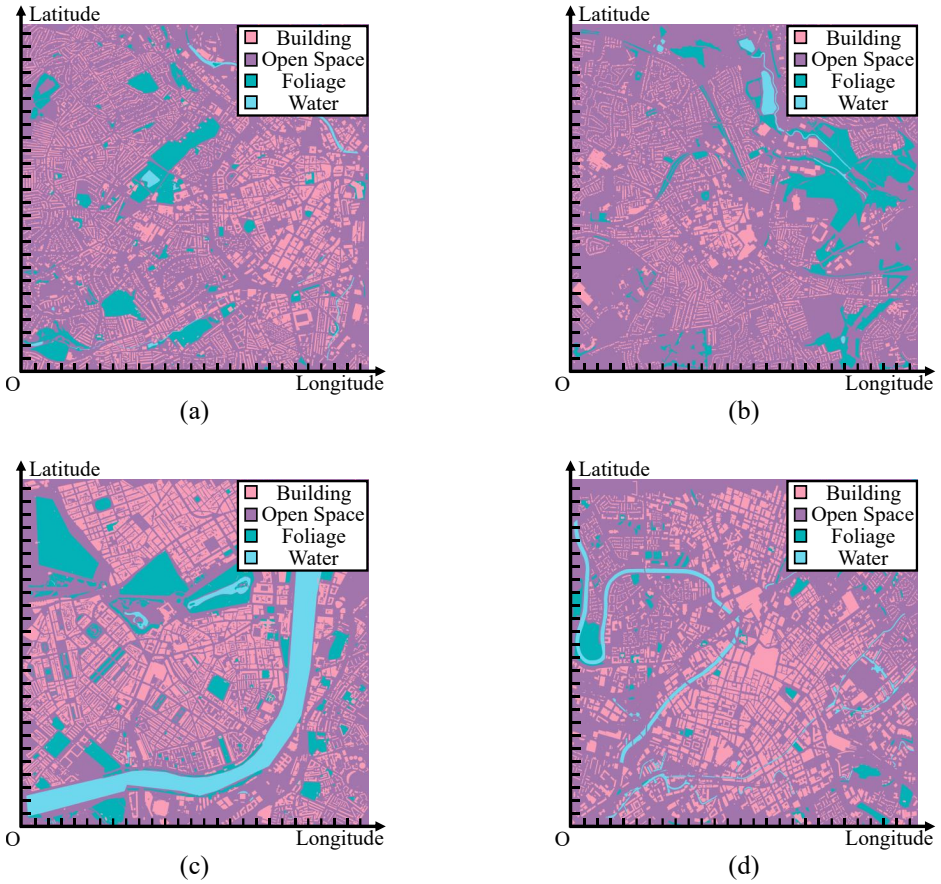

Fig. 4.3 Region maps of (a) Sheffield, (b) Barnsley, (c) London, and (d) Manchester. Along with the classified region types and the geographic coordinates.

Table 4.3 Information of Datasets for Model Extraction and Performance Validation. # of Points Refers to the Number of Data Points After Distance Binning and Path Loss Thresholding

Scenario	City	Set Type	Environment	Frequency Range	# of Points	Distance Range
UMa	Sheffield	Extraction	LOS	0.85-5 GHz	26,730	30-800 m
			NLOS		373,570	35-1,500 m
	Barnsley	Validation	LOS	0.85-5 GHz	36,331	31-800 m
			NLOS		391,134	31-1500 m
UMi	Manchester	Extraction	LOS	0.85-5 GHz	4,431	18-200 m
			NLOS		36,436	18-600 m
	London	Validation	LOS	0.85-5 GHz	3,396	28-200 m
			NLOS		37,109	28-600 m

Stage 2: Data Processing.

To characterise and validate the AMPLE model, the datasets of four cities are split into extraction and validation sets, where an *extraction set* refers to dataset used for model extraction, and a *validation set* refers to dataset used for validating the model performance. We take Sheffield in the UMa and Manchester in the UMi as extraction sets for parameter extraction, and Barnsley in the UMa and London in the UMi as validation sets for model validation. Following the similar filtering and LOS/NLOS classification strategy described in Section 4.3.4, we combine three frequencies together for model characterisation, where the detailed information is listed in Table 4.3.

Stage 3: Model Extraction.

Considering the straight line method described in Section 3.2.1, we construct the model format in (4.2) for each T-R pair. Based on the statistical properties of path loss and shadowing, we extract the desired model parameters including PLEs n_m, intercept A, frequency coefficient γ, and the standard deviation σ. Specifically, we consider ML with gradient descent to extract the parameters of the AMPLE model. As shown in (4.2), the AMPLE model can be computed as

$$\mathrm{PL}_z\,[\mathrm{dB}] = A + \sum_{m=1}^{M} D_m n_m + +10\gamma \log_{10}(f_z) + \Psi_\sigma. \tag{4.2}$$

With the random variable Ψ_σ, the path loss follows a normal distribution, along with $N[\mu(A,n_m,\gamma),\sigma^2]$, where [101]

$$\mu(A,n_m,\gamma) = A + \sum_{m=1}^{M} D_m n_m + 10\gamma \log_{10}(f_z). \tag{4.5}$$

Following that, we first compute the PDF of (4.2), which can be expressed as

$$P(l_z;\mu(A,n_m,\gamma),\sigma) = \frac{1}{\sqrt{2\pi}\sigma}\exp\left(-\frac{(l_z-\mu(A,n_m,\gamma))^2}{2\sigma^2}\right), \tag{4.6}$$

where l_z is the zth path loss value. Then, the joint PDF (i.e., likelihood function) can be expressed as

$$F(\mu(A,n_m,\gamma),\sigma) = \prod_{z=1}^{Z} \frac{1}{\sqrt{2\pi}\sigma}\exp\left(-\frac{(l_z-\mu(A,n_m,\gamma))^2}{2\sigma^2}\right). \tag{4.7}$$

By converting the likelihood function F into its negative natural logarithm form, the problem of finding the optimal parameters can be formulated as minimising this negative log-likelihood function, which can be expressed as

$$\arg\min_{A,n_m,\gamma,\sigma} (-\ln F(\mu(A,n_m,\gamma),\sigma)). \tag{4.8}$$

Because we here use gradient descent to regress these parameters, the partial derivatives of $-\ln F(\mu(A,n_m,\gamma),\sigma)$ with respect to all parameters are required, including PLEs n_m, intercept A, frequency coefficient γ, and the standard deviation σ, which are

$$-\frac{\partial \ln F(\mu(A,n_m,\gamma),\sigma)}{\partial A} = \sum_{z=1}^{Z}\left(\frac{\mu(A,n_m,\gamma)-l_z}{\sigma^2}\right), \tag{4.9}$$

$$-\frac{\partial \ln F(\mu(A,n_m,\gamma),\sigma)}{\partial n_m} = \sum_{z=1}^{Z}\left(\frac{(\mu(A,n_m,\gamma)-l_z)D_m}{\sigma^2}\right), \tag{4.10}$$

$$-\frac{\partial \ln F(\mu(A,n_m,\gamma),\sigma)}{\partial \gamma} = \sum_{z=1}^{Z}\left(\frac{(\mu(A,n_m,\gamma)-l_z)10\log_{10}(f_z)}{\sigma^2}\right), \tag{4.11}$$

$$-\frac{\partial \ln F(\mu(A,n_m,\gamma),\sigma)}{\partial \sigma} = \sum_{z=1}^{Z}\left(\frac{1}{\sigma}-\frac{(l_z-\mu(A,n_m,\gamma))^2}{\sigma^3}\right). \tag{4.12}$$

Note that the initial values of gradient descent are chosen based on our previous works in [16, 17], and the step size is set as 2×10^{-6}.

4.4.2 Information and Calibration of Compared Models

To validate the performance of the AMPLE model, we consider a comparison with other empirical path loss models, including the 3GPP path loss model, the 5GCMSIG CI model (i.e., CI-5GCMSIG), the 5GCMSIG ABG model (i.e., ABG-5GCMSIG), the CI model with extraction-set-based calibration (i.e., CI-Calibrated), and the ABG model with extraction-set-based calibration (i.e., ABG-Calibrated). The 3GPP and 5GCMSIG path loss models are respectively shown in [5, Table 7.4.1-1] and [9, Table 6], and for the CI-Calibrated and ABG-Calibrated models, the calibration process is given as follows.

As shown in (4.3) and (4.4), the CI model can be expressed as [9, 47]

$$\mathrm{PL}_z^{\mathrm{CI}}(f_z,d_z)\,[\mathrm{dB}] = 20\log_{10}\left(\frac{4\pi f_z\times 10^9}{c}\right)+10n\log_{10}\left(\frac{d_z}{1\,\mathrm{m}}\right)+\Psi_\sigma^{\mathrm{CI}}. \tag{4.13}$$

Based on the extraction set for the UMa/UMi scenarios and LOS/NLOS environments, we construct the CI-Calibrated model using the same method employed to characterise the AMPLE model, and the details are given as follows.

With random variable $\Psi_\sigma^{\mathrm{CI}}$, the mean of the CI model is

$$\mu(n) = 20\log_{10}\left(\frac{4\pi f_z\times 10^9}{c}\right)+10n\log_{10}(d_z). \tag{4.14}$$

Following that, the PDF of the CI model is

$$P(l_z;\mu(n),\sigma) = \frac{1}{\sqrt{2\pi}\sigma}\exp\left(-\frac{(l_z-\mu(n))^2}{2\sigma^2}\right). \tag{4.15}$$

By combining all data points, the likelihood function is written as

$$F(\mu(n),\sigma)=\prod_{z=1}^{Z}\frac{1}{\sqrt{2\pi}\sigma}\exp\left(-\frac{(l_z-\mu(n))^2}{2\sigma^2}\right). \tag{4.16}$$

Similarly, the parameters within the CI model can be treated as minimising the negative natural logarithm of (4.16), which is

$$\arg\min_{n,\sigma}(-\ln F(\mu(n),\sigma)). \tag{4.17}$$

Therefore, the partial derivatives of $-\ln F(\mu(n),\sigma)$, including CI PLE n and standard deviation σ, can be computed as

$$-\frac{\partial \ln F(\mu(n),\sigma)}{\partial n}=\sum_{z=1}^{Z}\left(\frac{(\mu(n)-l_z)10\log_{10}(d_z)}{\sigma^2}\right), \tag{4.18}$$

$$-\frac{\partial \ln F(\mu(n),\sigma)}{\partial \sigma}=\sum_{z=1}^{Z}\left(\frac{1}{\sigma}-\frac{(l_z-\mu(n))^2}{\sigma^3}\right). \tag{4.19}$$

We choose the initial values of both n and σ based on [9, Table 6], and we set the step size of gradient descent as 2×10^{-6}.

Meanwhile, for the ABG model, it can be expressed as [9, 47]

$$\mathrm{PL}_z^{\mathrm{ABG}}(f_z,d_z)\,[\mathrm{dB}]=10\alpha\log_{10}\left(\frac{d_z}{1\,\mathrm{m}}\right)+\beta+10\gamma^{\mathrm{ABG}}\log_{10}\left(\frac{f_z}{1\,\mathrm{GHz}}\right)+\Psi_\sigma^{\mathrm{ABG}}, \tag{4.20}$$

where α is the model PLE, β is the intercept, and γ^{ABG} is the frequency coefficient. With random variable $\Psi_\sigma^{\mathrm{ABG}}$, the mean of the ABG model is

$$\mu(\alpha,\beta,\gamma^{\mathrm{ABG}})=10\alpha\log_{10}\left(\frac{d_z}{1\,\mathrm{m}}\right)+\beta+10\gamma^{\mathrm{ABG}}\log_{10}\left(\frac{f_z}{1\,\mathrm{GHz}}\right). \tag{4.21}$$

Following that, the PDF of the ABG model is

$$P(l_z;\mu(\alpha,\beta,\gamma^{\mathrm{ABG}}),\sigma)=\frac{1}{\sqrt{2\pi}\sigma}\exp\left(-\frac{(l_z-\mu(\alpha,\beta,\gamma^{\mathrm{ABG}}))^2}{2\sigma^2}\right), \tag{4.22}$$

Along with all data points, the likelihood function can be expressed as

$$F(\mu(\alpha,\beta,\gamma^{\mathrm{ABG}}),\sigma)=\prod_{z=1}^{Z}\frac{1}{\sqrt{2\pi}\sigma}\exp\left(-\frac{(l_z-\mu(\alpha,\beta,\gamma^{\mathrm{ABG}}))^2}{2\sigma^2}\right). \tag{4.23}$$

Similarly, the parameters within the ABG model can be formulated as minimising the negative natural logarithm of (4.23), and can be expressed as

$$\arg\min_{\alpha,\beta,\gamma^{\mathrm{ABG}},\sigma}(-\ln F(\mu(\alpha,\beta,\gamma^{\mathrm{ABG}}),\sigma)). \tag{4.24}$$

In the meantime, the partial derivatives of $-\ln F(\mu(\alpha,\beta,\gamma^{\mathrm{ABG}}),\sigma)$ including PLE α, intercept β, frequency coefficient γ^{ABG}, and the standard deviation σ can be computed as

$$-\frac{\partial \ln F(\mu(\alpha,\beta,\gamma^{\mathrm{ABG}}),\sigma)}{\partial\alpha}=\sum_{z=1}^{Z}\left(\frac{(\mu(\alpha,\beta,\gamma^{\mathrm{ABG}})-l_z)10\log_{10}(d_z)}{\sigma^2}\right), \tag{4.25}$$

$$-\frac{\partial \ln F(\mu(\alpha,\beta,\gamma^{\mathrm{ABG}}),\sigma)}{\partial\beta}=\sum_{z=1}^{Z}\left(\frac{(\mu(\alpha,\beta,\gamma^{\mathrm{ABG}})-l_z)}{\sigma^2}\right), \tag{4.26}$$

$$-\frac{\partial \ln F(\mu(\alpha,\beta,\gamma^{\mathrm{ABG}}),\sigma)}{\partial\gamma^{\mathrm{ABG}}}=\sum_{z=1}^{Z}\left(\frac{(\mu(\alpha,\beta,\gamma^{\mathrm{ABG}})-l_z)10\log_{10}(f_z)}{\sigma^2}\right), \tag{4.27}$$

$$-\frac{\partial \ln F(\mu(\alpha,\beta,\gamma^{\mathrm{ABG}}),\sigma)}{\partial\sigma}=\sum_{z=1}^{Z}\left(\frac{1}{\sigma}-\frac{(l_z-\mu(\alpha,\beta,\gamma^{\mathrm{ABG}}))^2}{\sigma^3}\right). \tag{4.28}$$

For the LOS and NLOS environments, the initial values are based on [47, Table III] and [9, Table 6], respectively. The step size of gradient descent is set as 2×10^{-6}.

4.4.3 Performance Metrics

For performance metrics, we consider RMSE and MAE to assess the point-wise performance of model, and average total hit ratio error (AHRE) to evaluate prediction quality of path loss [132–134]. Further, we define prediction-measurement distribution error (PMDE) to evaluate the overall alignment between prediction and measurement via statistical distributions, and mean simulation time per data point to measure model complexity.

Point-Wise Evaluation.

For the RMSE, it can be computed as

$$\text{RMSE} = \sqrt{\sum_{z=1}^{Z} \frac{(\hat{l}_z - l_z)^2}{Z}}, \tag{4.29}$$

where Z is the total number of data points, $\hat{l}_z$ is the zth predicted path loss, and l_z is the zth simulated path loss. For the MAE, it can be expressed as

$$\text{MAE} = \sum_{z=1}^{Z} \frac{|\hat{l}_z - l_z|}{Z}. \tag{4.30}$$

Quality Evaluation.

For the AHRE [133], it is defined based on the total hit rate (THR) [132]. For the THR, given a path loss threshold L_T, a prediction is considered correct if both the predicted path loss value $\hat{l}_z$ and the simulated/measured path loss value l_z are either greater than, less than, or equal to L_T, regardless of the deviation between $\hat{l}_z$ and l_z [134]. The AHRE represents the average deviation from the 100% THR and is defined as [132–134]

$$\text{AHRE} = \frac{1}{N_{L_T}} \sum_{L_T = L_{T,\min}}^{L_{T,\max}} (100\% - \text{THR}(L_T)), \tag{4.31}$$

where N_{L_T} is the number of THR points, L_T is the path loss threshold. In this paper, we set $L_{T,\min} = 80$ and $L_{T,\max} = 100$ for LOS environments, and $L_{T,\min} = 100$ and $L_{T,\max} = 120$ for NLOS environments in both the UMa and UMi scenarios, as most path loss values are concentrated within these ranges. Additionally, this method is useful for evaluating the validity of a model in cases where coverage is defined solely by a threshold value. Note that a smaller AHRE indicates better model prediction accuracy [132–134].

Overall Alignment Evaluation.

To evaluate the model performance from a more comprehensive perspective, we define the PMDE as an overall alignment metric. We first use the Akaike information criterion (AIC) to determine the best-fit distributions for both the predicted and measured (or simulated) datasets [46]. We here consider the candidate distributions including normal, lognormal, gamma, Weibull, Rayleigh, Ricean, and chisquare. By constructing the PDFs for the two datasets, we then compute PMDE as the integral of the absolute difference between the two PDFs. The PMDE can be given as

$$\text{PMDE} = \int_x |f_{\text{p}}(x) - f_{\text{r}}(x)| dx, \tag{4.32}$$

where $f_{\text{p}}(x)$ and $f_{\text{r}}(x)$ are the PDFs of the predicted and measured (or simulated) datasets, respectively. Note that these two PDFs describe the overall distributions of the datasets across the environment, which is fundamentally different from point-based shadow fading that characterises local variations at one fixed location [41].

The PMDE provides a statistically grounded way to evaluate the alignment between model-predicted and measured (or simulated) dataset distributions, going beyond point-wise errors and offering a distribution-level performance metric. Similar to the RMSE and the MAE, the PMDE is a general-purpose metric that can also be applied beyond path loss modelling, wherever distributional similarity between predictions and reference data is of interest. A smaller PMDE indicates a better alignment between prediction and measurement/simulation.

Complexity Evaluation.

For the mean simulation time per data point, we run the models 1,000 times on the same dataset and compute the average simulation time for a single data point within one run. We define the mean simulation time per data point as

$$t_p = \frac{1}{GZ} \sum_{z=1}^{Z} \sum_{g=1}^{G} t_{z,g}, \tag{4.33}$$

where t_p represents the mean simulation time per data point, G is the total execution rounds (i.e., $G = 1{,}000$ in this case), and $t_{z,g}$ denotes the simulation time of the zth data point in the gth execution (or run) of the model. We perform multiple runs instead of a single run and simulate the entire dataset rather than individual data points to mitigate fluctuations in computer performance. In this chapter, we run the models and compute t_p on a typical office computer (CPU: Intel (R) Core (TM) i5-10505 3.20 GHz; RAM: 16.0 GB 2133 MHz) with MATLAB-R2024b programming environment.

4.4.4 Results and Analysis

Table 4.4 Performance of Models under UMa Barnsley and UMi London From 0.85 to 5 GHz

Scenario	Environment	Metric	3GPP	CI [9]	CI-Calibrated	ABG [9]	ABG-Calibrated	AMPLE
UMa	LOS	RMSE [dB]	5.95	9.52	5.07	N/A	4.77	4.67
		MAE [dB]	4.58	8.10	4.23		3.88	3.68
		AHRE [%]	16.56	31.44	15.79		14.67	14.06
		PMDE	0.34	1.02	0.15		0.12	0.51
		t_p [ns]	110.51	13.12	12.91		12.46	9.00
	NLOS	RMSE [dB]	15.34	11.05	11.43	10.75	11.35	9.43
		MAE [dB]	12.91	9.47	9.81	9.12	9.63	7.81
		AHRE [%]	21.21	19.05	19.57	18.01	18.87	15.41
		PMDE	1.02	0.77	0.80	0.63	0.71	0.56
		t_p [ns]	117.40	15.45	15.49	13.26	13.41	11.4
UMi	LOS	RMSE [dB]	11.52	12.16	6.86	N/A	6.29	4.49
		MAE [dB]	10.71	11.39	5.78		5.02	3.65
		AHRE [%]	37.95	39.89	23.15		20.39	14.45
		PMDE	1.33	1.37	0.83		0.97	0.26
		t_p [ns]	117.01	25.44	24.88		24.84	25.12
	NLOS	RMSE [dB]	13.58	13.69	10.91	13.58	10.85	9.15
		MAE [dB]	11.54	11.71	8.17	11.54	7.93	6.54
		AHRE [%]	35.51	36.31	26.15	35.51	25.45	20.35
		PMDE	0.93	1.00	0.69	0.93	0.73	0.56
		t_p [ns]	130.65	13.47	13.48	13.44	12.95	9.95

As shown in Table 4.4, the performance of the models is evaluated using the metrics introduced in Section 4.4.3. Generally, the AMPLE model outperforms the current empirical

path loss models used in the GSCMs [5, 9], while maintaining the same level of simulation time, that is, the same model complexity. Note that when computing the simulation time t_p in (4.33), similar to other empirical models, we consider the map information within the AMPLE model as pre-information (i.e., similar to simulated/measured path loss data) during model construction (as shown in Fig. 4.2 and explained in Section 4.4.1). Moreover, we draw the CDFs to visualise the absolute error between the model predictions and the simulation results under two scenarios (i.e., $|\hat{l}_z - l_z|$), which are shown in Fig. 4.4 and Fig. 4.5.

For the UMa scenario under the LOS environment, the AMPLE model performs similarly to other models. This can be seen in both Table 4.4 and Fig. 4.4(a), where the performance metrics in Table 4.4 and the CDF plot in Fig. 4.4(a) show that the AMPLE model has similar performance compared to other models, such as the ABG-Calibrated model and the CI-Calibrated model. This is because the LOS case involves a simple environment where transmission experiences minimal environmental impact. In such a situation, considering environmental factors has a limited contribution to path loss prediction. However, for the UMa scenario under the NLOS environment, environmental factors such as buildings and foliage cannot be ignored, making their consideration significant in path loss prediction [16, 17]. As shown in Table 4.4, the AMPLE model outperforms other models by considering main environmental factors, which provide more information during path loss predictions, and similar results can also be observed in Fig. 4.4(b). Meanwhile, in the more concentrated and complex UMi street canyon scenario, transmission is subject to greater environmental impacts, making environmental considerations even more crucial for path loss predictions. As a result, the AMPLE model outperforms other models, as shown in Table 4.4 and Fig. 4.5.

Besides, to visually illustrate the performance of the AMPLE model, we present heatmaps and absolute error maps of the models under 0.85 GHz, as shown in Fig. 4.6 and Fig. 4.7 for the UMa and UMi scenarios, respectively. The absolute error map is computed based on the absolute error between the model predictions and Ranplan simulations. For the heatmaps in both scenarios (i.e., Fig. 4.6(b)-(g) and Fig. 4.7(b)-(g)), the predictions follow a radiation-like, distance-based trend under the LOS and NLOS cases, except that the AMPLE model predicts path loss based on both LOS/NLOS environments and environmental factors.

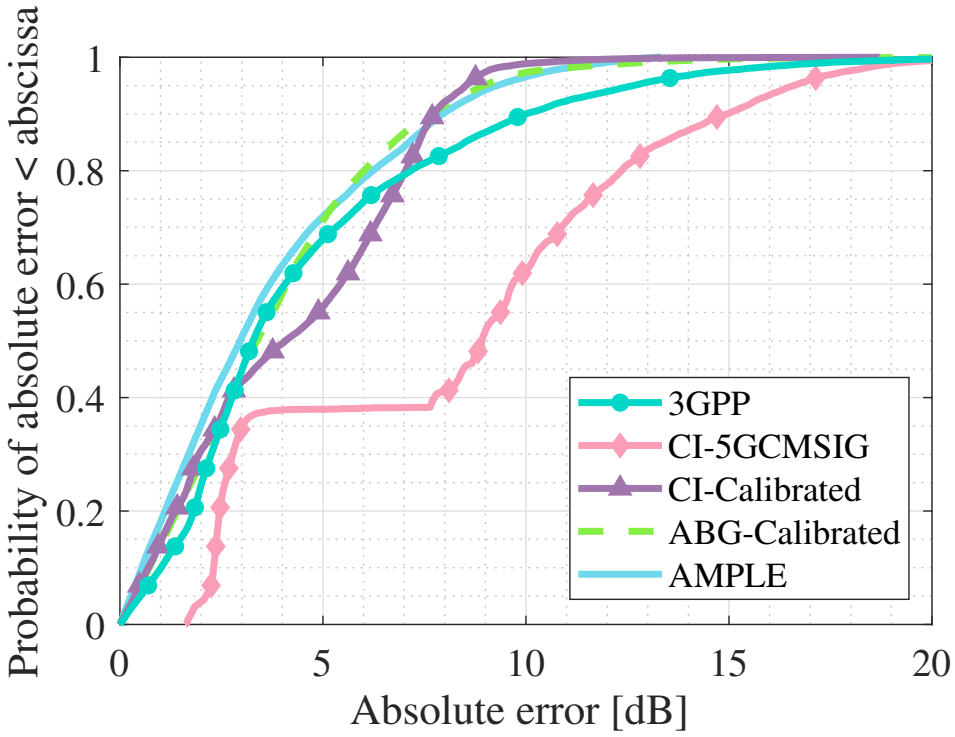

(a)

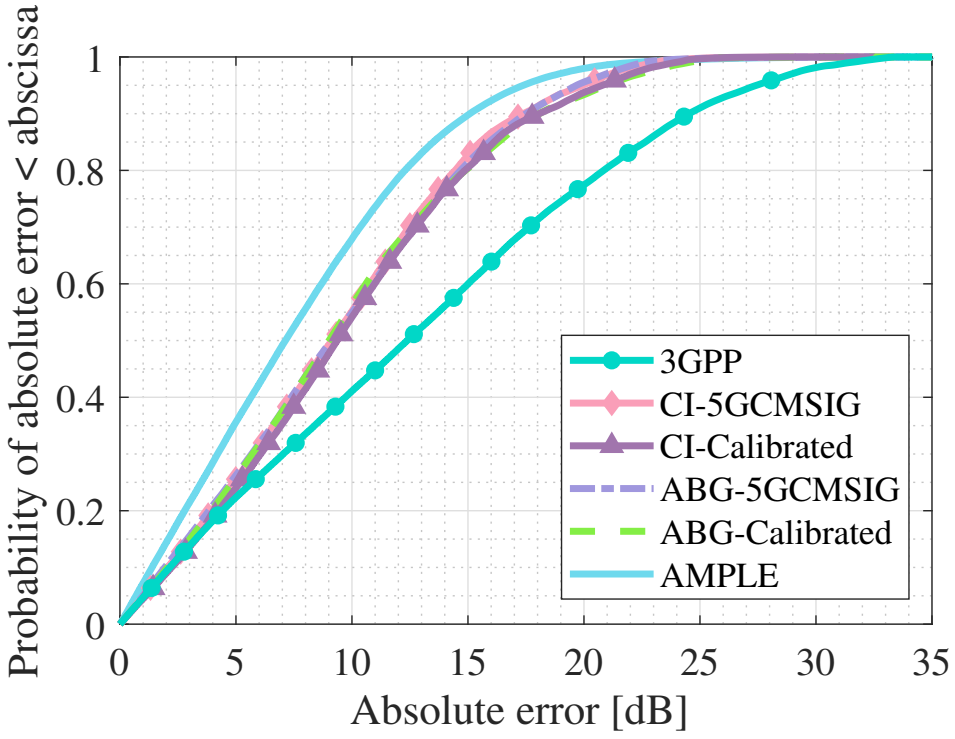

(b)

Fig. 4.4 CDF of absolute error between model predictions and Ranplan Professional simulations under the UMa Barnsley, with (a) the LOS environment, and (b) the NLOS environment.

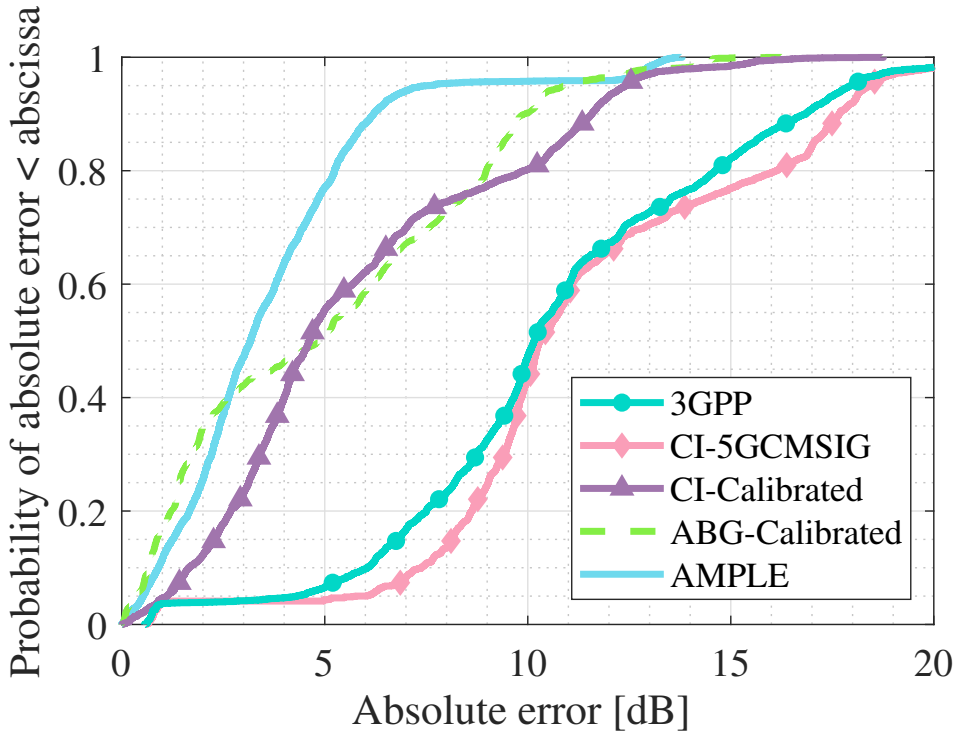

(a)

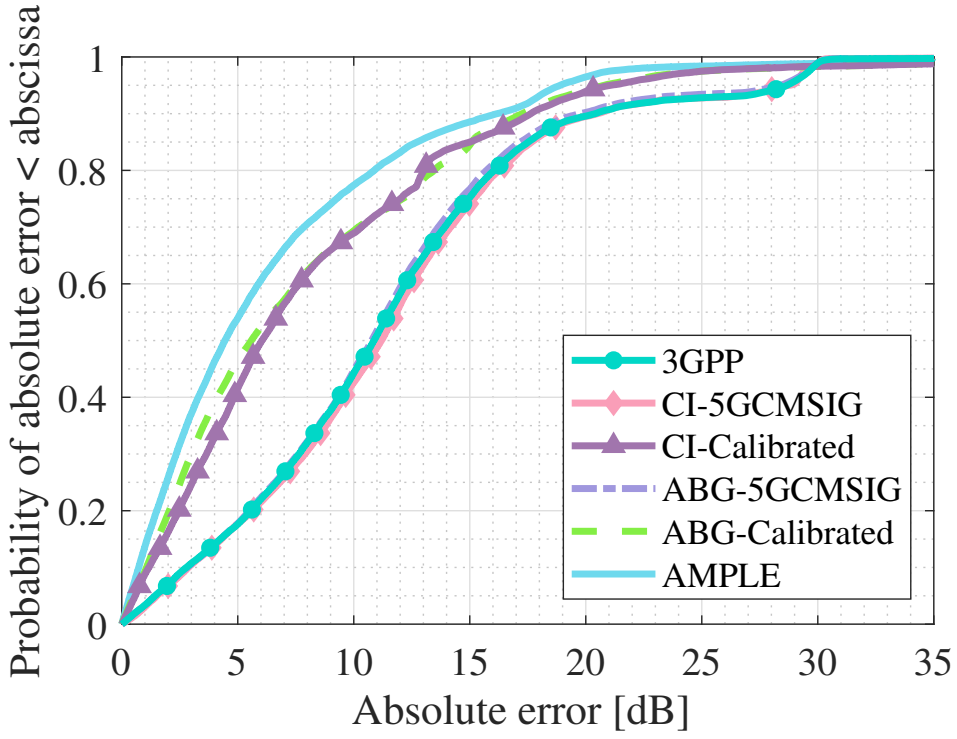

(b)

Fig. 4.5 CDF of absolute error between model predictions and Ranplan Professional simulations under the UMi London, with (a) the LOS environment, and (b) the NLOS environment.

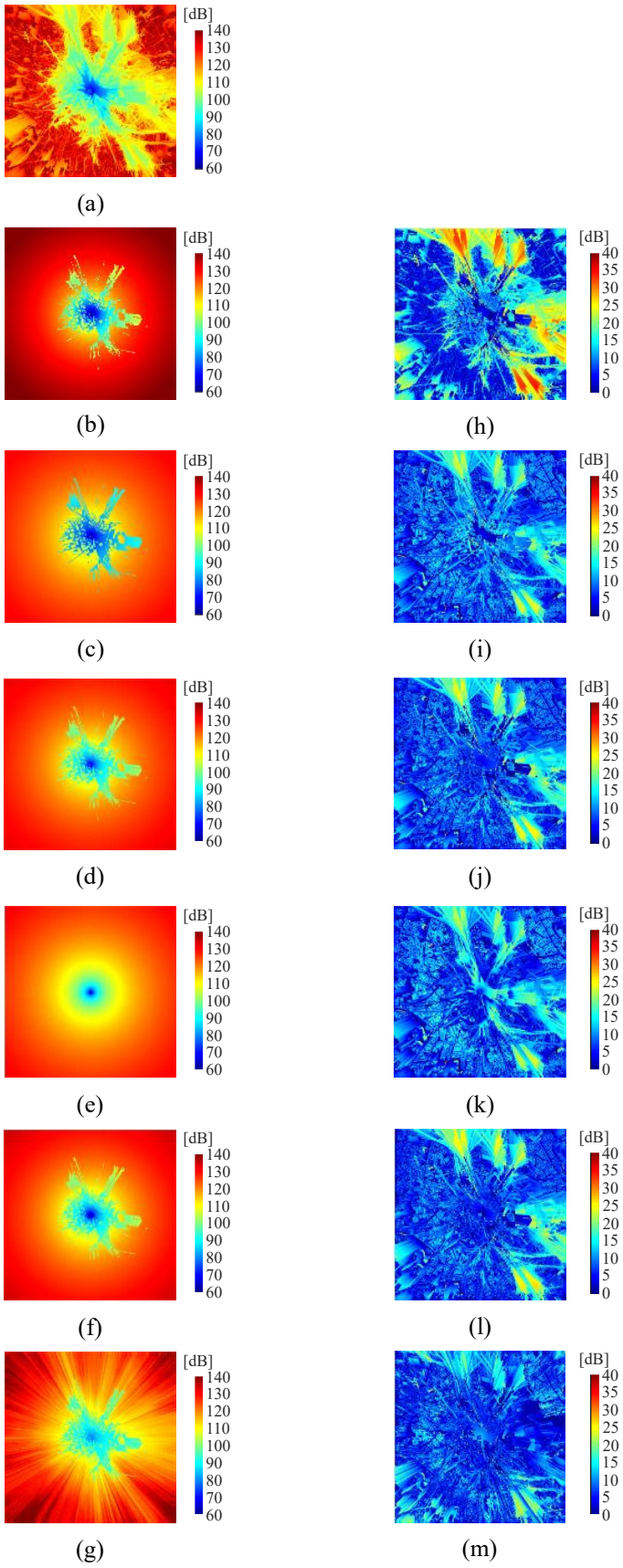

Fig. 4.6 Predictions under the UMa Barnsley 0.85 GHz, which include: Heatmaps for (a) Ranplan Professional simulation, (b) 3GPP [5, Table 7.4.1-1], (c) CI-5GCMSIG [9, Table 6], (d) CI-Calibrated, (e) ABG-5GCMSIG [9, Table 6], (f) ABG-Calibrated, and (g) AMPLE; and absolute error maps for (h) 3GPP, (i) CI-5GCMSIG, (j) CI-Calibrated, (k) ABG-5GCMSIG, (l) ABG-Calibrated, and (m) AMPLE.

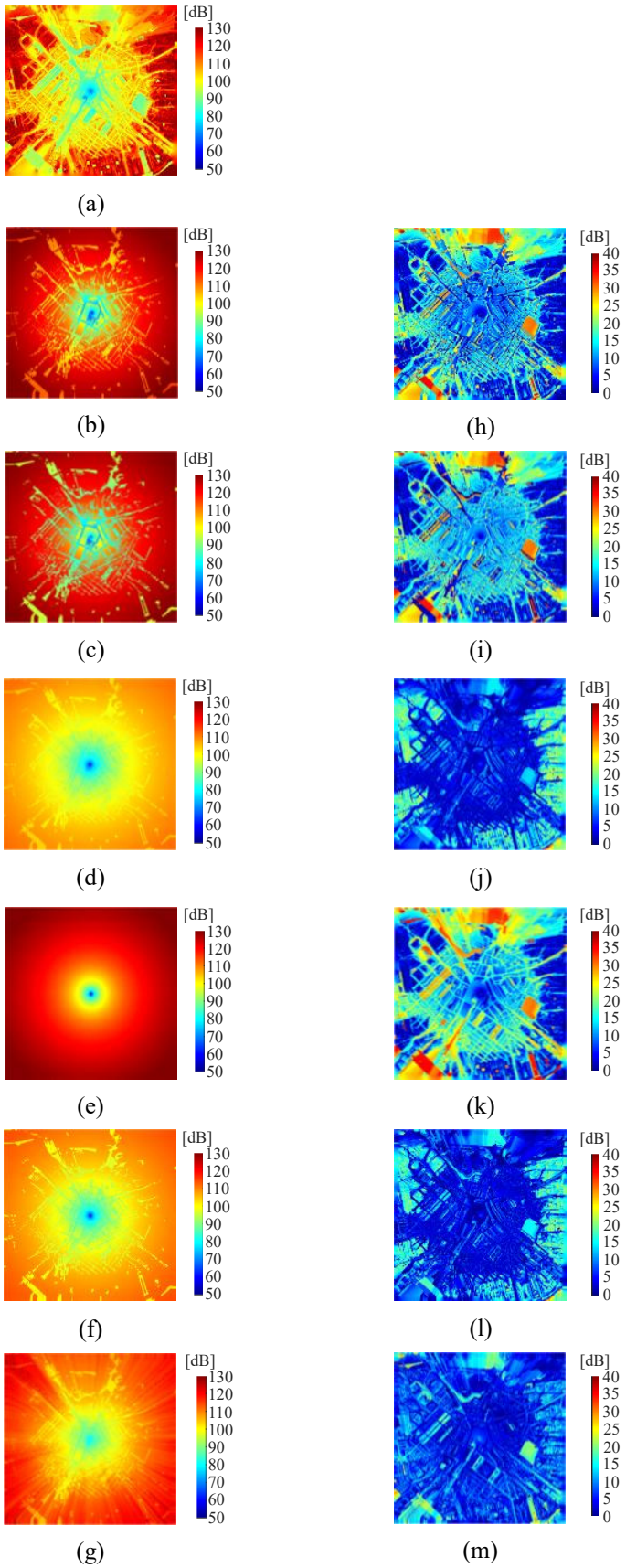

Fig. 4.7 Predictions under the UMi London 0.85 GHz, which include: Heatmaps for (a) Ranplan Professional simulation, (b) 3GPP [5, Table 7.4.1-1], (c) CI-5GCMSIG [9, Table 6], (d) CI-Calibrated, (e) ABG-5GCMSIG [9, Table 6], (f) ABG-Calibrated, and (g) AMPLE; and absolute error maps for (h) 3GPP, (i) CI-5GCMSIG, (j) CI-Calibrated, (k) ABG-5GCMSIG, (l) ABG-Calibrated, and (m) AMPLE.

For the error maps in the UMa scenario (as shown in Fig. 4.6(h)-(m)), prediction accuracy is largely influenced by the environment. Taking the 3GPP model as an example (Fig. 4.6(h)), prediction errors are acceptable in the LOS environment but abruptly increase as the environment gradually transitions to the NLOS case. Even with different parameters for the NLOS environment [5, Table 7.4.1-1], the 3GPP model still has a mean error of around 12 dB. This is similar to the CI-5GCMSIG model (Fig. 4.6(i)) and the ABG-5GCMSIG model (Fig. 4.6(k)), both of which perform slightly better than the 3GPP model in the NLOS environment. We previously consider that this may be caused by the differences in model construction datasets, so we use Ranplan simulation data to calibrate both the CI model and the ABG model (details are provided in Section 4.4.2). However, as shown in Fig. 4.6(j) (the CI-Calibrated model) and Fig. 4.6(l) (the ABG-Calibrated model), the results indicate that calibration improves predictions only in the LOS cases, while a gap remains in the NLOS case. Most errors are similar to those in the CI-5GCMSIG model and the ABG-5GCMSIG model, with a mean error of approximately 9 dB. Following that, by considering environmental factors, the AMPLE model (Fig. 4.6(m)) mitigates prediction errors in the NLOS case, with a mean error of around 8 dB.

For the error maps in the UMi scenario (as shown in Fig. 4.7(h)-(m)), prediction accuracy is influenced by both the environment and the dataset. The same environmental impact is observed in this scenario, where the 3GPP model (Fig. 4.7(h)), the CI-5GCMSIG model (Fig. 4.7(i)), and the ABG-5GCMSIG model (Fig. 4.7(k)) show significant prediction errors under the NLOS environment, with a mean error of approximately 12 dB. After calibration, the CI-Calibrated model (Fig. 4.7(j)) and the ABG-Calibrated model (Fig. 4.7(l)) show lower errors in the LOS environment but still have considerable errors in the NLOS environment, with a mean error of around 8 dB. Eventually, the environmental influences on predictions, especially in the NLOS environment, are effectively mitigated by the AMPLE model (Fig. 4.7(m)), with a mean error of around 7 dB.

Table 4.5 Parameters (in dB) of the AMPLE Model for UMa and UMi From 0.85 to 5 GHz

Model Parameter	**UMa**		**UMi**	
	LOS	**NLOS**	**LOS**	**NLOS**
Intercept A	59.86	59.79	55.19	55.20
In-Building n_1	1.35	1.80	1.59	1.78
Open Space n_2	1.14	1.64	1.46	1.89
Foliage n_3	2.59	2.71	2.70	2.70
Bodies of Water n_4	1.79	1.93	1.80	1.80
Frequency Coefficient γ	0.92	1.94	1.97	1.98
Shadow Fading std. σ	5.40	9.53	8.01	8.00
Default Values	Frequency from 0.85-5 GHz, $h_{\mathrm{BS}} = 30$ m, $h_{\mathrm{UT}} = 1.5$ m		Frequency from 0.85-5 GHz, $h_{\mathrm{BS}} = 15$ m, $h_{\mathrm{UT}} = 1.5$ m	

4.4.5 The AMPLE model From 0.85 to 5 GHz

Table 4.5 lists the parameters of the AMPLE model for the UMa and UMi scenarios. With different antenna heights (i.e., UMa $h_{\mathrm{BS}} = 30$ m, and UMi $h_{\mathrm{BS}} = 15$ m), the intercept A in the UMa scenario is slightly larger than in the UMi scenario. Beyond that, since most environments consist of buildings and open space, the PLE values of these two region types (i.e., n_1 and n_2) largely influence the performance of the AMPLE model, resulting in distinct differences across environments/scenarios. In contrast, the PLEs of foliage and water (i.e., n_3 and n_4) remain similar across four cases. In the meantime, the frequency coefficient reflects the impact of frequency on path loss, where only the UMa LOS environment shows a weaker frequency dependence. This may arise from the simplicity of the environment [47] and the limited range of frequency bands, which prevents the full impact of frequency dependence from being observed. If more complex environments, more carrier frequencies, or both are contained in the datasets, the frequency dependence would increase.

Besides, two points require further clarification: (1) why the AMPLE model in the LOS environments still cover those environmental factors instead of modelling open space

only, despite the typical definition of LOS; and (2) why the open space regions in the LOS environments of both scenarios have relatively lower PLE values. Regarding the first point, we classify data points based on both the map layout and a path loss threshold. That is, the LOS category includes not only direct LOS links but also those with first-order reflections, which can still result in low path loss values [125]. Furthermore, according to the straight-line mechanism described in Section 3.2.1, all regions intersected by the straight line are considered to contribute partially to the total path loss of the link. Therefore, even in the LOS environments, the influence of environmental factors remains present in both scenarios.

Moreover, the low PLE value for open space within the LOS environment is also attributed to the model's mechanism. Since the Txs are placed on buildings and the environmental information is based on 2D maps, links without obstructions are consistently misrecognised as penetrating through at least one building (i.e., the one located beneath the Tx) before reaching the Rxs. In other words, the impact of open space tends to be underestimated because the model mistakenly attributes it to buildings—particularly in the short-range LOS cases. Under these conditions, most of the open space influence is incorporated into the characterisation of buildings, causing the PLE n_2 to remain low at 1.14 for the UMa LOS and 1.46 for the UMi LOS. Instead, due to the more complex region intersections in the NLOS environments, this type of misclassification has less impact, as reflected in the more realistic parameter values observed in the NLOS cases for both scenarios [5, 9]. While this misrecognition affects the PLE values in the LOS environments, it still results in good path loss prediction performance (as described in Section 4.4.4). Therefore, we consider addressing this issue as part of future work to further enhance the AMPLE model, particularly in the LOS environments.

4.5 Summary

In this chapter, we have characterised the AMPLE model under UMa and UMi scenarios from 0.85-5 GHz. By using Ranplan Professional, we simulated four cites to characterise and validate the AMPLE model. The ray-based simulations at 2.1 GHz are validated with

measurements by extracting the CI model parameters and compared with those extracted from measurements in [47, Table I]. We also compared the AMPLE model with the 3GPP model, the ABG model, the CI model, and the models with simulation calibrations. The results showed that the AMPLE model outperforms these models by considering environments.

Chapter 5

An Empirical Site-Specific Channel Large-Scale Parameter Model with Ray-Based Validation

5.1 Introduction

[1][2]Apart from capturing complete propagation mechanisms (e.g., reflection, diffraction, scattering, and penetration) like ray-based models, the AMPLE model focuses on the root causes of these mechanisms–the environments that produce these mechanisms [16]. This is crucial for channel modelling since environments have the nature of "mechanism preferences" (e.g., walls mainly cause penetration, and corridors lead to waveguide effects). On the other hand, for LSPs other than path loss, those environmental factors are also important towards them, because all these values are related to signal power (i.e., the Ricean K-factor [43, 44], DS [45], and AS [46] are all influenced by the power of multipath components).

Given the importance of environmental factors and the relationships between LSPs and signal power, along with the statistical nature of these LSPs (i.e., distance-based log-normal

[1]The content of this chapter is based on the revised version of our publication [19].

distributions as demonstrated by previous research [41–46]), we connect the environments with large-scale parameter exponent (LSPE) matrix to numerically reveal the impacts of multiple regions on a single link. In this chapter, we propose a simple LSP model considering environmental factors, named as the AMPLE-LSP model. For LSP predictions, the AMPLE-LSP model covers parameters including path loss, the Ricean K-factor, DS and AS. This is achieved based on the straight line of each link that records the intersected regions and the corresponding lengths, of which the straight line is irrelevant to physical propagation mechanisms. Once the parameters are regressed, the AMPLE-LSP model achieves a site-specific LSP channel modelling, which enhances its accuracy compared to the models without physical-surrounding information.

The rest of this chapter is organised as follows. In Section 5.2, we provide the theoretical basis of the AMPLE-LSP model, that is, the distance-based log-normal modelling methods of LSPs. In Section 5.3, we introduce the AMPLE-LSP model, which is an extension to other LSPs based on the AMPLE model. In Section 5.4, we use Ranplan Professional to simulate both outdoor UMa and indoor InH scenarios for parameter extraction and model validation. Then, we present the application process of the AMPLE-LSP model, including the parameter extraction procedure. In Section 5.5, we validate the model performance and compare it with the LSP prediction in the 3GPP model and the 5GCMSIG model. Finally, Section 5.6 summarises this chapter.

5.2 Theoretical Basis

In this section, we provide a brief background on path loss, the Ricean K-factor, DS, and AS, focusing on the distance-based log-normal distributions, which are rarely known–particularly for the latter three [4–13]–but have been proposed and validated through previous measurement-based research [41–46].

5.2.1 Path Loss

Path loss is commonly defined as the difference (in dB) between the effective transmitted power and the received power [41], and here we consider path loss without antenna gains. Because of the log-normal nature over distance, beyond a CI distance d_0 (usually considered as 1 m), the path loss can be characterised as a function of distance d plus a shadow fading term $\Psi_\sigma^{\mathrm{PL}}$, which can be expressed as [42]

$$\mathrm{PL}\,[\mathrm{dB}] = A^{\mathrm{PL}} + 10n^{\mathrm{PL}}\log_{10}(d/d_0) + \Psi_\sigma^{\mathrm{PL}}, \qquad d \geq d_0, \tag{5.1}$$

where A^{PL} is the intercept representing the regressed decibel path loss at CI distance d_0, n^{PL} is the PLE, and the shadow fading term $\Psi_\sigma^{\mathrm{PL}}$ is normally distributed in decibels, with zero mean and a standard deviation σ^{PL}.

5.2.2 The Ricean K-Factor

The Ricean K-factor is determined as the power ratio between the strongest path and the sum of other multipath components [125]. In [43], by revealing the log-normal property of the Ricean K-factor from measurements, the authors proposed a distance-based Ricean K-factor model. This model has a form similar to the log-distance path loss model, and it can be expressed in decibels as [43, Eq. (15), (16)]

$$K\,[\mathrm{dB}] = A^{\mathrm{K}} + 10n^{\mathrm{K}}\log_{10} d + \Psi_\sigma^{\mathrm{K}} \tag{5.2}$$

with

$$A^{\mathrm{K}} = F + K_o, \tag{5.3}$$

where A^{K} is the intercept of K (it is set as the 1-km intercept for suburban macrocell environment in [43]), F is a combination of environment factors including season, antenna height, and beamwidth, K_o is a constant around 10.0 dB, n^{K} is the exponent, d is the distance, and Ψ_σ^{K} is a normal variate in dB-scale having zero mean and a standard deviation σ^{K}. A

similar distance-based model structure is also used in [44, Eq. (28)] to statistically predict the Ricean K-factor, of which it covers both LOS and NLOS cases.

5.2.3 RMS Delay Spread

Based on the delays of multipath components, the DS can be computed as [41, 45, 125]

$$\mathrm{DS} = \sqrt{\frac{\sum_{v=1}^{V} P_v \tau_v^2}{\sum_{v=1}^{V} P_v} - \left(\frac{\sum_{v=1}^{V} P_v \tau_v}{\sum_{v=1}^{V} P_v}\right)^2}, \tag{5.4}$$

where τ_v and P_v are the excess delay and the power of the vth multipath, respectively.

Following that, in [45], the authors introduced the log-normal distribution property of DS in relation to distance d, and provided a detailed argument and validation for this statistical property. At the end, the authors proposed a statistical model for DS, which can be written in decibels as [45, Eq. (10)]

$$\mathrm{DS}\,[\mathrm{dB}] = A^{\mathrm{DS}} + 10 n^{\mathrm{DS}} \log_{10} d + \Psi_{\sigma}^{\mathrm{DS}}, \tag{5.5}$$

where A^{DS} is the intercept of DS (the median value of DS at $d = 1$ km), n^{DS} is the exponent, and $\Psi_{\sigma}^{\mathrm{DS}}$ is a normal variate in dB-scale with zero mean and a standard deviation σ^{DS}.

5.2.4 Angular Spread

According to the 3GPP standards, the azimuth angular spread of arrival (ASA) and zenith angular spread of arrival (ZSA) can be obtained as [6, 125]

$$\mathrm{AS} = \sqrt{\frac{\sum_{v=1}^{V} (\theta_{v,\mu})^2 P_v}{\sum_{v=1}^{V} P_v}}, \tag{5.6}$$

where $\theta_{v,\mu}$ is given by

$$\theta_{v,\mu} = \mathrm{mod}(\theta_v - \mu_\theta + \pi, 2\pi) - \pi, \tag{5.7}$$

where θ_v is the azimuth angle of arrival (AOA)/zenith angle of arrival (ZOA) of the vth multipath, and μ_θ is defined as

$$\mu_\theta = \frac{\sum_{v=1}^{V} \theta_v P_v}{\sum_{v=1}^{V} P_v}. \tag{5.8}$$

In [46], after comparing multiple distribution functions at different distances of AS measurements via AIC method, the authors finally proved the distance-based log-normal distribution of AS. The statistical model of AS can be written as [46, Eq. (6), (7)]

$$\mathrm{AS}\,[\mathrm{dB}] = A^{\mathrm{AS}} + B \cdot d + \Psi_\sigma^{\mathrm{AS}}, \tag{5.9}$$

where A^{AS} and B are defined in [46] as the environment coefficients determined by linear regression, d is the distance, and $\Psi_\sigma^{\mathrm{AS}}$ is a normal variate in dB scale with zero mean and a standard deviation σ^{AS}. It should be noted that similar to the case of the Ricean K-factor (characterised by log-distance in [43, Eq. (15), (16)] and distance in [44, Eq. (28)]), modelling AS by distance in [46, Eq. (6), (7)] does not mean that AS cannot be modelled by log-distance.

5.3 The AMPLE-LSP Model

On the one hand, log-normal distributions of LSPs, including path loss [41, 42], the Ricean K-factor [43, 44], DS [45], and AS [46], provide a means of modelling those channel parameters as functions of distance in decibels. On the other hand, the AMPLE model offers a semi-empirical method for predicting path loss while considering environmental factors. Drawing on the similarities among these LSPs, we combine these approaches into an AMPLE-like method, that is, we construct the AMPLE model for LSPs (AMPLE-LSP) based on their distance-based log-normal distributions while considering environmental factors.

In this section, the process of constructing the AMPLE-LSP model is discussed in detail. A general modelling process is shown in Fig. 5.1, including LSP data analysis, map information extraction, model construction based on the straight line, and characterisations and predictions.

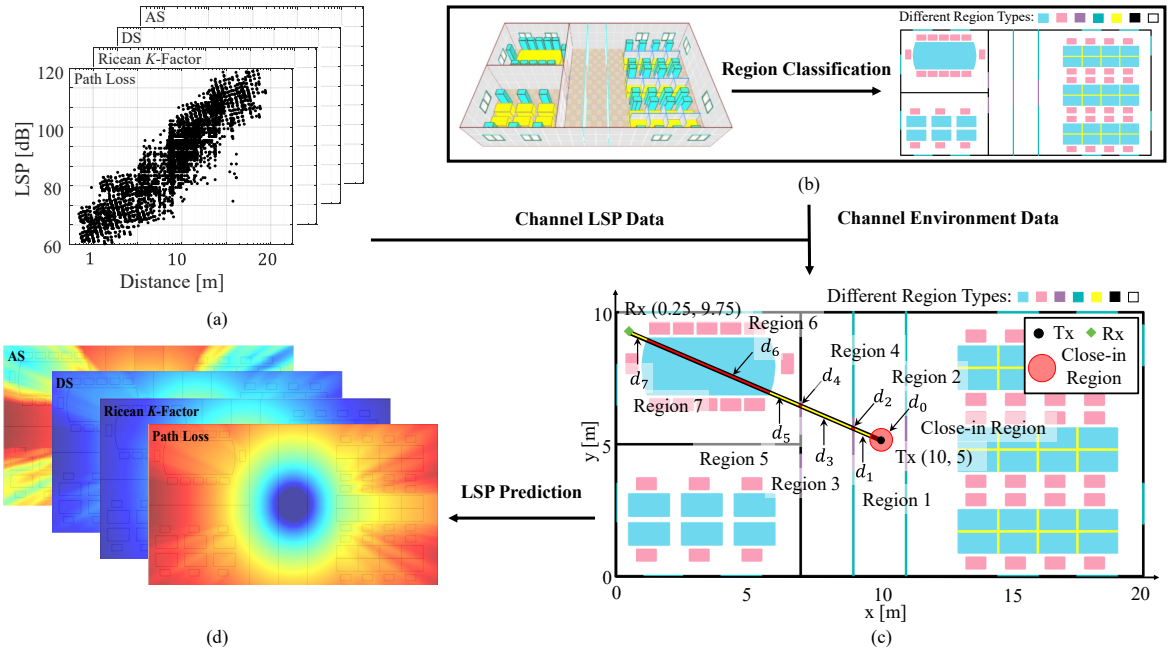

Fig. 5.1 Process of constructing the AMPLE-LSP model. (a) Channel LSP data from ray-based simulations and/or measurements. (b) Channel environment data with region classification. (c) Straight line with region lengths between Tx and Rx. (d) Predictions of LSPs.

5.3.1 Preliminary Information

Similar to the construction process of the AMPLE model (illustrated in Section 3.2), both LSP and environment information are required prior to construct the AMPLE-LSP model. For LSP data (as shown in Fig. 5.1(a)), they can be obtained from either ray-based simulations or measurements, and should include both the LSP values and the corresponding spatial coordinates. In addition, for channel environment data, it can be collected either from colour-coded raster maps for outdoor scenarios [16] or room layouts for indoor scenarios. To identify different environmental factors, the 2D raster map of the environment is classified into region types (e.g., walls as a region type) based on RGB values of map colours. For outdoor cases, machine learning methods such as k-means clustering [16, 17] are used for pre-processed maps (e.g., Google Maps), while deep learning methods like convolutional neural networks can be employed for raw maps with arbitrary region shapes (e.g., satellite maps). In indoor scenarios, region maps can be alternatively created using digital drawing software such as AutoCAD. Then, the LSP data collected from simulation and/or measurement can be

mapped onto region maps using coordinate systems, either employing the latitude/longitude for outdoor cases or room dimensions for indoor cases.

5.3.2 Model Construction

To parametrise the environment and construct the model, each region type is initially assigned a LSPE matrix that contains different LSPEs corresponding to various LSPs. These LSPE matrices are extracted based on different LSPs using simulations and/or measurements. Then, a straight line for each T-R link is established to record the intersected region, along with the region lengths, as illustrated in Fig. 5.1(c). Similar to (3.1), the straight line $\mathbf{S}^{\mathrm{LSP}}$ can be expressed as

$$\mathbf{S}^{\mathrm{LSP}} = \begin{bmatrix} \mathbf{N}_0 & \mathbf{N}_1 & \mathbf{N}_2 & \cdots & \mathbf{N}_R \\ d_0 & d_1 & d_2 & \cdots & d_R \end{bmatrix} \tag{5.10}$$

with

$$\mathbf{N}_R = \begin{bmatrix} n_R^{\mathrm{PL}} & n_R^{\mathrm{K}} & n_R^{\mathrm{DS}} & n_R^{\mathrm{AS}} \end{bmatrix}^{\mathrm{T}}, \tag{5.11}$$

where $\mathbf{N}_R$ is the Rth region LSPE matrix, $[\cdot]^{\mathrm{T}}$ is the transpose of a matrix, and d_R is the corresponding region length.

Considering the nature of CI distance in path loss [41] and the similar CI-distance-intercept relationship shown in other LSPs (as discussed in Section 5.2), we set d_0 as the CI distance for all LSPs along the straight line (where $d_0 = 1$ m), and the regions within the length d_0 are simplified as CI region. In other words, elements in $\mathbf{N}_0$ are 0, and the values of LSPs at d_0 are regressed as intercepts through simulations and/or measurements. In Fig. 5.1(c), the straight line intersects the CI region and seven other regions (i.e., $R = 7$), along with region lengths from d_0 to d_7.

For the AMPLE-LSP model, the formulation of the LSPs in decibels for each T-R straight line can be expressed as

$$\mathbf{LSP}\,[\mathrm{dB}] = \mathbf{A} + \sum_{r=1}^{R} 10\mathbf{N}_r \log_{10}\left(\frac{\sum_{k=0}^{r} d_k}{\sum_{k=0}^{r-1} d_k}\right) + \mathbf{\Psi}_{\sigma}, \tag{5.12}$$

where **LSP**, **A**, R, $\mathbf{N}_r$, d_k, and $\mathbf{\Psi}_\sigma$ are characterised as follows.

- ***Large-scale Parameter*** (**LSP**):

$$\mathbf{LSP}\,[\mathrm{dB}] = \begin{bmatrix} \mathrm{PL} & K & \mathrm{DS} & \mathrm{AS} \end{bmatrix}^{\mathrm{T}}. \tag{5.13}$$

  In the AMPLE-LSP model, the LSPs, including path loss (PL), the Ricean K-factor (K), RMS delay spread (DS) and angular spreads (AS), can be calculated using equation (5.12). Note that the parameter pairs vary across different LSPs and are extracted from simulations and/or measurements.

- ***Intercept*** (**A**):

$$\mathbf{A} = \begin{bmatrix} A^{\mathrm{PL}} & A^{\mathrm{K}} & A^{\mathrm{DS}} & A^{\mathrm{AS}} \end{bmatrix}^{\mathrm{T}}. \tag{5.14}$$

  The intercept matrix **A** contains the LSP values in dB scale at CI distance d_0 ($d_0 = 1$ m), which is extracted along with LSPE matrices.

- ***Intersected Regions*** (R, $\mathbf{N}_r$): Since the regions within d_0 are not counted in (5.10) (i.e., $n_0 = 0$), R regions are intersected by the T-R straight line, and the LSP matrix $\mathbf{N}_r$ contains the corresponding LSPEs for the rth region, which is

$$\mathbf{N}_r = \begin{bmatrix} n_r^{\mathrm{PL}} & n_r^{\mathrm{K}} & n_r^{\mathrm{DS}} & n_r^{\mathrm{AS}} \end{bmatrix}^{\mathrm{T}}. \tag{5.15}$$

- ***Weighted LSP*** (d_k): The weighted LSP of the rth region is computed by the subtraction between the end point LSP of rth and $r-1$th region, respectively [15–18]. Note that d_k is the kth region length.

- ***Normal Variate*** ($\mathbf{\Psi}_\sigma$):

$$\mathbf{\Psi}_\sigma = \begin{bmatrix} \Psi_\sigma^{\mathrm{PL}} & \Psi_\sigma^{\mathrm{K}} & \Psi_\sigma^{\mathrm{DS}} & \Psi_\sigma^{\mathrm{AS}} \end{bmatrix}^{\mathrm{T}}. \tag{5.16}$$

  In dB scale, $\mathbf{\Psi}_\sigma$ contains the normal variates for LSPs, each with a zero mean and a standard deviation σ [41–46].

Since the intersected regions R might not match the region types (e.g., one region type may be intersected multiple times), the terms with the same LSPE matrix (i.e., same region type) in equation (5.12) can be combined, which can be expressed as

$$\mathbf{LSP}\,[\mathrm{dB}] = \mathbf{A} + \sum_{m=1}^{M} D_m \mathbf{N}_m + \mathbf{\Psi}_\sigma \tag{5.17}$$

with

$$\mathbf{N}_m = \begin{bmatrix} n_m^{\mathrm{PL}} & n_m^{\mathrm{K}} & n_m^{\mathrm{DS}} & n_m^{\mathrm{AS}} \end{bmatrix}^{\mathrm{T}}, \tag{5.18}$$

where M is the number of classified region types, $\mathbf{N}_m$ is the LSPE matrix that contains the mth region type LSPEs, and D_m is the corresponding coefficient which is extracted by combining terms of $\mathbf{N}_m$.

For the number of Z data points (i.e., Z links) within the simulations and/or measurements, there are Z equations that have the similar format of (5.17). That is, those undefined parameter matrices, including intercept $\mathbf{A}$, LSPE matrix $\mathbf{N}_m$ for each region type, and the standard deviations of the normal variates $\mathbf{\Psi}_\sigma$, can be extracted by those Z paths and equations. Note that even the formations of equations are the same, different LSPEs within $\mathbf{N}_m$ are independent (e.g., n_m^{PL} and n_m^{AS} are extracted based on the simulated and/or measured path loss and AS, respectively). Finally, the predictions can be made via extracted model parameters, as illustrated in Fig. 5.1(d).

5.4 Model Applications

In this section, we apply the AMPLE-LSP model in complex outdoor scenarios and simple indoor scenarios simulated by Ranplan Professional [108–111]. We first introduce the Ranplan Professional channel multipath simulation with an example. Then, we present the applied outdoor and indoor scenarios for parameter extraction and model validation with details. After that, we introduce the parameter extraction process to construct the AMPLE-LSP model.

5.4.1 Ranplan Professional Channel Multipath Simulation

Recently, powerful ray-tracing simulators have been treated as "ray-tracing measurements [126]" to validate vital 5G technologies [124], as they can cover a wider range of channel information compared to the hardware measurements, while with only minor discrepancies [121–126]. Moreover, researchers have expanded the current standard 3GPP channel model using ray-based simulations [9, 10, 125]. In other words, with the current state-of-the-art, newly designed channel models can be characterised and validated not only by hardware measurements, but also the ray-based simulations. Therefore, in this chapter, we use Ranplan Professional, a powerful commercial ray-tracing simulator, to characterise and verify the proposed AMPLE-LSP model. Validated by hardware measurements [110, 111], Ranplan Professional has been used to characterise and validate channel models, including the AMPLE model [17, 18] and the DeepRay propagation model [112], as well as to validate other research in wireless communications [113, 114, 127, 128].

In Fig. 5.2, an example of Ranplan Professional multipath simulation is illustrated. Initially, the simulated environment is covered by multiple Rxs with a 0.5-metre interval, along with one Tx setting up at the centre of the environment, as illustrated in Fig. 5.2(a). Each T-R link contains separate multipath channel information including the number of multipath components, T-R separation distance, path gain, travel delay, AOA/ZOA, and the propagation process of each path. An example is shown in Fig. 5.2(b), where the Tx and Rx are positioned at (10, 5) and (0.25, 9.75), respectively, along with the first seven multipath information. It should be noted that the path propagation process records the full route of each path from the Tx to the Rx. For instance, in Fig. 5.2(b), ray no. 2 arrives at the Rx after one direct propagation (D), two transmissions (T), and one reflection (R). Thus, the propagation process of ray no. 2 is represented as "D-T-T-R". A simple explanation of simulated ray types is shown in Fig. 5.3, while a comprehensive illustration of ray types within a ray-tracing simulator can be found in Section 2.1.1 and [29, Section III]. In the Ranplan multipath simulations, 5 transmissions, 5 reflections, and 2 diffractions are considered the maximum mechanisms per path, whereas scattering is not covered. The propagation mechanism configurations in Ranplan Professional have been verified through

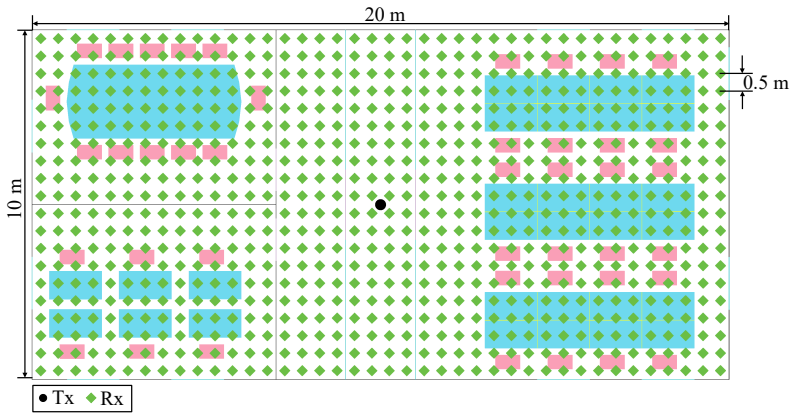

(a)

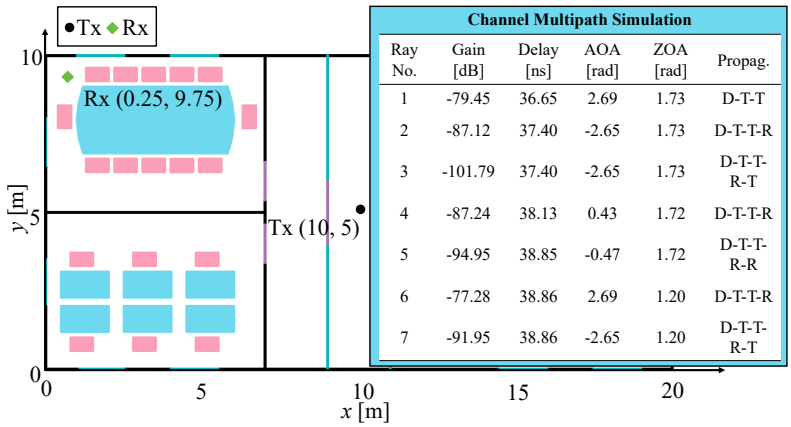

Channel Multipath Simulation

Ray No.	Gain [dB]	Delay [ns]	AOA [rad]	ZOA [rad]	Propag.
1	-79.45	36.65	2.69	1.73	D-T-T
2	-87.12	37.40	-2.65	1.73	D-T-T-R
3	-101.79	37.40	-2.65	1.73	D-T-T-R-T
4	-87.24	38.13	0.43	1.72	D-T-T-R
5	-94.95	38.85	-0.47	1.72	D-T-T-R-R
6	-77.28	38.86	2.69	1.20	D-T-T-R
7	-91.95	38.86	-2.65	1.20	D-T-T-R-T

(b)

Fig. 5.2 Example of Ranplan Professional channel multipath simulation. (a) Simulation with Rxs across the whole environment with a 0.5-metre interval. (b) Multipath simulation results of one link (i.e., between Tx (10, 5) to Rx (0.25, 9.75)). Propag. stands for propagation process of rays (e.g., for ray no. 2, "D-T-T-R" means the signal of this ray arrives at the Rx after one direct propagation (D), two transmissions (T), and one reflection (R)).

hardware measurements and are reported in [110, 111]. If one link contains a path with only direct propagation, we consider it a LOS link, and we use this criterion to distinguish LOS and NLOS cases within the simulation.

5.4.2 Simulated Scenarios

We construct complex outdoor scenarios and simple indoor scenarios to comprehensively characterise and validate the AMPLE-LSP model, where each scenario type contains two

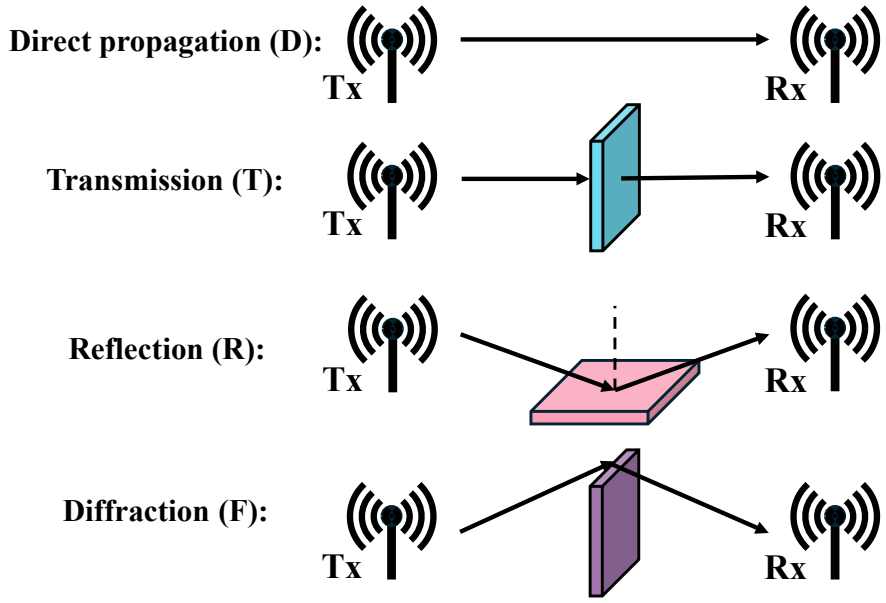

Fig. 5.3 Simple explanation of propagation mechanisms considered in the Ranplan Professional multipath simulation, where scattering is not covered [108]. Detailed information of ray types in ray-tracing can be found in Section 2.1.1 and [29, Section III].

simulations for parameter extraction and model validation [17]. Detailed scenario information is provided as follows.

Outdoor UMa Scenarios

Two UK cities, Sheffield (Outdoor Scenario A) and Barnsley (Outdoor Scenario B), are simulated to construct the outdoor UMa scenarios that fulfill the 3GPP UMa descriptions [17]. Environmental information, such as the city layouts and region elements, is imported from EDINA's Digimap Ordnance Survey [116], and the key region types after classification include *buildings*, *open space*, *foliage*, and *bodies of water* (lake, river, etc.). As shown in Fig. 5.4(a) and Fig. 5.4(c), two region maps are extracted from Ranplan Professional via XML files. The Txs in both scenarios are positioned on the rooftop of buildings and are equipped with omnidirectional antennas transmitting at 5GNR 2.1 GHz (5GNR band n1, 10-MHz bandwidth). The Tx power is 26 dBm, and the antenna gains of both Txs are 0 dBi. Complete environmental information, such as region heights, simulation ranges, Tx position, and the electromagnetic property of materials, is reported in Section 4.3.2.

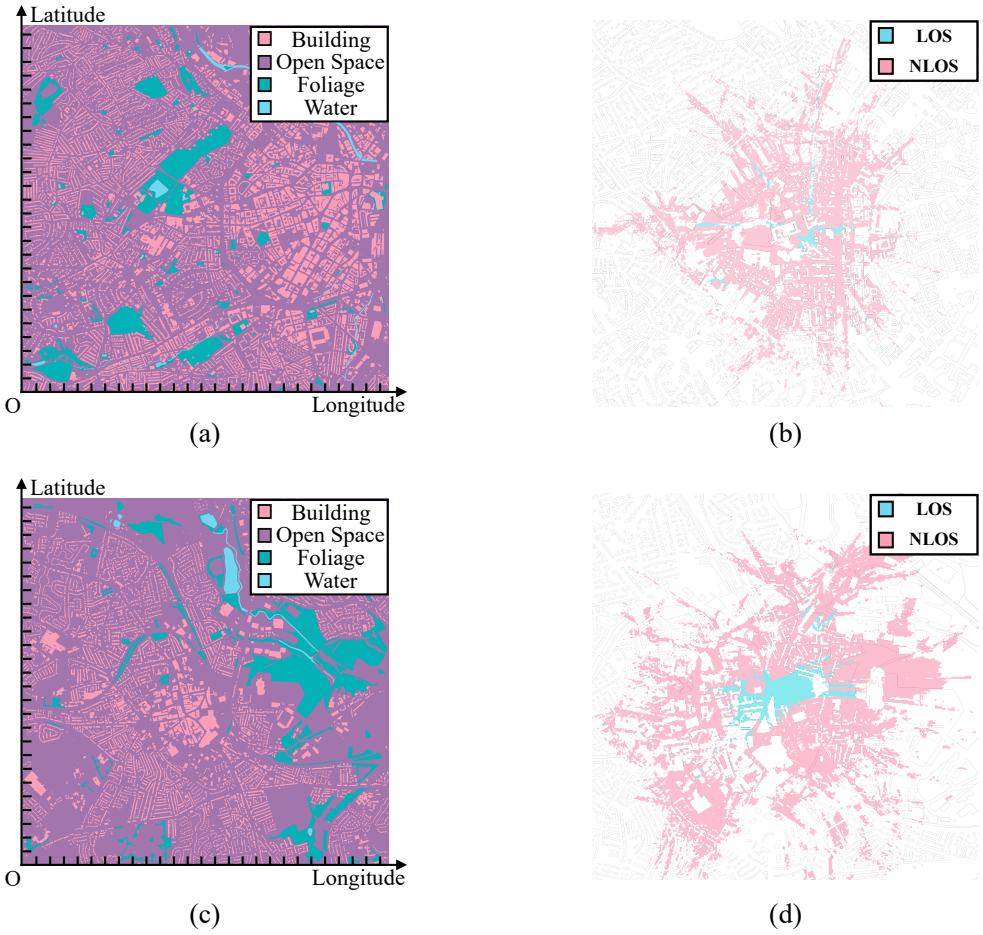

Fig. 5.4 Environmental information of the outdoor scenarios, including (a) the region map and (b) LOS/NLOS data of Outdoor Scenario A for parameter extraction, and (c) the region map and (d) LOS/NLOS data of Outdoor Scenario B for model validation.

Following the multipath simulation process illustrated in Fig. 5.2(a), both cities are mapped with Rxs with a resolution of 5 m. Due to the complexity of outdoor scenarios, not every positioned Rx receives a signal. Initially, we collect 224,627 links for Outdoor Scenario A and 160,400 links for Outdoor Scenario B, where the total multipath components are 1,813,795 and 2,862,957, respectively. Each data point includes the T-R separation distance, ray path gain, delay, AOA/ZOA, and the propagation process of each ray (as described in Section 5.4.1, with examples shown in Fig. 5.2(b) and Fig. 5.3). Following that, to eliminate small-scale fading effects, we assume that all the rays within a link contribute constructively to the total path loss and we compute the path loss by summing the path loss of rays in linear scale. Other LSPs, including the Ricean K-factor, DS ((5.4)), and

Table 5.1 Information of Outdoor Datasets for Model Extraction and Performance Validation. # of Data Points Refers to the Number of Data Points

	Outdoor Scenario A		**Outdoor Scenario B**	
Set Type	Extraction		Validation	
Frequency [GHz]	2.1		2.1	
Environment	LOS	NLOS	LOS	NLOS
# of Data Points	879	28,563	2,892	32,677
Distance (μ_d, σ_d) **[m]**	(281.8, 208.7)	(461.0, 207.4)	(200.7, 122.9)	(543.5, 216.9)
PL $(\mu^{\mathrm{PL}}, \sigma^{\mathrm{PL}})$ **[dB]**	(85.7, 6.5)	(104.5, 7.9)	(84.7, 4.6)	(104.6, 6.9)
$\boldsymbol{K}$ $(\mu^{\mathrm{K}}, \sigma^{\mathrm{K}})$ **[dB]**	(4.0, 3.3)	-	(6.8, 4.8)	-
DS $(\mu^{\mathrm{DS}}, \sigma^{\mathrm{DS}})$ **[ns]**	(149.2, 67.9)	(293.7, 223.6)	(253.5, 88.2)	(309.9, 212.9)
ASA $(\mu^{\mathrm{ASA}}, \sigma^{\mathrm{ASA}})$ **[°]**	(39.7, 19.3)	(65.3, 28.8)	(36.5, 17.1)	(58.3, 30.5)
ZSA $(\mu^{\mathrm{ZSA}}, \sigma^{\mathrm{ZSA}})$ **[°]**	(2.4, 1.7)	(5.8, 4.7)	(2.2, 1.4)	(5.0, 4.4)

ASA/ZSA ((5.6)-(5.8)), are computed according to the procedures and equations described in Section 5.2. In the meantime, based on the propagation process of rays within each link, we classify a link as LOS if it contains at least one multipath component with direct propagation only (as described in Section 5.4.1). Using this criterion, the entire scenario can be divided into LOS and NLOS environments. After filtering out erroneous simulations (e.g., data points outside the considered scenario, T-R distance greater than 1,500 m, etc.), we finally collect 29,442 links in Outdoor Scenario A for parameter extraction and 35,569 links in Outdoor Scenario B for model validation. The LOS/NLOS distributions of two outdoor simulations are illustrated in Fig. 5.4(b) and Fig. 5.4(d), respectively. In the meantime, the LSP information of two datasets with LOS/NLOS classification is described in Table 5.1.

Indoor InH Scenarios

As shown in Fig. 5.5(a) and Fig. 5.6(a), both indoor offices are based on the layout of 3GPP InH-office [5], with a basic size of 120 m $\times$ 50 m $\times$ 3 m. Following that, we add more details including doors and rooms within two indoor offices. By creating the region map using AutoCAD (as shown in Fig. 5.5(b) and Fig. 5.6(b)), the environmental factors are

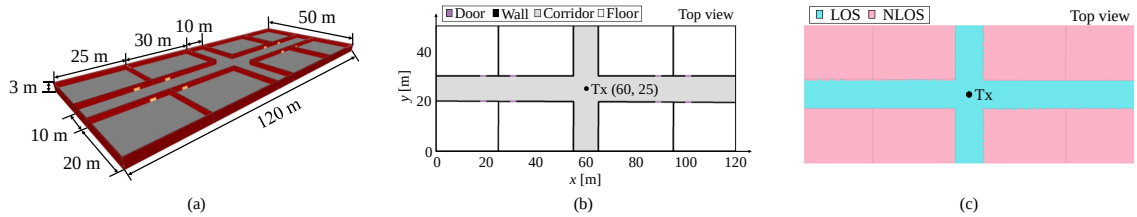

Fig. 5.5 Indoor Office C used for parameter extraction based on 3GPP InH-office layout [5]. (a) Layout and dimensions. (b) Region map. (c) LOS/NLOS classification based on multipath simulation.

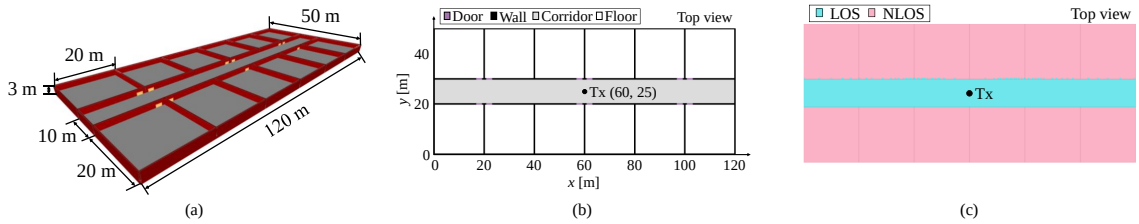

Fig. 5.6 Indoor Office D used for model validation based on 3GPP InH-office layout [5]. (a) Layout and dimensions. (b) Region map. (c) LOS/NLOS classification based on multipath simulation.

classified into four region types, which are: *door* is purple, *wall* is black, *corridor* is grey, and *floor* is white. Also, for the same region type in both scenarios, the materials are set as the same to facilitate better evaluation. The electromagnetic properties of materials used in both scenarios, including material type, transmission loss, reflection loss, and diffraction loss, are listed in Table 5.2. The indoor material database in Ranplan Professional is derived from measurements conducted by Ranplan Wireless as part of the European project "WiFEEB" [129].

Combining the room dimensions, a top-view coordinate system is established, where the Tx is positioned at the centre of the office (i.e., coordinates (60, 25)). For both indoor

Table 5.2 Electromagnetic Properties of Materials Used in Ranplan Professional at 2.4 GHz, Including Losses [dB] of Transmission, Reflection, and Diffraction [129]

Object	Door	Wall	Corridor	Floor
Material	Medium wood	Medium concrete	Heavy concrete	
Transmission [dB]	5.3	14.7	23.6	
Reflection [dB]	16.6	7.5	6	
Diffraction [dB]	27.7	24.7	21.1	

Table 5.3 Information of Indoor Datasets for Model Extraction and Performance Validation. # of Data Points Refers to the Number of Data Points

	Indoor Office C		**Indoor Office D**	
Set Type	Extraction		Validation	
Frequency [GHz]	2.4		2.4	
Environment	LOS	NLOS	LOS	NLOS
# of Data Points	6,478	17,510	4,849	19,139
Distance (μ_d, σ_d) **[m]**	(26.7, 16.2)	(37.1, 14.1)	(30.4, 16.9)	(35.3, 14.8)
PL $(\mu^{\mathbf{PL}}, \sigma^{\mathbf{PL}})$ **[dB]**	(69.6, 6.9)	(93.3, 10.7)	(67.6, 5.9)	(91.8, 11.4)
$\boldsymbol{K}$ $(\mu^{\mathbf{K}}, \sigma^{\mathbf{K}})$ **[dB]**	(1.8, 2.8)	-	(2.0, 2.2)	-
DS $(\mu^{\mathbf{DS}}, \sigma^{\mathbf{DS}})$ **[ns]**	(37.0, 17.4)	(33.8, 15.3)	(42.9, 15.7)	(32.5, 15.3)
ASA $(\mu^{\mathbf{ASA}}, \sigma^{\mathbf{ASA}})$ **[$\circ$]**	(40.7, 18.6)	(50.9, 15.0)	(44.0, 17.5)	(49.2, 16.3)
ZSA $(\mu^{\mathbf{ZSA}}, \sigma^{\mathbf{ZSA}})$ **[$\circ$]**	(7.2, 5.0)	(3.3, 2.7)	(6.5, 5.2)	(3.9, 3.2)

scenarios, the Txs are transmitting at WiFi 802.11n 2.4 GHz [108, 135], with a bandwidth of 20 MHz. To eliminate the system influence, we set the Tx power to 0 dBm, and the antenna gains of both Tx and Rx are 0 dBi. The heights of Tx and Rx are 3 m (i.e., ceiling in 3GPP [5]) and 1 m, respectively. Note that all the propagation conditions fulfill the modelling requirements of the 3GPP channel model [5].

Similar to the process illustrated in Fig. 5.2(a), both indoor cases are mapped with 24,000 Rxs with a resolution of 0.5 m, resulting in 24,000 links collected for each case. Since each link contains multipath components, a total of 777,251 data points are collected in Indoor Office C and 615,842 in Indoor Office D. The overall information and data extraction process in the indoor simulations are similar to those in the two outdoor scenarios. After filtering out erroneous simulations (e.g., removing data points outside the considered scenario, links shorter than 1 m, etc.), 23,988 links are retained for each case. The LOS/NLOS distributions of two indoor offices are illustrated in Fig. 5.5(c) and Fig. 5.6(c), respectively. In the meantime, the LSP information of two datasets with LOS/NLOS classification is generally described in Table 5.3.

5.4.3 Parameter Extraction

Following the distance-based log-normal distribution [41–46] described in Section 5.2 and the structure of the AMPLE-LSP model in (5.17), we generalise the parameter extraction process across five LSPs under a unified formulation for convenience. Let $\lambda \in \{1,2,...,5\}$ index the LSPs (e.g., $\lambda = 1$ represents path loss, $\lambda = 2$ represents the Ricean K-factor, and so on), so that (5.17) for $\text{LSP}^{(\lambda)}$ can be written as

$$\text{LSP}^{(\lambda)} = A^{(\lambda)} + \sum_{m=1}^{M} D_m n_m^{(\lambda)} + \Psi_{\sigma}^{(\lambda)}. \tag{5.19}$$

Since $\Psi_{\sigma}^{(\lambda)}$ is a normal variate with $N[0,(\sigma^{(\lambda)})^2]$, which means, the total $\text{LSP}^{(\lambda)}$ is normally distributed with $N[\mu^{(\lambda)},(\sigma^{(\lambda)})^2]$, where

$$\mu^{(\lambda)} = A^{(\lambda)} + \sum_{m=1}^{M} D_m n_m^{(\lambda)}. \tag{5.20}$$

Based on (5.20), the PDF of the zth link $\text{LSP}^{(\lambda)}$ can be expressed as

$$P(l_z^{(\lambda)};\mu^{(\lambda)},\sigma^{(\lambda)}) = \frac{1}{\sqrt{2\pi}\sigma^{(\lambda)}}\exp\left(-\frac{(l_z^{(\lambda)}-\mu^{(\lambda)})^2}{2(\sigma^{(\lambda)})^2}\right), \tag{5.21}$$

where $l_z^{(\lambda)}$ is the zth link $\text{LSP}^{(\lambda)}$ out of Z samples. Then, we use ML to extract the aforementioned parameters, including intercept $A^{(\lambda)}$, LSPEs $n_m^{(\lambda)}$ (for M region types, where $M = 4$ in both scenarios), and the standard deviation of $\Psi_{\sigma}^{(\lambda)}$. The likelihood function can be written as

$$F(\mu^{(\lambda)},\sigma^{(\lambda)}) = \prod_{z=1}^{Z} \frac{1}{\sqrt{2\pi}\sigma^{(\lambda)}}\exp\left(-\frac{(l_z^{(\lambda)}-\mu^{(\lambda)})^2}{2(\sigma^{(\lambda)})^2}\right). \tag{5.22}$$

By converting the likelihood function F into its negative natural logarithm form, the problem of finding the optimal parameters can be formulated as minimising this negative log-likelihood function, which can be expressed as [17]

$$\arg \min_{A^{(\lambda)},n_m^{(\lambda)},\sigma^{(\lambda)}} (-\ln F(\mu^{(\lambda)},\sigma^{(\lambda)})). \tag{5.23}$$

Subsequently, we use gradient descent to extract the undefined parameters, including intercept $A^{(\lambda)}$, LSPE $n_m^{(\lambda)}$, and standard deviation $\sigma^{(\lambda)}$. The partial derivatives of (5.22) for these parameters can be therefore characterised as

$$-\frac{\partial \ln F(\mu^{(\lambda)},\sigma^{(\lambda)})}{\partial A^{(\lambda)}} = \sum_{z=1}^{Z}\left(\frac{\mu^{(\lambda)}-l_z^{(\lambda)}}{(\sigma^{(\lambda)})^2}\right), \tag{5.24}$$

$$-\frac{\partial \ln F(\mu^{(\lambda)},\sigma^{(\lambda)})}{\partial n_m^{(\lambda)}} = \sum_{z=1}^{Z}\left(\frac{(\mu^{(\lambda)}-l_z^{(\lambda)})D_m}{(\sigma^{(\lambda)})^2}\right), \tag{5.25}$$

$$-\frac{\partial \ln F(\mu^{(\lambda)},\sigma^{(\lambda)})}{\partial \sigma^{(\lambda)}} = \sum_{z=1}^{Z}\left(\frac{1}{\sigma^{(\lambda)}}-\frac{(l_z^{(\lambda)}-\mu^{(\lambda)})^2}{(\sigma^{(\lambda)})^3}\right). \tag{5.26}$$

Based on (5.24)-(5.26), these parameters are jointly extracted by gradient descent with an appropriate step size. We choose the initial values of these parameters based on [5, Table 7.5-6], and we set the step size between 2×10^{-3} to 2×10^{-6}.

5.5 Results and Analysis

5.5.1 Compared Models

We compare the AMPLE-LSP model with the 3GPP-LSP model [5] and the 5GCMSIG-LSP model [9], which represent the current LSP prediction approaches within GSCMs for constructing statistical channel matrix. The 5GCMSIG-LSP model for the UMa and InH scenarios is summarised in Table 5.4 and Table 5.6, which is from [9, Table 6 & Table 13 & Table 23-36]; and the 3GPP-LSP model for the UMa and InH scenarios is summarised in Table 5.5 and Table 5.7, which is from [5, Table 7.4.1-1 & Table 7.5-6]. In these models, d is the T-R 3D separation distance in metre, f is the carrier frequency in GHz, and c is the speed of light in metre. It should be noted that DS, ASA, and ZSA are converted to linear scale from the original logarithmic values in both models before predicting the corresponding LSP values in Outdoor Scenario B and Indoor Office D.

Table 5.4 5GCMSIG Path Loss Model [9, Table 6] for the UMa Outdoor Scenario and the InH Indoor Scenario

Scenario	Environment	5GCMSIG Path Loss Model
UMa	**LOS**	$\mathrm{PL}_{\text{UMa-LOS}} = 20\log_{10}(\frac{4\pi f\times 10^9}{c}) + 20\log_{10}(d)$
	NLOS	$\mathrm{PL}_{\text{UMa-NLOS}} = 19.2 + 34\log_{10}(d) + 23\log_{10}(f)$
InH	**LOS**	$\mathrm{PL}_{\text{InH-LOS}} = 20\log_{10}(\frac{4\pi f\times 10^9}{c}) + 17.3\log_{10}(d)$
	NLOS	$\mathrm{PL}_{\text{InH-NLOS}} = 17.3 + 38.3\log_{10}(d) + 24.9\log_{10}(f)$

*d is the T-R 3D distance in m, f is the carrier frequency in GHz, and c is the speed of light in m.

Table 5.5 3GPP Path Loss Model [5, Table 7.4.1-1] for the UMa Outdoor Scenario and the InH Indoor Scenario

Scenario	Environment	3GPP Path Loss Model
UMa	**LOS**	$\mathrm{PL}_{\text{UMa-LOS}} = \begin{cases} \mathrm{PL}_1, & 10\,\text{m} \le d_{\text{2D}} \le d'_{\text{BP}} \\ \mathrm{PL}_2, & d'_{\text{BP}} \le d_{\text{2D}} \le 5\,\text{km}; \end{cases}$ $\mathrm{PL}_1 = 28 + 22\log_{10}(d) + 20\log_{10}(f);$ $\mathrm{PL}_2 = 28 + 40\log_{10}(d) + 20\log_{10}(f)$ $-9\log_{10}((d'_{\text{BP}})^2 + (h_{\text{Tx}} - h_{\text{Rx}})^2)$
	NLOS	$\mathrm{PL}_{\text{UMa-NLOS}} = \max(\mathrm{PL}_{\text{UMa-LOS}}, \mathrm{PL}'_{\text{UMa-NLOS}});$ $\mathrm{PL}'_{\text{UMa-NLOS}} = 13.54 + 39.08\log_{10}(d) + 20\log_{10}(f)$ $-0.6(h_{\text{Rx}} - 1.5)$
InH	**LOS**	$\mathrm{PL}_{\text{InH-LOS}} = 32.4 + 17.3\log_{10}(d) + 20\log_{10}(f)$
	NLOS	$\mathrm{PL}_{\text{InH-NLOS}} = \max(\mathrm{PL}_{\text{InH-LOS}}, \mathrm{PL}'_{\text{InH-NLOS}});$ $\mathrm{PL}'_{\text{InH-NLOS}} = 17.30 + 38.3\log_{10}(d) + 24.9\log_{10}(f)$

*d is the T-R 3D distance in m, f is the carrier frequency in GHz, and c is the speed of light in m.
*d_{2D} is the T-R 2D distance in m, h_{Tx} is the Tx height in m, h_{Rx} is the Rx height in m, and $d'_{\text{BP}} = \frac{4(h_{\text{Tx}}-1)(h_{\text{Rx}}-1)f\times 10^9}{c}$ in this chapter.

Table 5.6 Other Large-Scale Parameter Models of the 5GCMSIG Model [9, Table 13 & Table 23-36] for the UMa Outdoor Scenario and the InH Indoor Scenario

5GCMSIG-LSP		**LOS**	**NLOS**
UMa	$\boldsymbol{K}$ **[dB]**	9	N/A
	$\mathbf{log_{10}(DS/s)}$	-7.0278	-6.4429
	$\mathbf{log_{10}(ASA/1^\circ)}$	1.8096	1.8704
	$\mathbf{log_{10}(ZSA/1^\circ)}$	0.9504	1.2601
InH	$\boldsymbol{K}$ **[dB]**	$0.84\log_{10}(1+f)+2.12$	N/A
	$\mathbf{log_{10}(DS/s)}$	$-0.28\log_{10}(1+f)-7.31$	$-0.35\log_{10}(1+f)-7.06$
	$\mathbf{log_{10}(ASA/1^\circ)}$	$0.07\log_{10}(1+f)+1.39$	$-0.22\log_{10}(1+f)+1.98$
	$\mathbf{log_{10}(ZSA/1^\circ)}$	$-0.52\log_{10}(1+f)+1.60$	$-0.03\log_{10}(1+f)+0.89$

*f is the carrier frequency in GHz.

Table 5.7 Other Large-Scale Parameter Models of the 3GPP Channel Model [5, Table 7.5-6] for the UMa Outdoor Scenario and the InH Indoor Scenario

3GPP-LSP		**LOS**	**NLOS**
UMa	$\boldsymbol{K}$ **[dB]**	9	N/A
	$\mathbf{log_{10}(DS/s)}$	$-6.955-0.0963\log_{10}(f)$	$-6.28-0.204\log_{10}(f)$
	$\mathbf{log_{10}(ASA/1^\circ)}$	1.81	$2.08-0.27\log_{10}(f)$
	$\mathbf{log_{10}(ZSA/1^\circ)}$	0.95	$1.512-0.3236\log_{10}(f)$
InH	$\boldsymbol{K}$ **[dB]**	7	N/A
	$\mathbf{log_{10}(DS/s)}$	$-0.01\log_{10}(1+f)-7.692$	$-0.28\log_{10}(1+f)-7.173$
	$\mathbf{log_{10}(ASA/1^\circ)}$	$-0.19\log_{10}(1+f)+1.781$	$-0.11\log_{10}(1+f)+1.863$
	$\mathbf{log_{10}(ZSA/1^\circ)}$	$-0.26\log_{10}(1+f)+1.44$	$-0.15\log_{10}(1+f)+1.387$

*f is the carrier frequency in GHz.

5.5.2 Performance Metrics

For performance evaluation, we use RMSE in (4.29) and MAE in (4.30) to validate the point-wise performance of the models. Beyond that, we consider PMDE in (4.32) that we previously proposed in Section 4.4.3 to assess the overall alignment between prediction and measurement via statistical distributions [17]. Also, we use the mean simulation time per data point t_p in (4.33) to evaluate model complexity. All experiments in this chapter are conducted on a Dell G15 laptop (CPU: Intel (R) Core (TM) i7-12700H 2.30 GHz; RAM: 32.0 GB 4800 MHz) using the MATLAB R2023a programming environment.

5.5.3 Validation Results and Analysis

Following the parameter extraction process described in Section 5.4.3, we apply the AMPLE-LSP model in both complex outdoor scenarios and simple indoor scenarios, to validate its prediction abilities under both complex and simple environments. Specifically, we extract the AMPLE model from Outdoor Scenario A (Fig. 5.4(a) & (b)) and Indoor Office C (Fig. 5.5), and validate it in Outdoor Scenario B (Fig. 5.4(c) & (d)) and Indoor Office D (Fig. 5.6), respectively. More information of these environments can be found in Section 5.4.2. Compared with the 3GPP model and the 5GCMSIG model (as shown in Table 5.4-5.7), the performance results are presented in Table 5.8-5.12. Meanwhile, we plot the CDFs of the absolute error (i.e., $|\hat{l}_z - l_z|$) between the model LSP predictions and the Ranplan simulation results under Outdoor Scenario B and Indoor Office D. In addition, we generate the absolute error maps between the simulation results and the corresponding predictions from all three models to visually compare their performance. The CDFs of the LSP predictions are presented in Fig. 5.7-5.11, and the corresponding absolute error maps are shown in Fig. 5.12-5.16.

Table 5.8 Path Loss Prediction Performance of Models under Outdoor Scenario B at 5GNR 2.1 GHz and Indoor Office D at WiFi 802.11n 2.4 GHz

Scenario	Environment	Metrics	Path Loss [dB]		
			5GCMSIG	3GPP	AMPLE-LSP
Outdoor B	LOS	RMSE	1.75	2.35	1.08
		MAE	1.53	1.93	0.90
		PMDE	0.22	0.29	0.01
		t_p [ns]	19.52	24.67	6.93
	NLOS	RMSE	15.17	21.89	5.95
		MAE	13.84	20.67	4.66
		PMDE	1.38	1.47	0.46
		t_p [ns]	10.80	13.60	1.69
Indoor D	LOS	RMSE	3.62	3.66	0.36
		MAE	3.60	3.64	0.31
		PMDE	0.58	0.58	0.02
		t_p [ns]	15.77	16.98	4.66
	NLOS	RMSE	9.86	9.86	6.74
		MAE	8.19	8.19	5.60
		PMDE	0.66	0.66	0.48
		t_p [ns]	11.15	11.28	1.47

Table 5.9 The Ricean K-Factor Prediction Performance of Models under Outdoor Scenario B at 5GNR 2.1 GHz and Indoor Office D at WiFi 802.11n 2.4 GHz

Scenario	Environment	Metrics	Ricean K-Factor [dB]		
			5GCMSIG	3GPP	AMPLE-LSP
Outdoor B	LOS	RMSE	5.31		4.30
		MAE	4.51		3.53
		PMDE	1.49		1.05
		t_p [ns]	1.66		4.67
Indoor D	LOS	RMSE	2.31	5.47	1.18
		MAE	1.82	5.21	0.88
		PMDE	1.89	1.40	0.16
		t_p [ns]	1.24	1.23	3.25

Table 5.10 DS Prediction Performance of Models under Outdoor Scenario B at 5GNR 2.1 GHz and Indoor Office D at WiFi 802.11n 2.4 GHz

Scenario	Environment	Metrics	RMS Delay Spread [ns]		
			5GCMSIG	**3GPP**	**AMPLE-LSP**
Outdoor B	LOS	RMSE	182.46	174.23	107.29
		MAE	161.73	153.36	85.29
		PMDE	1.99	1.99	0.56
		t_p [ns]	3.32	3.58	4.08
	NLOS	RMSE	218.87	255.45	217.39
		MAE	177.73	217.69	170.56
		PMDE	1.99	1.99	1.43
		t_p [ns]	1.86	1.88	1.67
Indoor D	LOS	RMSE	17.67	27.72	4.98
		MAE	15.84	24.26	3.64
		PMDE	1.94	1.94	0.10
		t_p [ns]	3.62	3.73	3.28
	NLOS	RMSE	28.67	21.55	14.68
		MAE	25.20	18.36	11.24
		PMDE	2.00	1.99	0.64
		t_p [ns]	2.14	2.06	1.43

Table 5.11 ASA Prediction Performance of Models under Outdoor Scenario B at 5GNR 2.1 GHz and Indoor Office D at WiFi 802.11n 2.4 GHz

Scenario	Environment	Metrics	ASA [$\circ$]		
			5GCMSIG	**3GPP**	**AMPLE-LSP**
Outdoor B	LOS	RMSE	32.81	32.86	16.46
		MAE	29.56	29.61	13.10
		PMDE	2.00	2.00	1.17
		t_p [ns]	3.77	3.51	4.08
	NLOS	RMSE	34.37	50.35	30.99
		MAE	28.43	43.90	24.94
		PMDE	1.99	2.00	1.29
		t_p [ns]	1.88	1.87	1.68
Indoor D	LOS	RMSE	24.53	17.90	14.65
		MAE	20.25	15.31	12.80
		PMDE	1.97	1.97	0.10
		t_p [ns]	3.45	3.65	3.04
	NLOS	RMSE	28.78	21.83	15.52
		MAE	24.03	16.73	12.25
		PMDE	1.99	1.99	0.28
		t_p [ns]	2.08	1.97	1.40

Table 5.12 ZSA Prediction Performance of Models under Outdoor Scenario B at 5GNR 2.1 GHz and Indoor Office D at WiFi 802.11n 2.4 GHz

Scenario	Environment	Metrics	ZSA [○]		
			5GCMSIG	3GPP	AMPLE-LSP
Outdoor B	LOS	RMSE	6.83	6.82	1.59
		MAE	6.74	6.73	1.10
		PMDE	1.94	1.94	0.69
		t_p [ns]	4.08	3.47	4.08
	NLOS	RMSE	13.92	21.04	4.40
		MAE	13.35	20.61	3.23
		PMDE	1.94	1.94	1.12
		t_p [ns]	1.89	1.88	1.74
Indoor D	LOS	RMSE	15.47	14.50	1.58
		MAE	14.68	13.72	0.52
		PMDE	1.99	1.99	0.01
		t_p [ns]	3.57	3.57	2.89
	NLOS	RMSE	4.86	16.75	2.12
		MAE	4.36	16.44	1.56
		PMDE	1.99	1.49	1.03
		t_p [ns]	2.06	1.93	1.39

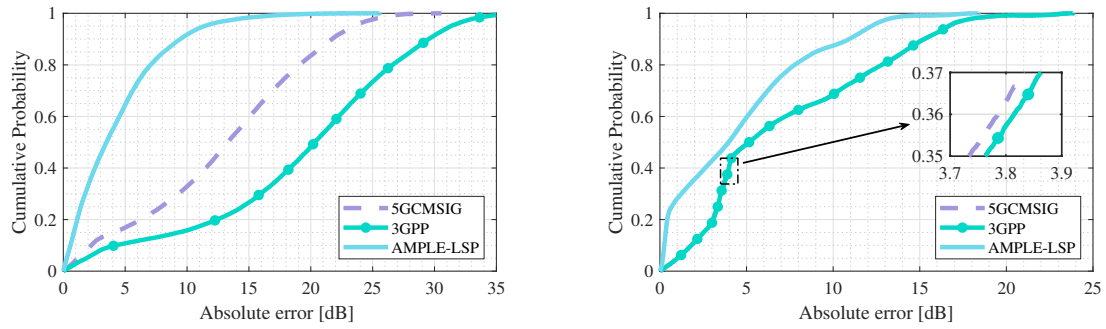

(a) (b)

Fig. 5.7 CDF of path loss absolute error between model predictions and Ranplan Professional simulations for (a) Outdoor Scenario B and (b) Indoor Office D.

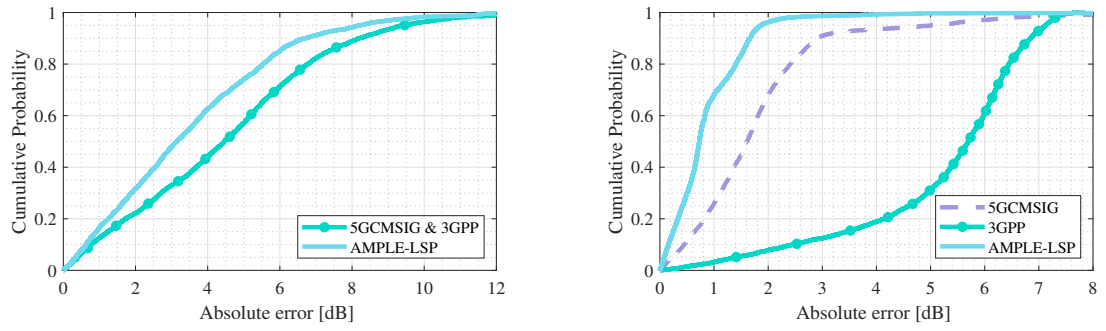

(a) (b)

Fig. 5.8 CDF of the Ricean K-factor absolute error between predictions and Ranplan Professional simulations for (a) Outdoor Scenario B LOS case and (b) Indoor Office D LOS case.

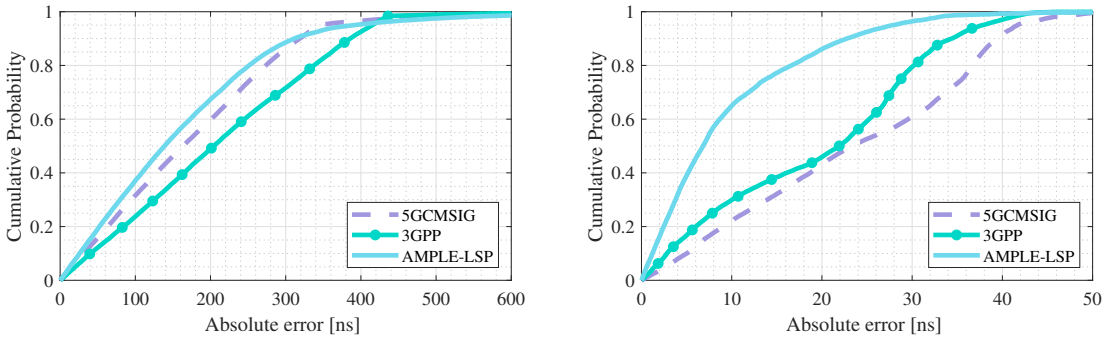

Fig. 5.9 CDF of DS absolute error between model predictions and Ranplan Professional simulations for (a) Outdoor Scenario B and (b) Indoor Office D.

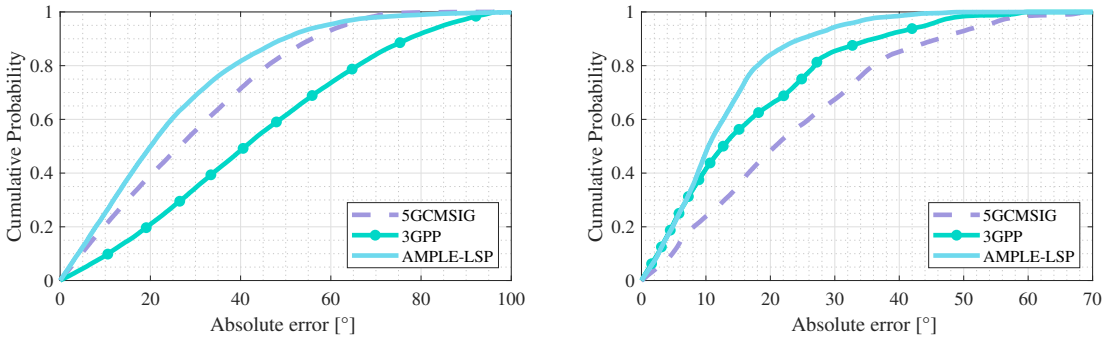

Fig. 5.10 CDF of ASA absolute error between model predictions and Ranplan Professional simulations for (a) Outdoor Scenario B and (b) Indoor Office D.

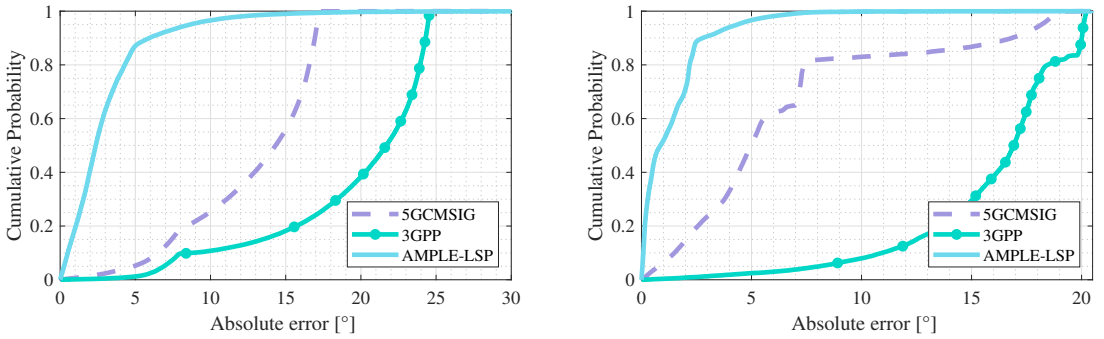

Fig. 5.11 CDF of ZSA absolute error between model predictions and Ranplan Professional simulations for (a) Outdoor Scenario B and (b) Indoor Office D.

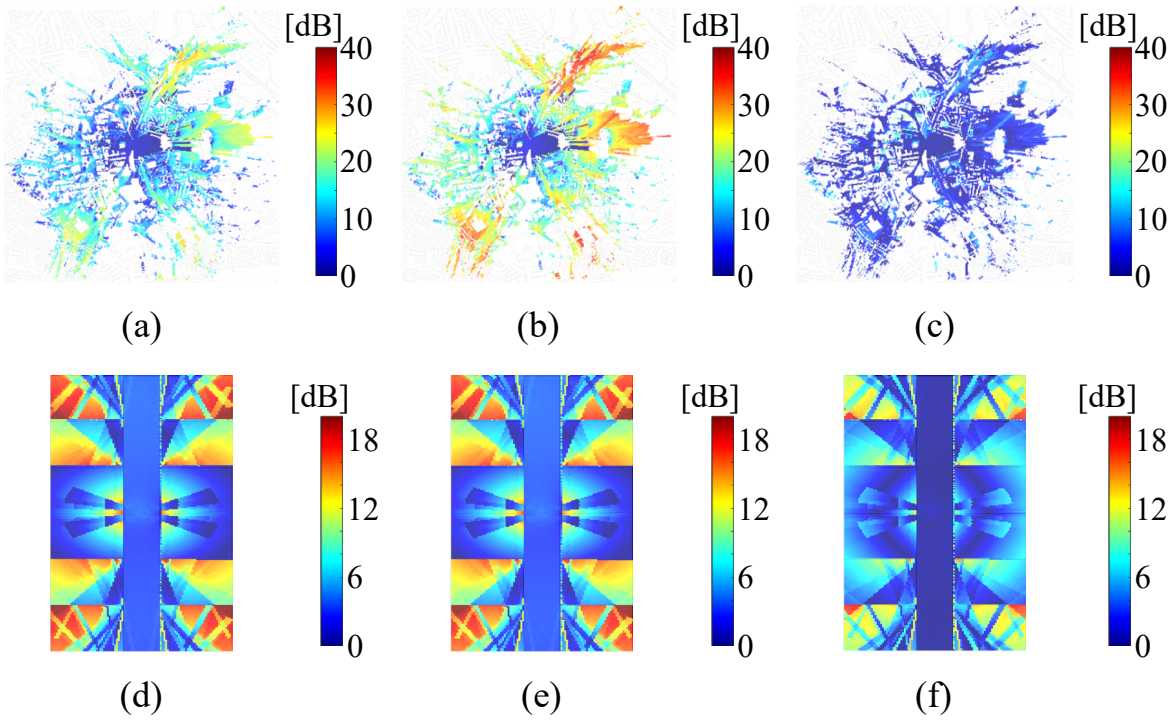

Fig. 5.12 Path loss absolute error maps between Ranplan Professional simulations and model predictions for Outdoor Scenario B (i.e., (a) 5GCMSIG, (b) 3GPP, and (c) AMPLE-LSP) and Indoor Office D (i.e., (d) 5GCMSIG, (e) 3GPP, and (f) AMPLE-LSP).

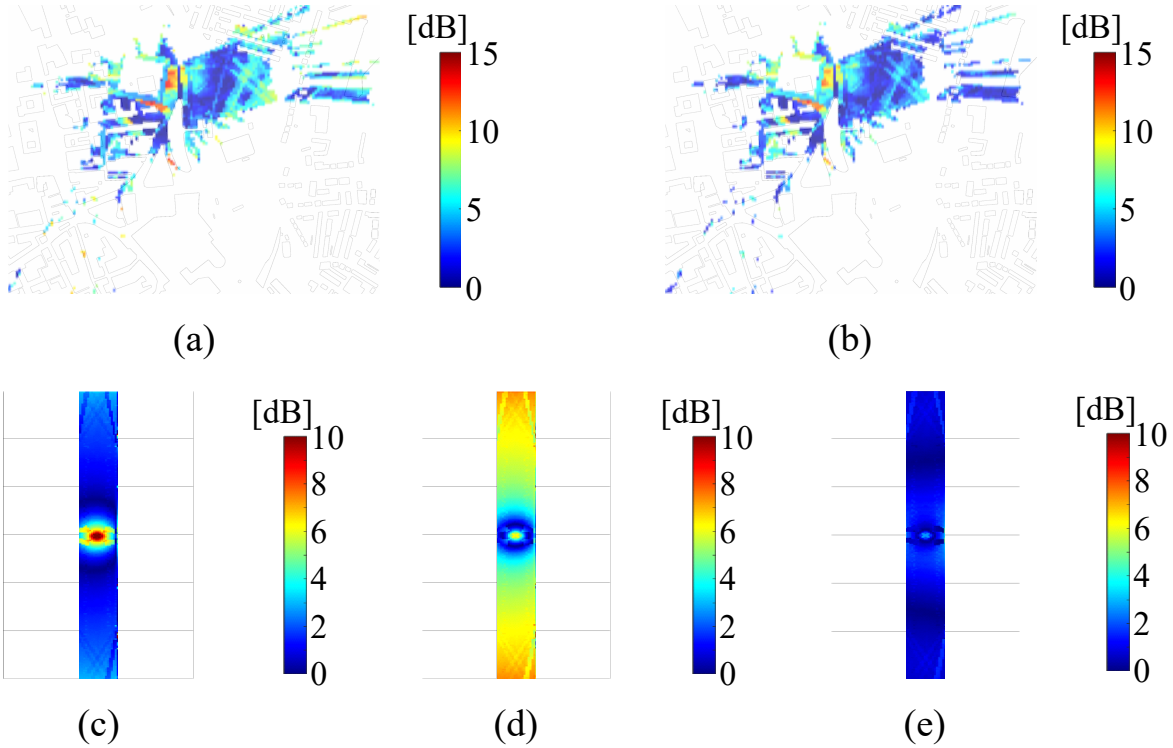

Fig. 5.13 The Ricean K-factor absolute error maps between Ranplan Professional simulations and model predictions for the LOS cases of Outdoor Scenario B (i.e., (a) 5GCMSIG & 3GPP and (b) AMPLE-LSP) and Indoor Office D (i.e., (c) 5GCMSIG, (d) 3GPP, and (e) AMPLE-LSP).

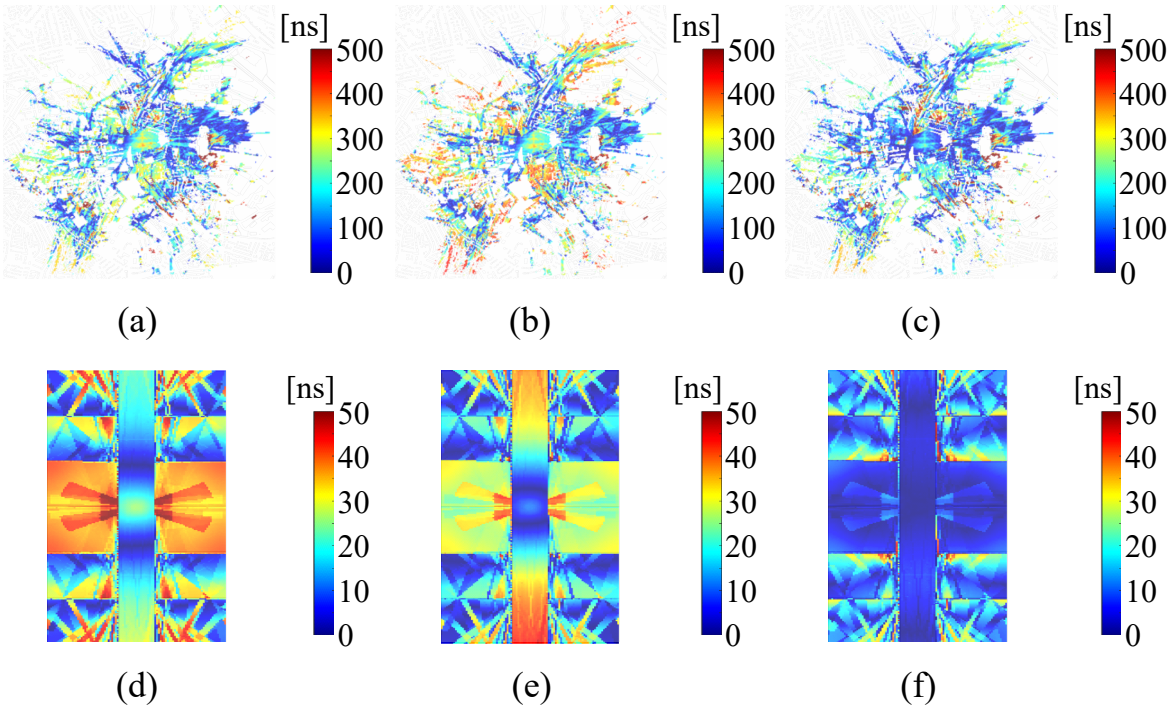

Fig. 5.14 DS absolute error maps between Ranplan Professional simulations and model predictions for Outdoor Scenario B (i.e., (a) 5GCMSIG, (b) 3GPP, and (c) AMPLE-LSP) and Indoor Office D (i.e., (d) 5GCMSIG, (e) 3GPP, and (f) AMPLE-LSP).

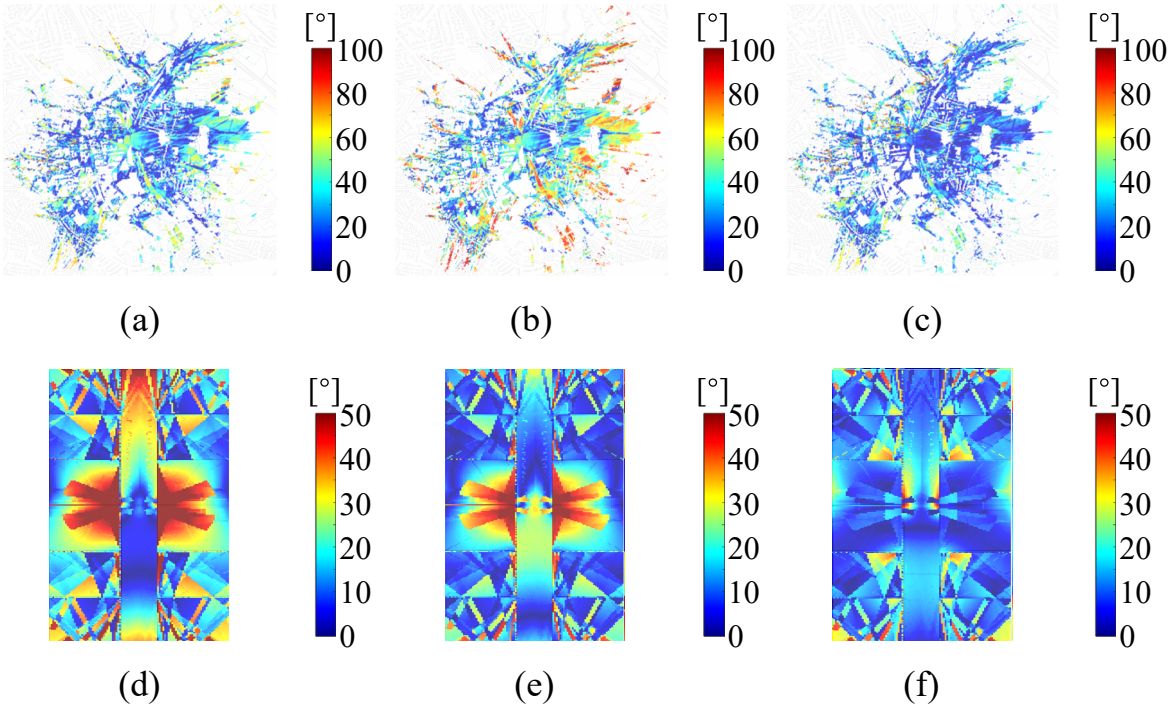

Fig. 5.15 ASA absolute error maps between Ranplan Professional simulations and model predictions for Outdoor Scenario B (i.e., (a) 5GCMSIG, (b) 3GPP, and (c) AMPLE-LSP) and Indoor Office D (i.e., (d) 5GCMSIG, (e) 3GPP, and (f) AMPLE-LSP).

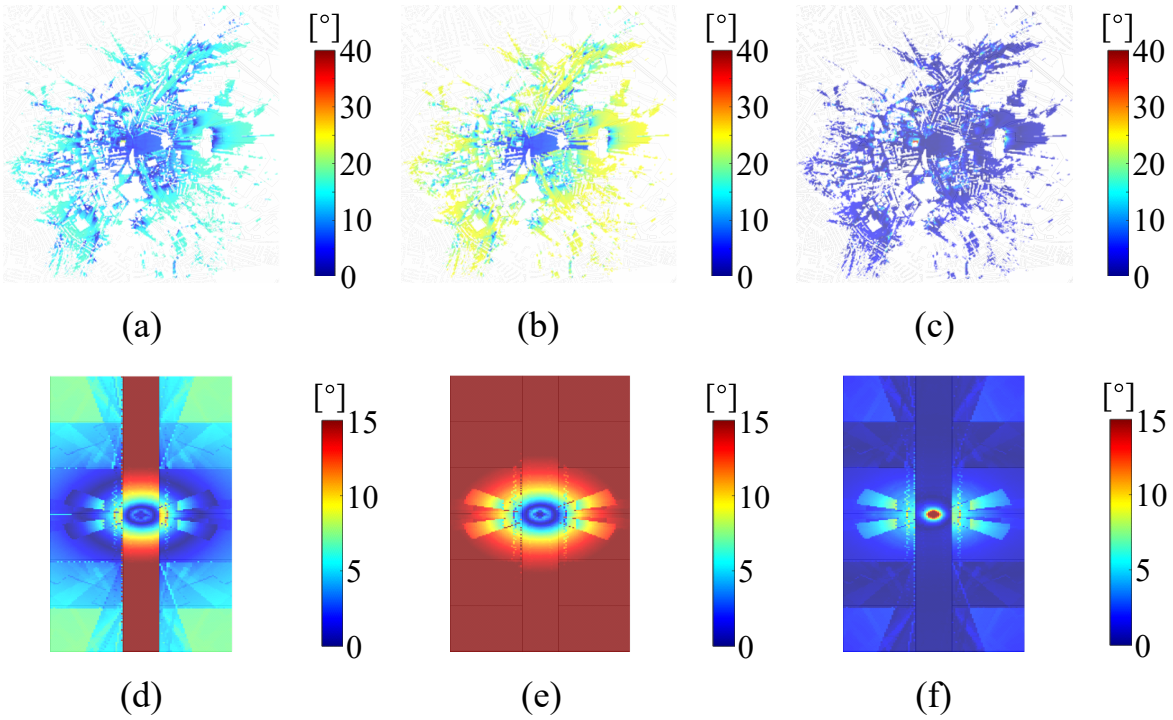

Fig. 5.16 ZSA absolute error maps between Ranplan Professional simulations and model predictions for Outdoor Scenario B (i.e., (a) 5GCMSIG, (b) 3GPP, and (c) AMPLE-LSP) and Indoor Office D (i.e., (d) 5GCMSIG, (e) 3GPP, and (f) AMPLE-LSP).

Generally, the AMPLE-LSP model outperforms both the 3GPP model and the 5GCMSIG model, while maintaining a similar simulation time, in other words, the same level of model complexity. The reasons why the AMPLE-LSP model outperforms the LSP models in the GSCMs are as follows:

- **Influence of distance:** Beyond path loss, which is commonly recognised as a distance-based modelling parameter, other LSPs such as the Ricean K-factor, DS, and ASA/ZSA have also been shown to follow distance-based log-normal distribution models [43–46]. However, in the current GSCMs, they are typically modelled using a single mean value—two examples are shown in Table 5.6 and Table 5.7, and this approach is widely adopted by other GSCMs as well. While such modelling methods were sufficient to capture channel characteristics in the past decades, they are likely to result in significant prediction errors in future radio communication systems [1–3]. This limitation is preliminarily demonstrated by the performance results in Outdoor

Scenario B and Indoor Office D. By further incorporating distance dependence, we enhance the prediction accuracy of LSPs beyond just path loss.

- **Impact of Environment:** The impact of environments plays a significant role in channel LSP predictions. This is evident in GSCMs, which characterise LSPs based on different scenarios (e.g., UMa, UMi, RMa, etc.) and distinguish between LOS and NLOS cases. Still, considering only general environment types is insufficient for achieving more precise predictions. By incorporating detailed environmental factors with low model computation complexity, the AMPLE-LSP model achieves improved prediction accuracy.

Besides, the analysis based on different LSPs are presented as follows.

Path Loss. As we previously investigated [16–18], the AMPLE-LSP model outperforms the 3GPP and 5GCMSIG models in path loss prediction by setting multiple PLEs corresponding to different region types. The AMPLE-LSP model captures more environmental details in both scenarios through its region-specific modelling, resulting in path loss predictions that align more closely with Ranplan simulations than those of the other two models, as shown in Table 5.8, Fig. 5.7, and Fig. 5.12.

Ricean K-factor. Since the power of rays is related to propagation loss, it is reasonable to model the Ricean K-factor with the consideration of environmental factors. Instead of relying on mean values, the AMPLE-LSP model considers both distance and environmental impacts, thereby enhancing the prediction of K values in both scenarios. For both scenarios, the CDFs of absolute error are shown in Fig.5.8, and the error maps are shown in Fig.5.13.

DS. The DS by definition is the standard deviation of multipath excess delays weighted by their respective power (as expressed in (5.4)). In other words, DS does not simply reflect the range of delays in a channel, but rather captures temporal dispersion as shaped by the power distribution of the multipath components. It represents temporal characteristics of the channel and is inherently influenced by the power of each path. Therefore, although DS is a time-domain parameter, both the T-R distance and environmental factors can reasonably be considered as influential in its modelling. Thus, a high DS may result from either large

excess delays associated with high-power components or from a wide range of excess delays with relatively balanced power distribution. Conversely, a low DS may occur when short excess delays dominate with high power, or when longer excess delays exist but carry very low power. Based on this, the AMPLE-LSP model performs slightly better than the other two models, and the results are shown in Table. 5.10, Fig. 5.9, and Fig. 5.14.

ASA/ZSA. Similar to DS, the AS reveals the spatial information of channels with power distribution of multipath components. By further considering T-R distance and environmental factors, the AMPLE-LSP model outperforms the 5GCMSIG and 3GPP models which are with constant predictions only. The comparisons via pefromance metrics are shown in Table 5.11 and Table 5.12, the CDFs of absolute error are shown in Fig. 5.10 and Fig. 5.11, and the error maps are shown in Fig. 5.15 and Fig. 5.16.

5.6 Summary

In this chapter, we first reviewed the distance-based log-normal distributions of LSPs (i.e., path loss, the Ricean K-factor, DS, and AS) from previous research, which, to the best of our knowledge, remain largely unfamiliar to many current researchers in this area. Even without the contributions of this chapter, the distance-based LSP model structure can be considered a future direction for current GSCMs. Following that, we proposed a site-specific LSP prediction approach considering static environmental factors, covering LSP parameters including path loss, the Ricean K-factor, DS, and AS. The proposed model is based on the raster map and simulations/measurements under the target scenario type. To validate the model, we constructed both outdoor and indoor scenarios based on Ranplan Professional channel multipath simulation. The overall results show that the proposed AMPLE-LSP model outperforms the LSP models in the 3GPP channel model and the 5GCMSIG model while maintaining similar model complexity.

By further adding SSP channel modelling or combined with the current 3GPP stochastic channel model, a site-specific stochastic channel model can be potentially constructed, which could be widely used for radio network planning and near real-time network opti-

misation in the current 5G, previous fourth generation (4G), and future 6G and beyond networks. Overall, this chapter reviews and provides two potential paths (the log-distance model in Section 5.2 and the AMPLE-LSP model) for the future development of statistical channel modelling in radio communications and is of great significance in the wireless communications communities.

Chapter 6

Conclusion and Future Work

6.1 Conclusion

In this thesis, we proposed a new method for fast LSP predictions considering propagation environments under the statistical channel model structures. Those LSPs including path loss, the Ricean K-factor, DS, and AS. The proposed methods have three advantages for developing/replacing the future LSP predictions in the GSCMs, that are: 1) Site-specific; 2) Same prediction structure for all the covered LSPs; 3) Once fully generated/characterised, the proposed models have low computational complexity–with the same level of the current empirical LSP models. This thesis can be considered the first systematic study on the AMPLE/AMPLE-LSP model, synthesising existing related works [15–19]. It also serves as a potential basis for the future development of site-specific GSCMs.

In Chapter 3, we proposed the AMPLE model along with both measurement-based and ray-based validation. The AMPLE model is a novel radio propagation model that employs multiple PLEs. At the beginning, the propagation scenario is classified into the region maps, and each environment region type within the region maps is assigned with a specific, initially undefined PLE. To construct the AMPLE model, a straight-line method is proposed to combine the environmental information with path loss data. That is, for each T-R link, a straight line is generated to record the intersected regions, allowing the weighted path loss of these regions to be computed. Once the model is constructed, similar to other empirical

models, the PLEs and associated parameters in the AMPLE model are extracted based on either measurements or ray-based simulations. We validated the AMPLE model in two suburban areas (i.e., UMa scenarios), using both measurement and ray-based data. We also compared the AMPLE model with the 3GPP path loss model and the ABG model defined in the 5GCMSIG model. The results show that the AMPLE model outperforms these two models while maintaining similar model complexity.

In Chapter 4, we enhanced the AMPLE model to support path loss prediction across multiple carrier frequencies. Following that, we characterised the AMPLE model by ray-based simulations from 0.85-5 GHz in both UMa and UMi scenarios. The ray-based simulations are discussed in detail and compared with the measurements reported in [47]. We also provided a standardised characterisation process for the AMPLE model, which can serve as a foundation for future AMPLE-related model construction process. In addition, we presented a more comprehensive model validation with existing statistical radio propagation models used in the GSCMs, compared to the model validation part in Section 3.3 and Section 3.4. We compared the AMPLE model with the 3GPP path loss model, the ABG and CI models in the 5GCMSIG model, and those with simulation calibrations. For performance evaluation, we consider RMSE and MAE for pointwise evaluation, and AHRE for quality evaluation [132–134]. Futhermore, we proposed the PMDE for distributional alignment performance, and the mean simulation time per data point t_p for model complexity evaluation. The results further confirmed the superior performance of the AMPLE model over the compared models. Finally, we provided the characterisation results of the AMPLE model from 0.85 to 5 GHz under the UMa and UMi scenarios.

In Chapter 5, we expended the AMPLE-like modelling method from path loss to other LSPs, including the Ricean K-factor, DS, and AS (for ASA and ZSA). We first introduced the theoretical basis of the extension, that is, the log-distance model for the Ricean K-factor [43, 44], DS [45], and AS (for ASA and ZSA) [46], all of which were proposed in prior measurement-based studies. However, these models remain relatively unknown to the broader research community. Following that, we adopted a modelling process similar to that of the AMPLE model to construct the AMPLE-LSP model, where shared environmental information

is applied consistently across all covered LSPs. We then validated the proposed models using ray-based multipath simulations in both outdoor and indoor scenarios. Compared with the 3GPP-LSP and 5GCMSIG-LSP models, and under the same performance evaluation metrics used in Chapter 4 (i.e., RMSE, MAE, PMDE, and t_p), the AMPLE-LSP model demonstrated superior performance.

6.2 Future Work

Future work can be divided into two directions: refinements for the AMPLE model and for the AMPLE-LSP model, given the significance of path loss compared to other LSPs [4–14]. In this section, we provide a comprehensive and unified overview of the future work, based on the issues and limitations identified in the preceding chapters.

6.2.1 Future Work of the AMPLE Model

In Chapter 3, to meet the requirements of current empirical path loss modelling, which demands a balance between computational complexity and model accuracy for further radio channel modelling (e.g., SSPs), we made a tradeoff between these factors. Still, with more data and/or analysis, the AMPLE model can be expanded and refined, at some cost of complexity. Although the AMPLE model has been enhanced with a frequency coefficient in Chapter 4, there remain opportunities for additional improvements and refinements. We here briefly summarise the limitations and potential refinements of the AMPLE model.

2D Region Map to 3D Region Map.

As we mentioned in Section 4.4.5, the misrecognition of buildings near short-range in the AMPLE model is due to the limitation of 2D region maps. This can be addressed by introducing a 3D region map, that is, the heights of different region types, including buildings. By setting up region heights and 3D T-R distance, the straight-line method can accurately capture intersected regions, thereby eliminating misrecognitions such as unintended building

regions. This refinement would be particularly useful in scenarios such as LOS cases. Also, the PLE-region-type relationship would suffer less noise.

Frequencies, Mainstream Scenarios, and Measurements.

For frequency bands, the current AMPLE model only covers 0.85-5 GHz, and more carrier frequencies must be considered to fulfill the requirements of path loss modelling in 6G or beyond. Also, since we follow the 3GPP channel model standard, which typically considers mainstream scenarios including UMa, UMi, RMa, and InH, we here only cover part of the scenario types. Beyond that, the current AMPLE design is largely based on ray-based simulations, where future characterisation of the AMPLE model should also consider measurements for more real scenarios and variations.

Detailed Scenarios and Terrain Categories.

Since different scenarios have different region type preferences, standard region types may not suit all cases (e.g., for some scenarios, there are no buildings, and, for some cases, there are no trees). In the meantime. the terrain categories are also necessary to be considered, since, even with the same region type, terrains that are flat ground (no abrupt altitude changing) and hilly ground (up and down) may show different impacts towards propagation even under the same scenario type.

Which means, to make the AMPLE model more general and accurate, beyond mainstream scenarios, we need to carefully classify the current typical scenario types and the corresponding region type preferences. Each scenario type contains not only the construction of the scenario itself, but also the detailed terrain categories towards the environment. Overall, from what we could understand, accomplishing the generality of the AMPLE model is harder than previous path loss models (e.g., the ABG model), since it has the potential to cover more environmental information. And, to make it easy to use for the later stages or even the next generations, it would be better to carefully construct the basic datasets.

Model Construction, Extra Modelling, and Future Validation.

For the AMPLE model, a typical problem, of which we simplified in this thesis, is the choice of region types within the initial model construction stage. Small region types, moving obstacles, and weather conditions also impact radio propagation and path loss, and can be considered for further improvement after the basic AMPLE model has been constructed. One potential method is to set up multiple levels of the AMPLE model to address the same scenario type with different environmental complexity. Beyond that, aspects such as model sensitivity, real-world deployment, and computational overhead in large-scale scenarios or multi-frequency scenarios, are unconsidered issues for the AMPLE model at the current stage. However, "first thing first", based on our understanding, these issues are not of primary concern until the AMPLE model reaches a more mature stage of development.

Environment Classification.

For environment classification, beyond k-means clustering which is only suitable for pre-processed maps (e.g., Google Maps, Bing Maps, etc.), deep-learning methods such as convolutional neural networks can be considered for raw maps with arbitrary region shapes (e.g., satellite maps). Additionally, it should be noted that the environment recognition methods used in this thesis are simplified approaches, as the primary focus is on radio propagation. Map classification can be addressed more comprehensively as an image processing and recognition problem, which allows for more general, efficient, and in-depth solutions.

6.2.2 Future Work of the AMPLE-LSP Model

Eventually, the design of the AMPLE-LSP model is intended to be integrated into the main body of the 3GPP channel model as the site-specific LSP modelling part, thereby contributing to the development of a site-specific stochastic channel model for future digital twin channel (DTC) [136, 137]. However, the current AMPLE-LSP model remains a prototype with limited applicability. Based on our current understanding, its limitations and corresponding directions for future work are summarised as follows.

Sufficient Datasets.

To enhance the AMPLE-LSP model based on the prototype presented in Chapter 5, comprehensive parameter extraction across diverse environments is essential. Ideally, the datasets should include LSP measurement/simulation covering typical scenarios such as UMa, UMi, and so on, along with corresponding map data.

Frequency Dependency.

A key limitation of the current AMPLE-LSP model is its inability to support multiple frequency bands using a single set of model parameters, as is commonly done in GSCMs. Similar to the frequency extension applied in the AMPLE model [17] and in other LSP models within existing GSCMs, incorporating frequency dependence into the AMPLE-LSP model is a direction for future enhancement. However, since current research has not yet fully established the frequency dependence of LSPs beyond path loss, we identify this as a potential area for further investigation.

Construction of A Site-Specific GSCM.

Once the AMPLE-LSP model is fully developed, it can replace the LSP predictions in the current GSCMs (e.g., step 3 and 4 in the 3GPP channel model [5]) to construct an environment-concerned GSCM for the modelling of cellular networks. Specifically, for mobile users or dynamic environments, they can be potentially modelled with spatial correlations that are used in both the 3GPP channel model [5] and the QuaDRiGa channel model [7, 8], with a more detailed consideration. This site-specific GSCM would raise the possibility of constructing a DTC with low computational complexity [136, 137].

References

[1] J. Zhang *et al.*, "Channel measurement, modeling, and simulation for 6G: A survey and tutorial," 2023, arXiv: 2305.16616. [Online]. Available: https://arxiv.org/abs/2305.16616

[2] C.-X. Wang *et al.*, "6G wireless channel measurements and models: Trends and challenges," *IEEE Veh. Technol. Mag.*, vol. 15, no. 4, pp. 22–32, Dec. 2020.

[3] C.-X. Wang *et al.*, "A survey of 5G channel measurements and models," *IEEE Commun. Surv. Tutor.*, vol. 20, no. 4, pp. 3142-3168, 4th Quart., 2018.

[4] P. Kyösti *et al.*, *WINNER II channel models, D1.1.2 V1.0*, 2007. [Online]. Available: http://www.signal.uu.se/Publications/WINNER/WIN2D112.pdf

[5] 3GPP, *Study on channel model for frequencies from 0.5 to 100 GHz, V16.1.0*, 2020. [Online]. Available: https://www.etsi.org

[6] 3GPP, *Spatial channel model for multiple input multiple output (MIMO) simulations, V11.0.0*, 2003. [Online]. Available: https://www.etsi.org

[7] S. Jaeckel *et al.*, "QuaDRiGa: A 3-D multi-cell channel model with time evolution for enabling virtual field trials," *IEEE Trans. Antennas Propag.*, vol. 62, no. 6, pp. 3242–3256, June 2014.

[8] S. Jaeckel *et al.*, *QuaDRiGa—Quasi deterministic radio channel generator, user manual and documentation, V2.0.0*, 2017. [Online]. Available: https://quadriga-channel-model.de

[9] NTT Docomo *et al.*, *5G channel model for bands up to 100 GHz, V2.0*, 2016. [Online]. Available: http://www.5gworkshops.com

[10] M. Peter *et al.*, *Measurement campaigns and initial channel models for preferred suitable frequency ranges, Deliverable D2.1,* 2016. [Online]. Available: https://ec.europa.eu/research/participants/documents/downloadPublic?documentIds-=080166e5a7a6b182&appId=PPGMS

[11] V. Nurmela *et al.*, *METIS channel models, Deliverable D1.4,* 2015. [Online]. Available: https://www.researchgate.net/publication/282807948

[12] ITU-R SG05, *Draft new report ITU-R m. [IMT-2020.eval]*, 2017. [Online]. Available: https://www.itu.int/md/R15-SG05-C-0057/en

[13] L. Liu *et al.*, "The COST 2100 MIMO channel model," *IEEE Wireless Commun. Mag.*, vol. 19, no. 6, pp. 92–99, Dec. 2012.

[14] H. Poddar *et al.*, "A tutorial on NYUSIM: Sub-terahertz and millimeter-wave channel simulator for 5G, 6G, and beyond," *IEEE Commun. Surv. Tutor.*, vol. 26, no. 2, pp. 824–857, 2nd Quart., 2024.

[15] J. Zhang *et al.*, "A method of fast path loss calculation considering environmental factors," WO2023214176A1, 2023. [Online]. Available: https://patents.google.com/patent/WO2023214176A1/en?oq=WO2023214176A1

[16] L. Zhou *et al.*, "AMPLE: An adaptive multiple path loss exponent radio propagation model considering environmental factors," *IEEE Trans. Veh. Technol.*, vol. 74, no. 2, pp. 3395-3400, Feb. 2025.

[17] L. Zhou *et al.*, "An environment-adaptive radio propagation path loss model with ray-based validation," *IEEE Antennas Wireless Propag. Lett.*, vol. 23, no. 10, pp. 3217-3221, Oct. 2024.

[18] L. Zhou *et al.*, "Ray-based characterization of the AMPLE model from 0.85 to 5 GHz," *IEEE Trans. Antennas Propag.*, vol. 73, no. 10, pp. 8174-8188, Oct. 2025.

[19] L. Zhou *et al.*, "A site-specific channel large-scale parameter model with ray-based validation," *IEEE Trans. Veh. Technol.*, early access, Dec. 2025, doi: 10.1109/TVT.2025.3640770.

[20] L. Xiao *et al.*, "Characterization of the AMPLE channel model for IEEE 802.11ah-Based IoT," in *Proc. 2025 IEEE 25th Int. Conf. Commun. Technol. (ICCT)*, 2025, pp. 139-143.

[21] J. W. Schuster, and R. J. Luebbers, "Comparison of GTD and FDTD predictions for UHF radio wave propagation in a simple outdoor urban environment," in *Proc. IEEE Antennas Propag. Soc. Int. Symp. Dig.*, Montreal, QC, Canada, 1997, pp. 2022-2025.

[22] T. M. Schäfer and W. Wiesbeck, "Simulation of radiowave propagation in hospitals based on FDTD and ray-optical methods," *IEEE Trans. Antennas Propag.*, vol. 53, no. 8, pp. 2381–2388, Aug. 2005.

[23] A. C. M. Austin, M. J. Neve, and G. B. Rowe, "Modeling propagation in multifloor buildings using the FDTD method," *IEEE Trans. Antennas Propag.*, vol. 59, no. 11, pp. 4239–4246, Nov. 2011.

[24] *Introduction to Finite Element Analysis*, accessed on July 2025. [Online]. Available: https://www.engr.uvic.ca/ mech410/lectures/FEA_Theory.pdf

[25] R. Xu, H. Zhu, and J. Yuan, "Electric-field intrabody communication channel modeling with finite-element method," *IEEE Trans. Biomed. Eng.*, vol. 58, no. 3, pp. 705-712, Mar. 2011.

[26] A. M. Eid and J. W. Wallace, "Accurate modeling of body area network channels using surface-based method of moments," *IEEE Trans. Antennas Propag.*, vol. 59, no. 8, pp. 3022–3030, Aug. 2011.

[27] R. F. Harrington, *Field Computation by Moment Methods*. Piscataway, NJ, USA: Wiley, 1993.

[28] R. Marklein, “The finite integration technique as a general tool to compute acoustic, electromagnetic, elastodynamic, and coupled wave fields,” *Rev. Radio Sci.*, pp. 201–244, 2002.

[29] Z. Yun and M. F. Iskander, “Ray tracing for radio propagation modeling: Principles and applications,” *IEEE Access*, vol. 3, pp. 1089–1100, 2015.

[30] D. He *et al.*, “The design and applications of high-performance ray-tracing simulation platform for 5G and beyond wireless communications: A tutorial,” *IEEE Commun. Surv. Tutor.*, vol. 21, no. 1, pp. 10–27, 1st Quart., 2019.

[31] G. Yu *et al.*, “A ray-launching algorithm for polarized wireless channel prediction,” in *Proc. IEEE Glob. Commun. Conf. Workshops (GlobCom Wkshps)*, Kuala Lumpur, Malaysia, Dec. 4-8, 2023, pp. 1928-1933.

[32] *CST Studio Suite*, 2025. [Online]. Available: https://www.3ds.com/products/simulia/cst-studio-suite

[33] K. Ito, I. Ida, and M.-S. Wu, “Body effect on characteristics of small loop antenna in pager systems,” in *Proc. IEEE Antennas Propag. Soc. Int. Symp. (Digest)*, Chicago, IL, USA, June 1992, pp. 1081-1084.

[34] M. Särestöniemi, M. Hämäläinen, and J. Iinatti, “An overview of the electromagnetic simulation-based channel modeling techniques for wireless body area network applications,” *IEEE Access*, vol. 5, pp. 10622–10632, May 2017.

[35] J. B. Cole, “A high accuracy FDTD algorithm to solve microwave propagation and scattering problems on a coarse grid,” *IEEE Trans. Microw. Theory Tech.*, vol. 43, no. 9, pp. 2053-2058, Sept. 1995.

[36] D. T. Paris and F. K. Hurd, *Basic Electromagnetic Theory*. New York, USA: McGraw-Hill, 1969.

[37] A. Maltsev *et al.*, *Channel Models for IEEE 802.11ay*, document 802.11-15/1150r9, IEEE, New York, USA, 2016.

[38] *Channel Models for 60 GHz WLAN Systems*, IEEE 902.11ad, May 2010. [Online]. Available: https://www.ieee802.org/11/Reports/tgad_update.htm

[39] A. Maltsev *et al.*, *MiWEBA D5.1: Channel modeling and characterization, Deliverable D5.1,* 2014. [Online]. Available: https://www.google.com/search?q=MiWEBA+D5.1

[40] A. Goldsmith, *Wireless Communications*. Cambridge: Cambridge University Press, 2005.

[41] T. S. Rappaport, *Wireless Communications: Principles and Practice*. New Jersey, USA: Prentice Hall, 1996.

[42] V. Erceg *et al.*, "An empirically based path loss model for wireless channels in suburban environments," *IEEE J. Sel. Areas Commun.*, vol. 17, no. 7, pp. 1205–1211, July 1999.

[43] L. J. Greenstein *et al.*, "Ricean K-factors in narrow-band fixed wireless channels: Theory, experiments, and statistical models," *IEEE Trans. Veh. Technol.*, vol. 58, no. 8, pp. 4000–4012, Oct. 2009.

[44] P. Tang *et al.*, "Estimation of the K-factor for temporal fading from single-snapshot wideband measurements," *IEEE Trans. Veh. Technol.*, vol. 68, no. 1, pp. 49–63, Jan. 2019.

[45] L. J. Greenstein *et al.*, "A new path-gain/delay-spread propagation model for digital cellular channels," *IEEE Trans. Veh. Technol.*, vol. 46, no. 2, pp. 477–485, May 1997.

[46] R. Zhang *et al.*, "Measurement and modeling of angular spreads of three-dimensional urban street radio channels," *IEEE Trans. Veh. Technol.*, vol. 66, no. 5, pp. 3555–3570, May 2017.

[47] S. Sun, *et al.*, "Investigation of prediction accuracy, sensitivity, and parameter stability of large-scale propagation path loss models for 5G wireless communications," *IEEE Trans. Veh. Technol.*, vol. 65, no. 5, pp. 2843–2860, May 2016.

[48] F. A. Aoudia *et al.*, "Sionna RT: Technical report," 2025, arXiv: 2504.21719. [Online]. Available: https://arxiv.org/abs/2504.21719

[49] K. Guan *et al.*, "Towards realistic high-speed train channels at 5G millimeter-wave band—Part I: Paradigm, significance analysis, and scenario reconstruction," *IEEE Trans. Veh. Technol.*, vol. 67, no. 10, pp. 9112–9128, Oct. 2018.

[50] K. Guan *et al.*, "Towards realistic high-speed train channels at 5G millimeter-wave band—Part II: Case study for paradigm implementation," *IEEE Trans. Veh. Technol.*, vol. 67, no. 10, pp. 9129–9144, Oct. 2018.

[51] C. Phillips, D. Sicker, and D. Grunwald, "A survey of wireless path loss prediction and coverage mapping methods," *IEEE Commun. Surveys Tuts.*, vol. 15, no. 1, pp. 255–270, 1st Quart., 2013.

[52] H. T. Friis, "A note on a simple transmission formula," *Proc. IRE*, vol. 34, no. 5, pp. 254–256, May 1946.

[53] A. S. Glassner, *An Introduction to Ray Tracing*. San Francisco, CA, USA: Academic, 1989.

[54] J. Keller, "One hundred years of diffraction theory," *IEEE Trans. Antennas Propag.*, vol. 33, no. 2, pp. 123–126, Feb. 1985.

[55] K. Bullington, "Radio propagation at frequencies above 30 megacycles," *Proc. IRE*, vol. 35, no. 10, pp. 1122–1136, Oct. 1947.

[56] C. L. Giovaneli, "An analysis of simplified solutions for multiple knife-edge diffraction," *IEEE Trans. Antennas Propag.*, vol. 32, no. 3, pp. 297–310, Mar. 1984.

[57] J. B. Keller, "Geometrical theory of diffraction," *J. Opt. Soc. Amer.*, vol. 32, no. 2, pp. 116–130, Feb. 1962.

[58] R. G. Kouyoumjian and P. H. Pathak, "A uniform geometrical theory of diffraction for an edge in a perfectly conducting surface," *Proc. IEEE*, vol. 62, no. 11, pp. 1448–1461, Nov. 1974.

[59] P. D. Holm, "A new heuristic UTD diffraction coefficient for nonperfectly conducting wedges," *IEEE Trans. Antennas Propag.*, vol. 48, no. 8, 1211–1219, Aug. 2000.

[60] C. Tzaras and S. R. Saunders, "An improved heuristic UTD solution for multiple-edge transition zone diffraction," *IEEE Trans. Antennas Propag.*, vol. 49, no. 12, pp. 1678–1682, Dec. 2001.

[61] P. Bernardi, R. Cicchetti, and O. Testa, "A three-dimensional UTD heuristic diffraction coefficient for complex penetrable wedges," *IEEE Trans. Antennas Propag.*, vol. 50, no. 2, pp. 217–224, Feb. 2002.

[62] R. J. Luebbers, "Comparison of lossy wedge diffraction coefficients with application to mixed path propagation loss prediction," *IEEE Trans. Antennas Propag.*, vol. 36, no. 7, pp. 1031–1034, Jul. 1988.

[63] Y. L. C. de Jong and M. H. A. J. Herben, "A tree-scattering model for improved propagation prediction in urban microcells," *IEEE Trans. Veh. Technol.*, vol. 53, no. 2, pp. 503–513, Mar. 2004.

[64] M. Kvicera, F. Pérez-Fontán, and P. Pechac, "Scattering from single isolated tree based on physical optics: Preliminary model," in *Proc. 9th Eur. Conf. Antennas Propag. (EuCAP)*, Lisbon, Portugal, May 2015, pp. 1–4.

[65] M. Kvicera *et al.*, "Sensitivity analysis of multiple scattering theory applied to tree canopies at microwave frequencies," in *IEEE Antennas Wireless Propag. Lett.*, vol. 15, pp. 1175-1178, 2016.

[66] M. Kvicera *et al.*, "A new model for scattering from tree canopies based on physical optics and multiple scattering theory," *IEEE Trans. Antennas Propag.*, vol. 36, no. 7, pp. 1031–1034, Jul. 1988.

[67] P. Kersaudy *et al.*, "Stochastic analysis of scattered field by building facades using polynomial chaos," *IEEE Trans. Antennas Propag.*, vol. 62, no. 12, pp. 6382–6393, Dec. 2014.

[68] E. M. Vitucci *et al.*, "Polarimetric properties of diffuse scattering from building walls: Experimental parameterization of a ray-tracing model," *IEEE Trans. Antennas Propag.*, vol. 60, no. 6, pp. 2961–2969, June 2012.

[69] P. Pongsilamanee and H. L. Bertoni, "Specular and nonspecular scattering from building facades," *IEEE Trans. Antennas Propag.*, vol. 52, no. 7, pp. 1879–1889, July 2004.

[70] V. Degli-Esposti, "A diffuse scattering model for urban propagation prediction," *IEEE Trans. Antennas Propag.*, vol. 49, no. 7, pp. 1111–1113, July 2001.

[71] G. Gougeon, Y. Lostanlen, and L. Maviel, "Coupling a deterministic propagation model with diffuse scattering and urban furniture for small cells," in *Proc. Eur. Conf. Antennas Propag. (EuCAP)*, Rome, Italy, Apr. 2011, pp. 3448–3452.

[72] J. S. Lu *et al.*, "Measurement and characterization of various outdoor 60 GHz diffracted and scattered paths," in *Proc. IEEE Mil. Commun. Conf. (MILCOM)*, San Diego, CA, USA, Nov. 2013, pp. 1238–1243.

[73] G. Li *et al.*, "Connected vehicle channels: On the consideration of electromagnetic scattering from local scatterers," *IEEE Trans. Veh. Technol.*, vol. 67, no. 9, pp. 7910–7923, Mar. 2018.

[74] M. M. Taygur and T. F. Eibert, "A ray-tracing algorithm based on the computation of (exact) ray paths with bidirectional ray-tracing," *IEEE Trans. Antennas Propag.*, vol. 68, no. 8, pp. 6277–6286, Aug. 2020.

[75] H. Ling, R.-C. Chou, and S.-W. Lee, "Shooting and bouncing rays: Calculating the RCS of an arbitrarily shaped cavity," *IEEE Trans. Antennas Propag.*, vol. 37, no. 2, pp. 194–205, Feb. 1989.

[76] T. Imai, "A survey of efficient ray-tracing techniques for mobile radio propagation analysis," *IEICE Trans. Commun.*, vol. 100, no. 5, pp. 666–679, 2017.

[77] H. Obeidat *et al.*, "Indoor environment propagation review," *Comput. Sci. Rev.*, vol. 37, pp. 1–22, Aug. 2020.

[78] D. S. Baum *et al.*, *Final report on link level and system level channel models, D5.4 V1.4*, 2005. [Online]. Available: https://www.researchgate.net/publication/229031750

[79] H. Xiao, A. Burr, and L. Song, "A time-variant wideband spatial channel model based on the 3GPP model," in *Proc. IEEE Veh. Technol. Conf. (VTC Fall)*, Montreal, QC, Canada, Sept. 25–28, 2006, pp. 1-5.

[80] D. S. Baum *et al.*, "An interim channel model for beyond-3G systems: Extending the 3GPP spatial channel model (SCM)," in *Proc. IEEE 61st Veh. Technol. Conf. (VTC Spring)*, Stockholm, Sweden, May 30 – Jun. 1, 2005, pp. 1-5.

[81] L. Correia, *Mobile Broadband Multimedia Networks*. London, UK: Elsevier, 2006.

[82] S. Wu *et al.*, "A general 3-D non-stationary 5G wireless channel model," *IEEE Trans. Commun.*, vol. 66, no. 7, pp. 3065-3078, July 2018.

[83] X. Cheng *et al.*, "Wideband channel modeling and ICI cancellation for vehicle-to-vehicle communication systems," *IEEE J. Sel. Areas Commun.*, vol. 31, no. 9, pp. 434–448, Sept. 2013.

[84] X. Cheng *et al.*, "Two-cylinder and multi-ring GBSSM for realizing and modeling of vehicle-to-vehicle wideband MIMO channels," *IEEE Trans. Intell. Transp. Syst.*, vol. 17, no. 10, pp. 2787–2799, Oct. 2016.

[85] A. Borhani and M. Pätzold, "Correlation and spectral properties of vehicle-to-vehicle channels in the presence of moving scatterers," *IEEE Trans. Veh. Technol.*, vol. 62, no. 9, pp. 4228–4239, Nov. 2013.

[86] A. Chelli and M. Pätzold, "A non-stationary MIMO vehicle-to-vehicle channel model derived from the geometrical street model," in *Proc. IEEE 74th Veh. Technol. Conf. (VTC Fall)*, San Francisco, CA, USA, Sept. 5-8, 2011, pp. 1-6.

[87] M. Hata, "Empirical formula for propagation loss in land mobile radio services," *IEEE Trans. Veh. Technol.*, vol. 29, no. 3, pp. 317–325, Aug. 1980.

[88] Y. Okumura *et al.*, "Field strength and its variability in VHF and UHF land mobile radio service," *Rev. Elec. Commun. Lab.*, vol. 16, 1968.

[89] COST, *COST Action 231: Digital mobile radio towards future generation systems, Final report*, 1999. [Online]. Available: https://op.europa.eu/en/publication-detail/-/publication/f2f42003-4028-4496-af95-beaa38fd475f

[90] TIA, *Wireless communications systems-performance in noise and interference-limited situations-recommentded methods for technology-independent modeling, simulation, and verifications*, 2004. [Online]. Available: https://fasma.org/wp-content/uploads/TSB-88-B-Wireless-Communications-Systems-Performance-in-Noise-and-Interference-Limited-Situations-Recommended-Methods-for-Technology-Independent-Modeling-Simulation-and-Verifications.pdf

[91] ECC-CEPT, *The analysis of the coexistence of point-to-multipoint FWS cells in the 3.4-3.8 GHz band*, 2006. [Online]. Available: https://docdb.cept.org/download/292

[92] A. Medeisis and A. Kajackas, "On the use of the universal Okumura-Hata propagation prediction model in rural areas," in *Proc. 51st IEEE Veh. Technol. Conf. (VTC Spring)*, Tokyo, Japan, May 15-18, 2000, pp. 1815-1818.

[93] ITU-R, *Prediction methods for the terrestrial land mobile service in the VHF and UHF bands, Recommendation ITU-R P.529-3*, 1999. [Online]. Available: https://www.itu.int/rec/R-REC-P.529/en

[94] S. I. Umana, N. O. Akpbio, and S. E. Mbong, "Stanford university interim propagation loss model for a gmelina arborea tree-lined road," *Rev. Comput. Eng. Res.*, vol. 5, no. 2, pp. 57–63, 2018.

[95] V. Erceg *et al.*, *Channel models for fixed wireless applications*, 2003. [Online]. Available: https://www.ieee802.org/16/tg3/contrib/802163c-01_29r4.pdf

[96] S. Sun *et al.*, "Propagation path loss models for 5G urban micro-and macro-cellular scenarios," in *Proc. IEEE 83rd Veh. Technol. Conf. (VTC Spring)*, Nanjing, China, May 15-18, 2016, pp. 1-6.

[97] S.R. Saunders and F.R. Bonar, "Explicit multiple building diffraction attenuation function for mobile radio wave propagation," *Electron. Lett.*, vol. 27, no. 14, pp. 1276–1277, July 1991.

[98] G. D. Durgin, T. S. Rappaport, and H. Xu, "Partition-based path loss analysis for in-home and residential areas at 5.85 GHz," in *Proc. IEEE Global Commun. Conf. (GLOBECOM)*, Sydney, Australia, Nov. 8–12, 1998, pp. 904-909.

[99] G. D. Durgin, T. S. Rappaport, and H. Xu, "Measurements and models for radio path loss and penetration loss in and around homes and trees at 5.85 GHz," *IEEE Trans. Commun.*, vol. 46, no. 11, pp. 1484–1496, Nov. 1998.

[100] L. Zhou *et al.*, "A fast path loss model for wireless channels considering environmental factors," 2023, arXiv: 2303.12441. [Online]. Available: https://arxiv.org/abs/2303.12441v1

[101] C. Gustafson *et al.*, "Statistical modeling and estimation of censored pathloss data," *IEEE Wireless Commun. Lett.*, vol. 4, no. 5, pp. 569–572, Oct. 2015.

[102] B. Eric, *LoRa documentation*, 2019. [Online]. Available: https://buildmedia.readthedocs.org/media/pdf/lora/latest/lora.pdf

[103] O. Cetinkaya *et al.*, "Distributed sensing with low-cost mobile sensors toward a sustainable IoT," *IEEE Internet Thing Mag.*, vol. 4, no. 3, pp. 96-102, Sept. 2021.

[104] A. C. Cohen, *Truncated and Censored Samples: Theory and Applications.* New York, USA: Marcel Dekker, 1991.

[105] J. Miranda *et al.*, "Path loss exponent analysis in wireless sensor networks: Experimental evaluation," in *Proc. IEEE Int. Conf. Ind. Inform. (INDIN)*, Bochum, Germany, July 29–31, 2013, pp. 54-58.

[106] G. Peterson, "The application of electromagnetic surface waves to wireless energy transfer," in *Proc. IEEE Wireless Power Transfer Conf. (WPTC)*, Boulder, CO, USA, May 13–15, 2015, pp. 1-4.

[107] R. W. P. King, "Electromagnetic surface waves: New formulas and applications," *IEEE Trans. Antennas Propag.*, vol. 33, no. 11, pp. 1204–1212, Nov. 1985.

[108] *Ranplan Professional*, 2026. [Online]. Available: https://www.ranplanw ireless.com/products/professional

[109] Z. Lai *et al.*, "Intelligent ray launching algorithm for indoor scenarios," *Radio engineering*, vol. 20, no. 2, pp. 398-408, June 2011.

[110] W. Yang *et al.*, "Verification of an intelligent ray launching algorithm in indoor environments in the Ka-band," *Radio Sci.*, vol. 56, no. 9, pp. 1-11, Sept. 2021.

[111] W. Yang *et al.*,"Indoor measurement based verification of ray launching algorithm at the Ka-band," in *Proc. XXXIIIrd Gen. Assem. Sci. Symp. Int. Union Radio Sci. (URSI GASS)*, Rome, Italy, Aug. 29-Sept. 5, 2020, pp. 1-4.

[112] K. Qiu *et al.*, "Pseudo ray-tracing: Deep leaning assisted outdoor mm-wave path loss prediction," *IEEE Wireless Commun. Lett.*, vol. 11, no. 8, pp. 1699–1702, Aug. 2022.

[113] C. Qin *et al.*, "Simulation based channel hardening of cell-free massive MIMO in mm-wave," in *Proc. XXXIVth Gen. Assem. Sci. Symp. Int. Union Radio Sci. (URSI GASS)*, Rome, Italy, Aug. 28–Sept. 4, 2021, pp. 1–4.

[114] S. Bakirtzis *et al.*, "EM DeepRay: An expedient, generalizable, and realistic data-driven indoor propagation model," *IEEE Trans. Antennas Propag.*, vol. 70, no. 6, pp. 4140–4154, June 2022.

[115] *Digimap.* [Online]. Available: https://digimap.edina.ac.uk

[116] Ordnance Survey (GB), OS Open Map - Local [SHAPE geospatial data], Scale 1:10000, Tiles: se, Updated: 12 October 2023, Using: EDINA Digimap Ordnance Survey Service, Downloaded: May 2024. [Online]. Available: https://digimap.edina.ac.uk

[117] X. Zhang and J. G. Andrews, "Downlink cellular network analysis with multi-slope path loss models," *IEEE Trans. Commun.*, vol. 63, no. 5, pp. 1881–1894, Mar. 2015.

[118] J. Senic *et al.*, "Analysis of e-band path loss and propagation mechanisms in the indoor environment," *IEEE Trans. Antennas Propag.*, vol. 65, no. 12, pp. 6562-6573, Dec. 2017.

[119] P. Zhang *et al.*, "In-building coverage of millimeter-wave wireless networks from channel measurement and modeling perspectives," *Sci. China Inf. Sci.*, vol. 63, no.8, pp. 1-16, Aug. 2020.

[120] Y. Chang *et al.*, "A novel dual-slope mm-wave channel model based on 3D ray-tracing in urban environments," in *Proc. IEEE Int. Symp. Pers. Indoor Mob. Radio Commun. (PIMRC)*, Washington, DC, USA, Sept. 2–5, 2014, pp. 222-226.

[121] T. Kwon *et al.*, "RF lens-embedded massive MIMO systems: Fabrication issues and codebook design," *IEEE Trans. Microw. Theory Tech.*, vol. 64, no. 7, pp. 2256–71, July 2016.

[122] Y.-J. Cho *et al.*, "RF lens-embedded antenna array for mmWave MIMO: Design and performance," *IEEE Commun. Mag.*, vol. 56, no. 7, pp. 42–48, July 2018.

[123] B. Ai *et al.*, "On indoor millimeter wave massive MIMO channels: Measurement and simulation," *IEEE J. Sel. Areas Commun.*, vol. 35, no. 7, pp. 1678–1690, July 2017.

[124] Y.-G. Lim *et al.*, "Waveform multiplexing for new radio: Numerology management and 3D evaluation," *IEEE Wirel. Commun.*, vol. 25, no. 5, pp. 86–94, Oct. 2018.

[125] K. Guan *et al.*, "Channel characterization for intra-wagon communication at 60 and 300 GHz bands," *IEEE Trans. Veh. Technol.*, vol. 68, no. 6, pp. 5193-5207, June 2019.

[126] Y.-G. Lim *et al.*, "Map-based millimeter-wave channel models: An overview, data for B5G evaluation and machine learning," *IEEE Wireless Commun.*, vol. 27, no. 4, pp. 54–62, Aug. 2020.

[127] J. Zhang *et al.*, "Spatial scattering modulation with multipath component aggregation," *IEEE Trans. Green Commun. Netw.*, vol.8, no. 1, pp. 18-34, Mar. 2024.

[128] J. Zhang *et al.*, "Performance evaluation of spatial scattering modulation in the indoor environment," in *Proc. Int. Symp. Wirel. Commun. Syst. (ISWCS)*, Hangzhou, China, Oct. 19-22, 2022, pp. 1-6.

[129] J. M. Rigelsford *et al.*, *Wireless/Energy efficiency of typical building components and architecture, Deliverable D1.2*, 2013. [Online]. Available: https://cordis.europa.eu/project/id/286333/reporting/es

[130] ITU-R, *Electrical characteristics of the surface of the Earth*, 2021. [Online]. Available: https://www.itu.int/rec/r-rec-p.527/en

[131] ITU-R, *Attenuation in vegetation*, 2021. [Online]. Available: https://www.itu.int/rec/r-rec-p.833/en

[132] A. S. Owadally, E. Montiel, and S. R. Saunders, "A comparison of the accuracy of propagation models using hit rate analysis," in *Proc. 54th IEEE Veh. Technol. Conf. (VTC Fall)*, Atlantic City, NJ, USA, Oct. 7–11, 2001, pp. 1979-1983.

[133] E. Östlin, H. -J. Zepernick, and H. Suzuki, "Evaluation of the new semi-terrain based propagation model recommendation ITU-R P.1546," in *Proc. 58th IEEE Veh. Technol. Conf. (VTC Fall)*, Orlando, FL, USA, Oct. 6–9, 2003, pp. 114-118.

[134] E. Östlin, H.-J. Zepernick, and H. Suzuki, "Macrocell path-loss prediction using artificial neural networks," *IEEE Trans. Veh. Technol.*, vol. 59, no. 6, pp. 2735–2747, July 2010.

[135] Y. Xiao, "IEEE 802.11n: Enhancements for higher throughput in wireless LANs," *IEEE Wireless Commun.*, vol. 12, no. 6, pp. 82–91, Dec. 2005.

[136] H. Gao *et al.*, "Digital twin enabled 6G radio testing: Concepts, challenges and solutions," *IEEE Commun. Mag.*, vol. 61, no. 11, pp. 88-94, Nov. 2023.

[137] J. Wang *et al.*, "Towards 6G digital twin channel using radio environment knowledge pool," 2023, arXiv: 2312.10287. [Online]. Available: https://arxiv.org/abs/2312.10287

RightsLink

LZ

AMPLE: An Adaptive Multiple Path Loss Exponent Radio Propagation Model Considering Environmental Factors

Author: Lingyou Zhou
Publication: IEEE Transactions on Vehicular Technology
Publisher: IEEE
Date: February 2025

Thesis / Dissertation Reuse

The IEEE does not require individuals working on a thesis to obtain a formal reuse license, however, you may print out this statement to be used as a permission grant:

Requirements to be followed when using any portion (e.g., figure, graph, table, or textual material) of an IEEE copyrighted paper in a thesis:

1) In the case of textual material (e.g., using short quotes or referring to the work within these papers) users must give full credit to the original source (author, paper, publication) followed by the IEEE copyright line © 2011 IEEE.
2) In the case of illustrations or tabular material, we require that the copyright line © [Year of original publication] IEEE appear prominently with each reprinted figure and/or table.
3) If a substantial portion of the original paper is to be used, and if you are not the senior author, also obtain the senior author's approval.

Requirements to be followed when using an entire IEEE copyrighted paper in a thesis:

1) The following IEEE copyright/ credit notice should be placed prominently in the references: © [year of original publication] IEEE. Reprinted, with permission, from [author names, paper title, IEEE publication title, and month/year of publication]
2) Only the accepted version of an IEEE copyrighted paper can be used when posting the paper or your thesis on-line.
3) In placing the thesis on the author's university website, please display the following message in a prominent place on the website: In reference to IEEE copyrighted material which is used with permission in this thesis, the IEEE does not endorse any of [university/educational entity's name goes here]'s products or services. Internal or personal use of this material is permitted. If interested in reprinting/republishing IEEE copyrighted material for advertising or promotional purposes or for creating new collective works for resale or redistribution, please go to http://www.ieee.org/publications_standards/publications/rights/rights_link.html to learn how to obtain a License from RightsLink.

If applicable, University Microfilms and/or ProQuest Library, or the Archives of Canada may supply single copies of the dissertation.

BACK CLOSE WINDOW

RightsLink

LZ

An Environment-Adaptive Radio Propagation Path Loss Model With Ray-Based Validation

Author: Lingyou Zhou
Publication: IEEE Antennas and Wireless Propagation Letters
Publisher: IEEE
Date: October 2024

Thesis / Dissertation Reuse

The IEEE does not require individuals working on a thesis to obtain a formal reuse license, however, you may print out this statement to be used as a permission grant:

Requirements to be followed when using any portion (e.g., figure, graph, table, or textual material) of an IEEE copyrighted paper in a thesis:

1) In the case of textual material (e.g., using short quotes or referring to the work within these papers) users must give full credit to the original source (author, paper, publication) followed by the IEEE copyright line © 2011 IEEE.
2) In the case of illustrations or tabular material, we require that the copyright line © [Year of original publication] IEEE appear prominently with each reprinted figure and/or table.
3) If a substantial portion of the original paper is to be used, and if you are not the senior author, also obtain the senior author's approval.

Requirements to be followed when using an entire IEEE copyrighted paper in a thesis:

1) The following IEEE copyright/ credit notice should be placed prominently in the references: © [year of original publication] IEEE. Reprinted, with permission, from [author names, paper title, IEEE publication title, and month/year of publication]
2) Only the accepted version of an IEEE copyrighted paper can be used when posting the paper or your thesis on-line.
3) In placing the thesis on the author's university website, please display the following message in a prominent place on the website: In reference to IEEE copyrighted material which is used with permission in this thesis, the IEEE does not endorse any of [university/educational entity's name goes here]'s products or services. Internal or personal use of this material is permitted. If interested in reprinting/republishing IEEE copyrighted material for advertising or promotional purposes or for creating new collective works for resale or redistribution, please go to http://www.ieee.org/publications_standards/publications/rights/rights_link.html to learn how to obtain a License from RightsLink.

If applicable, University Microfilms and/or ProQuest Library, or the Archives of Canada may supply single copies of the dissertation.

BACK CLOSE WINDOW

RightsLink

LZ

Ray-Based Characterization of the AMPLE Model From 0.85 to 5 GHz

Author: Lingyou Zhou
Publication: IEEE Transactions on Antennas and Propagation
Publisher: IEEE
Date: October 2025

Quick Price Estimate

The IEEE does not require individuals working on a thesis to obtain a formal reuse license, however, you may print out this statement to be used as a permission grant:

Requirements to be followed when using any portion (e.g., figure, graph, table, or textual material) of an IEEE copyrighted paper in a thesis:

1) In the case of textual material (e.g., using short quotes or referring to the work within these papers) users must give full credit to the original source (author, paper, publication) followed by the IEEE copyright line © 2011 IEEE.
2) In the case of illustrations or tabular material, we require that the copyright line © [Year of original publication] IEEE appear prominently with each reprinted figure and/or table.
3) If a substantial portion of the original paper is to be used, and if you are not the senior author, also obtain the senior author's approval.

Requirements to be followed when using an entire IEEE copyrighted paper in a thesis:

1) The following IEEE copyright/ credit notice should be placed prominently in the references: © [year of original publication] IEEE. Reprinted, with permission, from [author names, paper title, IEEE publication title, and month/year of publication]
2) Only the accepted version of an IEEE copyrighted paper can be used when posting the paper or your thesis on-line.
3) In placing the thesis on the author's university website, please display the following message in a prominent place on the website: In reference to IEEE copyrighted material which is used with permission in this thesis, the IEEE does not endorse any of [university/educational entity's name goes here]'s products or services. Internal or personal use of this material is permitted. If interested in reprinting/republishing IEEE copyrighted material for advertising or promotional purposes or for creating new collective works for resale or redistribution, please go to http://www.ieee.org/publications_standards/publications/rights/rights_link.html to learn how to obtain a License from RightsLink.

If applicable, University Microfilms and/or ProQuest Library, or the Archives of Canada may supply single copies of the dissertation.

I would like to... reuse in a thesis/dissertation

RightsLink

LZ

A Site-Specific Channel Large-Scale Parameter Model With Ray-Based Validation

Author: Lingyou Zhou
Publication: IEEE Transactions on Vehicular Technology
Publisher: IEEE
Date: 05 December 2025

Quick Price Estimate

The IEEE does not require individuals working on a thesis to obtain a formal reuse license, however, you may print out this statement to be used as a permission grant:

Requirements to be followed when using any portion (e.g., figure, graph, table, or textual material) of an IEEE copyrighted paper in a thesis:

1) In the case of textual material (e.g., using short quotes or referring to the work within these papers) users must give full credit to the original source (author, paper, publication) followed by the IEEE copyright line © 2011 IEEE.
2) In the case of illustrations or tabular material, we require that the copyright line © [Year of original publication] IEEE appear prominently with each reprinted figure and/or table.
3) If a substantial portion of the original paper is to be used, and if you are not the senior author, also obtain the senior author's approval.

Requirements to be followed when using an entire IEEE copyrighted paper in a thesis:

1) The following IEEE copyright/ credit notice should be placed prominently in the references: © [year of original publication] IEEE. Reprinted, with permission, from [author names, paper title, IEEE publication title, and month/year of publication]
2) Only the accepted version of an IEEE copyrighted paper can be used when posting the paper or your thesis on-line.
3) In placing the thesis on the author's university website, please display the following message in a prominent place on the website: In reference to IEEE copyrighted material which is used with permission in this thesis, the IEEE does not endorse any of [university/educational entity's name goes here]'s products or services. Internal or personal use of this material is permitted. If interested in reprinting/republishing IEEE copyrighted material for advertising or promotional purposes or for creating new collective works for resale or redistribution, please go to http://www.ieee.org/publications_standards/publications/rights/rights_link.html to learn how to obtain a License from RightsLink.

If applicable, University Microfilms and/or ProQuest Library, or the Archives of Canada may supply single copies of the dissertation.

I would like to... reuse in a thesis/dissertation